Thesis
UCRL-LR-142199

Microcalorimetry and the Transition-Edge Sensor

Mark Lindeman, Ph.D.

April, 2000

U.S. Department of Energy
Lawrence Livermore National Laboratory

DISCLAIMER

This work was performed under the auspices of the U. S. Department of Energy by the University of California, Lawrence Livermore National Laboratory under Contract No. W-7405-Eng-48.

MICROCALORIMETRY AND THE TRANSITION-EDGE SENSOR

by

Mark Anton Lindeman

A thesis submitted in partial fulfillment
of the requirements for the degree of

Doctor of Philosophy

University of California at Davis

2000

Approved by

Chairperson of Supervisory Committee

Program Authorized
to Offer Degree Department of Applied Science

Date March 23, 2000

University of California at Davis

Abstract

MICROCALORIMETERY AND THE TRANSITION-EDGE SENSOR

by Mark Anton Lindeman

Chairperson of the Supervisory Committee: Professor Stephen Cramer
Department of Applied Science

Many scientific and industrial applications call for quantum-efficient high-energy-resolution microcalorimeters for the measurement of x rays. The applications driving the development of these detectors involve the measurement of faint sources of x rays in which few photons reach the detector. Interesting astrophysical applications for these microcalorimeters include the measurement of composition and temperatures of stellar atmospheres and diffuse interstellar plasmas. Other applications of microcalorimeter technology include x-ray fluorescence (XRF) measurements of industrial or scientific samples. We are attempting to develop microcalorimeters with energy resolutions of several eV because many sources (such as celestial plasmas) contain combinations of elements producing emission lines spaced only a few eV apart. Our microcalorimeters consist of a metal-film absorber (250 μm × 250μm × 3 μm of copper) coupled to a superconducting transition-edge-sensor (TES) thermometer. This microcalorimeter demonstrated an energy resolution of 42 eV (FWHM) at 6 keV, excellent linearity, and showed no evidence of position dependent response. The response of our microcalorimeters depends both on the temperature of the microcalorimeter and on the electrical current conducted through the TES thermometer. We present a microcalorimeter model that extends previous microcalorimeter theory to include additional current dependent effects. The model makes predictions about the effects of various forms of noise. In addition, the model helps us to understand what measurements are useful for characterizing TES microcalorimeters. While the energy resolution we obtained was quite good (twice as good as conventional semiconductor-based x-ray detectors), the obtained resolution was not as good as expected, due to excess noise from fluctuations in the TES thermometer. The energy resolution of future TES microcalorimeters can be improved by redesigning the calorimeters to minimize the noise due to these fluctuations.

TABLE OF CONTENTS

ACKNOWLEDGMENTS

The author wishes to thank all of the members of the cryogenic detector group at Lawrence Livermore National Laboratory. In particular, I would like to thank my research advisor, Simon Labov, for providing a great environment for the development of the graduate students' professional and interpersonal skills. Jan Batteux, the group technician, produced or maintained much of the necessary mechanical equipment. Daniel Chow, Matthias Frank, Larry Hiller, Simon Labov, and Carl Mears participated in many important discussions of the physics in this thesis. Larry also provided computer systems support. I owe thanks to my mother, Grace Lindeman, for providing much encouragement. I would also like to thank Lisa Woods for all the kindness and assistance that she has given in support of me and my goals. Steve Cramer, Simon Labov, and Richard Freeman deserve thanks for reviewing this thesis. This work was performed under the auspices of the U.S. Department of Energy by University of California Lawrence Livermore National Laboratory under contract No. W-7405-Eng-48, with support from the NASA Constellation X-ray Mission Technology Development Program under interagency agreement S-10256-G.

LIST OF SYMBOLS

α'	unitless measure of the variation of a thermometer's resistance with temperature
β	unitless measure of the variation of a thermometer's resistance with electric current
γ	unitless measure of the variation of a microcalorimeters heat capacity with temperature
δI	small perturbation in the electrical current I due to noise or the absorption of a particle by a microcalorimeter
δT	small perturbation in the temperature T of a microcalorimeter due to noise or the absorption of a particle by a microcalorimeter
Δ	energy gap of a superconductor
ΔE_{FWHM}	full-width-half-max energy resolution
ΔT	change in temperature of a microcalorimeter caused by the absorption of an photon
κ	thermal conductivity in the thermometer
Φ_0	the flux quantum
σ	standard deviation or electrical conductivity
ρ	resistivity in the thermometer
τ_{d}	exponential decay time of a pulse
τ_{J}	Joule heating time constant of the microcalorimeter model
τ_{el}	electrical time constant of the microcalorimeter theory (approximately *L/R)*

τ_{eff}	effective thermal time constant of the microcalorimeter model
τ_{etc}^{2}	electrothermal coupling time constant of the microcalorimeter model
τ_{r}	rise time of a pulse
τ_{th}	thermal time of a microcalorimeter (approximately C/G)
τ_{VN}	voltage noise reduction time constant of the microcalorimeter model
φ	phase of the order parameter Ψ from Ginzburg-Landau theory
Ψ	order parameter of Ginzburg-Landau theory
ξ	the Ginzburg-Landau coherence length
A	cross term of the microcalorimeter model relating temperature fluctuations to the rate of change of the current in the thermometer
B	cross term of the microcalorimeter model relating current fluctuations to the rate of change in temperature of the microcalorimeter
c	specific heat of the transition edge sensor
C	heat capacity of the microcalorimeter
C_{o}	heat capacity of the microcalorimeter when the microcalorimeter is in equilibrium
C_{abs}	heat capacity of the
C_{therm}	heat capacity of the thermometer
$D(f)$	normalization factor in the microcalorimeter model
f	frequency
G	thermal conductance between the microcalorimeter and the bath
g	thermal conductance per unit volume in the TES

G_{abs}	thermal conductance between the absorber and the bath
I	electrical current in the thermometer
I_0	electrical current in the thermometer when the microcalorimeter is in equilibrium
I_c	critical current of a superconductor
i	$\sqrt{-1}$
J	electrical current density in the thermometer
k_B	Boltzmann's constant
L	inductance of the electronic bias circuit and amplifier
N	exponent in the power law that describes the cooling power of the thermal coupling between the microcalorimeter and the bath
P_{abs}	power deposited in the absorber by the absorption of x rays or other radiation
P_{cool}	cooling power of the thermal coupling from the microcalorimeter to the bath
P_J	power due to Joule heating in the thermometer
P_{VN}	power fluctuations due to electrical noise in the thermometer
R	electrical resistance of the thermometer
R_0	electrical resistance of the thermometer when the microcalorimeter is in equilibrium
R_s	resistance of the shunt resistor in the electronic bias circuit
R_{th}	Thevenin equivalent resistance of the electronic bias circuit
S	entropy

t	time
T	temperature of the microcalorimeter
T_0	temperature of the microcalorimeter when the microcalorimeter is at equilibrium
T_{bath}	the temperature of the cold bath that is coupled to the microcalorimeter
U	internal energy of the microcalorimeter
V	voltage across the thermometer
V_0	voltage across the thermometer when the calorimeter is at equilibrium
V_{th}	Thevenin equivalent voltage bias of the electronic bias circuit
V_{VN}	voltage fluctuations due to electronic noise in the thermometer
V_{Rth}	voltage fluctuations due to electronic noise in the electronic bias circuit

Chapter 1

INTRODUCTION

1.1 Low temperature energy-dispersive detectors and microcalorimetry

A typical low-temperature energy-dispersive detector absorbs energy from particles that impact it. It converts that energy into excitations that diffuse and thermalize within the detector, as illustrated in Fig. 1.1. The presence of additional excitations causes the electrical resistance or some other measurable property of the detector to change. These changes are measured electronically, providing a measurement of the energy of the absorbed particle. Eventually, the energy of the event diffuses out of the detector to a large cold bath. This process returns the detector to equilibrium so that it is ready to measure another absorption event.

Excitations are disturbances in the material of the detector. More specifically, they are modes of the system that are excited above their ground state energies. Typically, excitations are modeled as particles that travel inside a material. Lattice vibrations, which are modeled as particles called phonons, are an example of one type of excitation. Excitations are created by thermal energy, and the number of excitations in a material at equilibrium increases with temperature. Excitations are also created by athermal events such as the absorption of a particle as shown in Fig. 1.1. The typical energy of athermal excitations can be much larger than that of thermal excitations.

In any detector, some of the excitations are phonons. What other kinds of excitations exist depends upon the material composition of the detector. In superconductors, part of the athermal excitations created by the absorption of an energetic particle are quasiparticles. In semiconductors, electron-hole pairs are created. Regardless of the material, these excitations carry energy and travel through the detector and scatter both elastically and inelastically. This process causes a few initial energetic excitations to be converted to many excitations of lesser energy as time progresses. Ultimately, the athermal distribution of excitations is converted to a thermal distribution of excitations through this process. Thus, the thermalization process converts the energy collected from a particle into heat. Heat from the event eventually leaks out of the detector to a cold bath to which the detector is thermally coupled, thereby returning the detector to equilibrium.

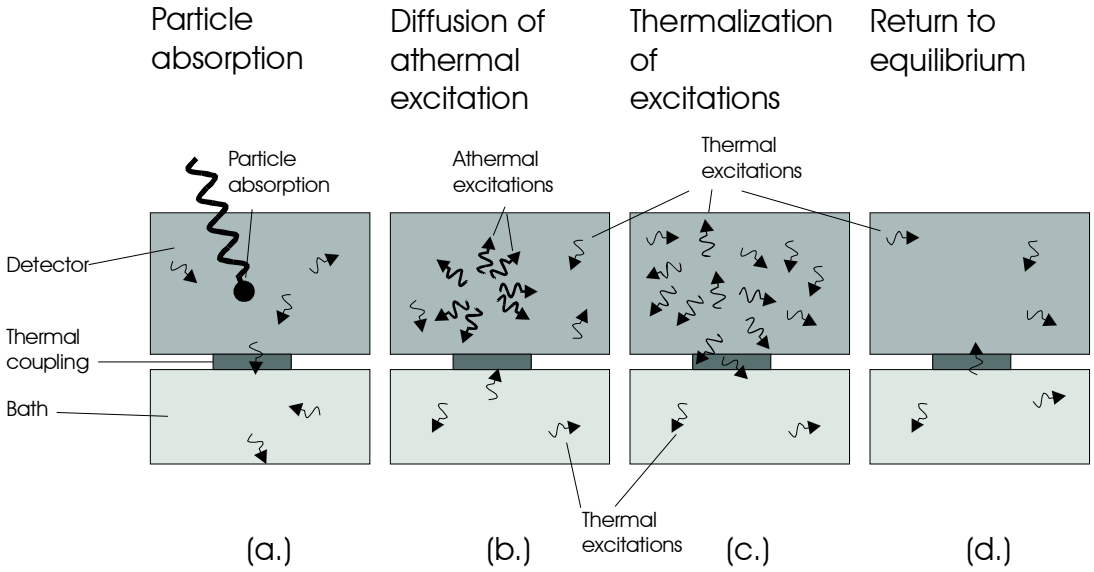

Figure 1.1 The absorption of a particle in a low-temperature energy-dispersive detector. The internal components of the detector, such as absorbers and sensors, are not illustrated in this general picture because they are specific to particular types of detectors. a.) The detector is at equilibrium until it absorbs particle. b.) The absorption event creates a number of excitations in the detector. c.) Inelastic scattering produces many more thermal excitations. d.) The detector eventually cools back to equilibrium, ready to measure another particle.

Energy-dispersive detectors measure the amount of energy that is collected from particles and converted to excitations. If the average energy of a typical excitation is known, a measurement of the energy of a particle can be obtained by counting the number of athermal excitations created (before they are converted to phonons). Detectors that measure the athermal excitations are called athermal detectors. Another way to perform the energy measurement is to let all the excitations be thermalized then measure the heat from thermalization. Detectors that function in this way are called thermal detectors.

Microcalorimeters are a type of thermal energy-dispersive detector. Figure 1.2 illustrates the thermal couplings between the absorber thermometer and cold bath of a simple microcalorimeter. The resistive thermometer is strongly coupled to the absorber and weakly coupled to the cold bath, which is held at a constant temperature. The cold bath serves to keep the temperature of the microcalorimeter near a fixed equilibrium in the absence of large absorption events. The electrical resistance of the thermometer, which is a function of

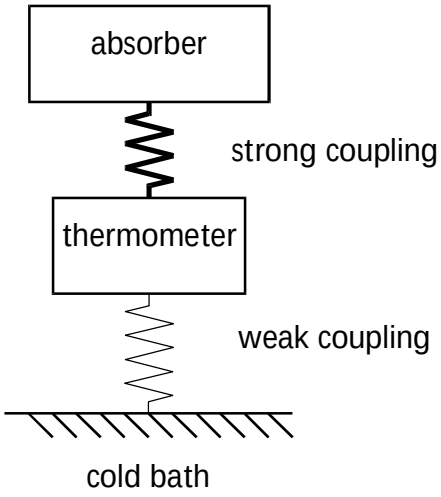

Figure 1.2. A simple microcalorimeter. The absorber is strongly coupled to the thermometer. The microcalorimeter is weakly coupled to the cold bath. Ideally, the thermometer and absorber are so well coupled that they act like one thermal element. Absorption events in the absorber cause the temperature to increase in the microcalorimeter. The temperature increase is measured by the thermometer.

the temperature, is measured electronically. The electronic bias circuit, which is used to measure the resistance, drives a current through the thermometer. Joule heating from this current usually causes the equilibrium temperature of the thermometer and absorber to be somewhat higher than the bath temperature.

When a particle is absorbed in a microcalorimeter, its energy is thermalized, which results in an increase in temperature of the microcalorimeter. The heat from the event eventually leaks out of the microcalorimeter to the cold bath, which returns it to equilibrium. Thus, the usual response of a microcalorimeter to an absorption event is a pulse, as shown in Fig. 1.3. The amplitude of the pulse is proportional the energy of the event that is measured. The rise time of the thermal pulse is determined by the time it takes energy from the absorption event to be thermalized in the thermometer. In the simplest microcalorimeters, the decay time is given by the time it takes for the thermal energy to leak out of the microcalorimeter into the cold bath. However, the Joule heating from the electrical bias on the thermometer can lengthen or shorten the decay time, as will be described in Chapter 4.

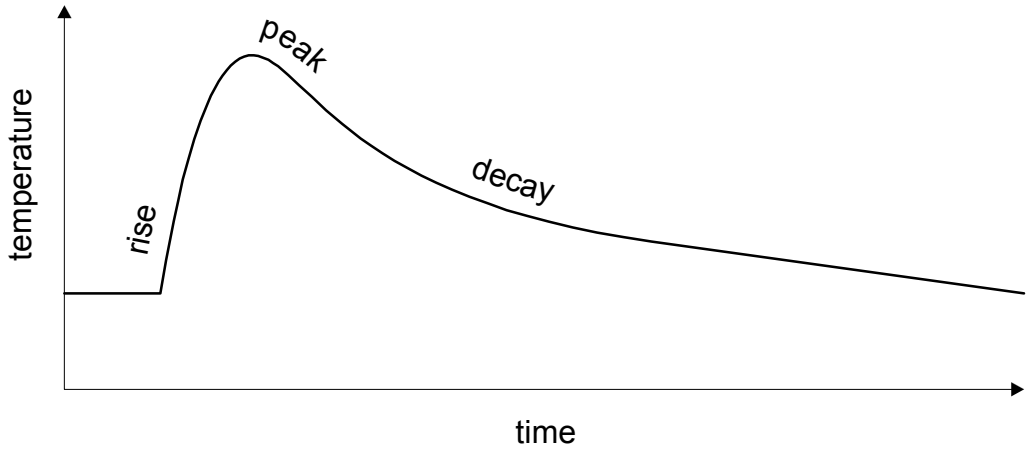

Figure 1.3. The thermal response of a microcalorimeter to the absorption of a particle. Initially, the microcalorimeter is at thermal equilibrium. When a particle is absorbed, its energy is thermalized. The increasing thermal energy causes a quick rise in temperature. The heat flow out of the microcalorimeter into the bath through the weak thermal coupling increases as the temperature of the microcalorimeter increases. This causes the temperature to decay back to equilibrium after the energy of the particle is thermalized.

1.2 Noise and energy resolution

Typically, the energies of thousands of absorption events are measured during an experiment. The amplitudes of the measured pulses are then plotted in a histogram. An illustration of such a histogram is shown in Fig. 1.4. The various peaks in the histogram correspond to the various energies of the particles being measured. The detector is calibrated so that the histogram can be plotted as a function of energy of the particles. The widths of the peaks are determined by noise and other non-ideal effects. Ultimately, the best obtainable resolution is limited by noise caused by intrinsic fluctuations in these devices. The energy resolution is usually reported in terms of the full-width-half-maximum (FWHM) of the peaks, ΔE. In calorimeters, the noise causes a Gaussian distribution of energy measurements. For Gaussian noise, the full-width-half-maximum value is approximately 2.35 times the standard deviation σ. Various sources of noise will be discussed throughout this thesis.

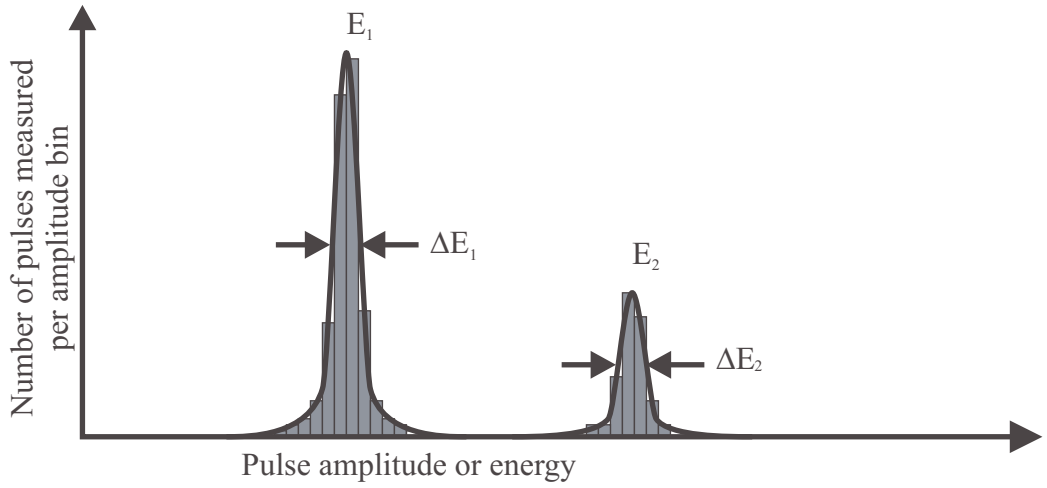

Figure 1.4. An ideal histogram of pulse amplitudes. The two peaks correspond to particles of two energies, E_1 and E_2. The area of the peaks is proportional to the number of counts detected, which depends on the intensity of the source of the particles and the collection efficiency of the detector at the peak energies. The grey rectangles represent the number of counts distributed into each of the amplitude bins. The noise causes the peaks to be Gaussian curves.

A reasonable estimate of the energy resolution of a microcalorimeter is obtained by calculating the magnitude of the fluctuations of the thermal energy in the detector. Thermodynamic fluctuations result from the random transfer of thermal energy between the various modes of a system. These fluctuations (called phonon noise) cause heat to move back and forth between the detector and the cold bath in a random way. This causes the internal energy of the device to fluctuate by an amount,

$$\Delta E_{\text{therm}} = 2.35\sqrt{k_{\text{B}} T^2 C} \qquad (1.1)$$

(FWHM), where k_{B} is Boltzman's constant, T is the temperature of the device, and C is the heat capacity of the device. The magnitude of the internal energy fluctuations in a device is a good first estimate of the energy resolution of an energy-dispersive detector. Equation (1.1) shows that the energy resolution is smaller (and therefore better) for low temperature devices with small heat capacities. For this reason, our devices are designed with small heat capacities and operated at low temperatures (~0.1 K). It is important to note that equation (1.2), which is derived in Chapter 3, gives the magnitude of the energy fluctuations from equilibrium over long time scales. Over shorter time scales, the internal energy actually fluctuates less. Microcalorimeters can take advantage of this fact and obtain energy resolutions much better than the resolution ΔE_{therm}. The optimal resolution of a microcalorimeter will be derived in Chapter 4. Athermal detectors often suffer from other sources of noise associated with the counting of athermal excitations, such as shot noise. This statistical noise limits the energy resolution of athermal detectors.

1.3 The transition-edge-sensor microcalorimeter

Transition-edge-sensor (TES) microcalorimeters are the main subject of this thesis. Like all microcalorimeters, these devices consist of an absorber and a thermometer (the transition-edge sensor). The type of absorber used depends on what type of particle the device is

designed to measure. My work at Lawrence Livermore National Laboratory has mainly involved the development of x-ray detectors and gamma-ray detectors. In our x-ray detectors, the absorbers are thin films of normal metal, such as copper, which efficiently absorb soft x rays. Our gamma ray detectors have absorbers consisting of bulk crystals of superconductor or dielectric material that are designed to absorb gamma rays, yet have heat capacities that are not too large. In both cases, the absorber dominates the heat capacity of the device, and the absorber is well coupled to the transition-edge-sensor thermometer, while the entire microcalorimeter is weakly coupled to the cold bath.

Transition-edge sensors (TES) are very sensitive resistive thermometers made of thin films of superconductor. An illustration of resistance versus temperature of a superconductor is shown in Fig. 1.5. At temperatures sufficiently below the critical temperature, T_c, the electrical resistance of a superconductor is zero. At temperatures sufficiently above T_c, the

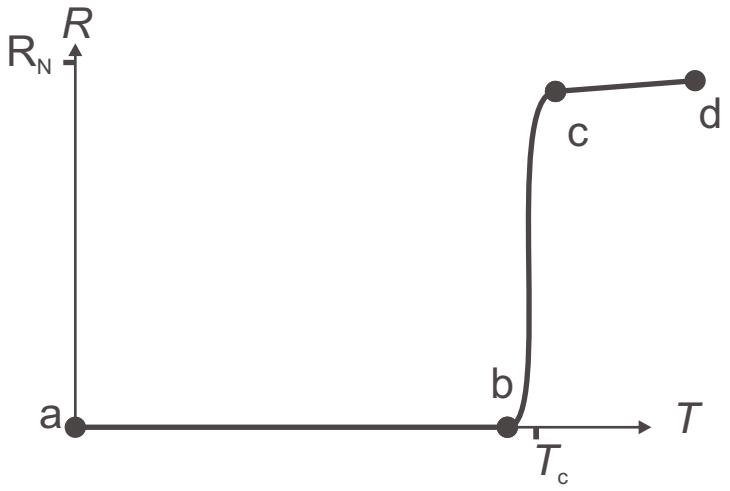

Figure 1.5. Resistance versus temperature of a superconducting transition-edge-sensor (TES) thermometer. At low temperatures, the TES superconducts, and its electrical resistance is zero (segment ab). Near the critical temperature T_c, the device is in the phase transition and the resistance increases sharply with increasing temperature (segment bc). At higher temperatures, the thermometer is in the normal metal state, and its resistance is the normal resistance R_N (segment cd). In our devices, the phase transition is typically several mK wide, and the normal resistance R_N is roughly 1 Ω.

superconductor is in the normal metal state. In our devices, T_c is typically 100 to 200 mK. At low temperatures (less than a few Kelvin), the normal resistance of our metal films is dominated by impurity scattering of electrons. Impurity scattering is independent of temperature. Therefore, the normal resistance is nearly constant just above T_c. Close to T_c, the resistance of a superconductor increases rapidly with temperature. This is the phase transition between the superconducting and normal metal states. The TES operated in the phase transition. Because the resistance increases rapidly in the transition, the TES is a very sensitive thermometer.

An example of a transition-edge sensor microcalorimeter is shown in Fig. 1.6. The figure shows the layout of a microcalorimeter designed to measure soft x rays with an energy resolution of a few eV. In order to obtain such high energy resolution, the heat capacity is kept small. Our soft x-ray microcalorimeters have a volume of about 10^{-14} m^3. These devices are made of thin metal films that are deposited on a thin membrane. The membranes are supported by a silicon substrate. Depositing the devices on the membranes keeps them relatively decoupled from the silicon substrate, which functions as the cold bath of the microcalorimeter. Both ends of the TES are connected to an electronic circuit that reads the electrical resistance across the length of the device. When an x ray is absorbed in the microcalorimeter, a pulse is measured by the electronic circuit. The amplitude of the pulse is proportion al to x-ray energy.

In operation, a bias voltage is applied to the TES thermometer, and the current flowing through it is measured. However, the resistance of a TES depends not only on temperature, but also on the magnitude of the electrical current conducted through the TES. In Chapter 4, I present a model that includes such current dependent effects. In Chapter 7 and Appendix A, I present experimental methods, based on that model, that can be used to thoroughly characterize TES microcalorimeters.

1.4 Absorption of radiation

The particle collection efficiency of an energy-dispersive detector is determined by the volume and the material composition of the absorber. Thick absorbers have higher absorption efficiency, and absorbers with larger collection area can measure more particles from faint sources. However, the volume of the absorber must be kept small to obtain good energy resolution. Large absorbers can limit the energy resolution of a detector by increasing its heat capacity. Also, large absorbers can limit the energy resolution by increasing the diffusion time of the excitations in the absorber. In athermal detectors, the athermal excitations are typically converted to thermal excitations through inelastic scattering. These losses increase with the size of the absorber. In thermal detectors, long diffusion times lengthen the measured pulses (by increasing the rise time of the pulses) and decrease the pulses' amplitude. This results in lower signal-to-noise ratio in the pulses. Because of these effects, the size of the absorber in energy-dispersive detectors is often

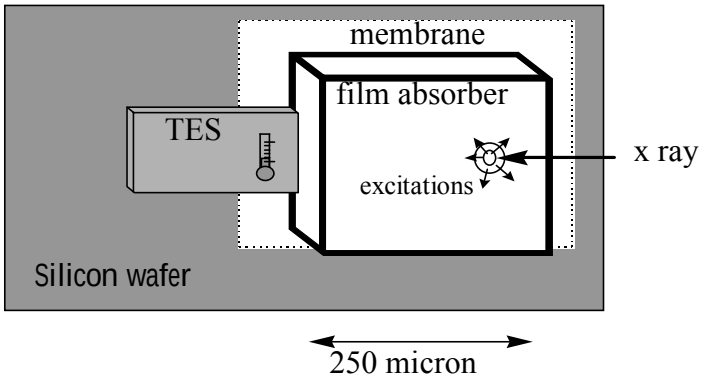

Figure 1.6. An illustration of the layout of a TES based microcalorimeter for the measurement of x rays. In this device, a thin-film absorber is connected to a TES thermometer. In our devices, the absorber is typically 250 microns by 250 microns in area. It is typically 0.5 to 3 microns thick, and made of a metal film that does not superconduct at the operating temperature of the device. The TES thermometer is much smaller in volume and heat capacity than the absorber.

determined by a compromise between collection efficiency and energy resolution.

Collection efficiency is affected by a number of other considerations. Energetic x rays can pass though thin films unabsorbed. For x rays with energies greater than 1 keV, elements with large atomic numbers are often used as absorbers because they are more efficient absorbers of x rays[1]. Soft x rays (less than 1 keV) can be easily absorbed by thin films. However, if air or moisture freezes on to the surface of a detector, it will absorb some of the soft x rays. Therefore, the detectors must be operated in a high quality vacuum space. In the optical band, it is important that the surface of the absorber be non-reflective, so that the absorber absorbs rather than reflects radiation.

1.5 Applications of low-temperature energy-dispersive detectors

Low temperature energy-dispersive detectors can be used to measure the energies of a variety of particles. These detectors have been used to measure electromagnetic radiation such as optical light, x rays or gamma rays [2-7]. In such detectors, the energy of individual photons, $E = h\nu$, is measured. Alternatively, the kinetic energies, $E = mv^2/2$, of massive particles that impact such a detector can also be measured [8].

Low-temperature energy-dispersive detectors based on transition-edge sensor technology are being developed for a number of applications. They are being developed as broadband x-ray detectors by our group [9] (the Labov cryodetector group at Lawrence Livermore National Laboratory) and others [3,10,11]. Applications of these x ray detectors include imaging arrays for x-ray astronomy, such as the NASA Constellation-X project (see web page at http://constellation.gsfc.nasa.gov/). These detectors also have applications for x-ray fluorescence (XRF) measurements of biological or industrial samples at a synchrotron radiation laboratory, similar to what our group has demonstrated using our athermal detectors [12]. Our group is also developing TES microcalorimeters for gamma-ray

detection [7]; these sensitive gamma ray detectors can be used to detect and analyze the composition of nuclear materials [13]. The LLNL and NIST groups have incorporated energy-dispersive detectors into matrix-assisted-laser-desorption-ionization time-of-flight (MALDI-TOF) mass spectrometers [8,14,15]. This technology can accurately measure the masses of large biomolecures, such as proteins or snippets of DNA.

Others have been developing calorimeters using transition-edge sensors with large absorbers for the detection of weakly interacting massive particles (WIMPs) a hypothetical form of dark matter that may comprise the vast majority of the mass of the universe [16,17].

1.6 Current state of research

Excellent progress is being made toward the development of cryogenic energy-dispersive detectors with high energy resolution. In 1991, the collaboration between NASA Goddard Space Flight Center and Wisconsin University, demonstrated a resolution of 7.3 eV 6 keV, using microcalorimeters composed of HgTe absorbers and doped silicon thermisters [18]. In 1996, our group demonstrated 29 eV FWHM resolution at 6 keV using SIS tunnel junctions, a type of athermal detector [19]. These SIS detectors were shown to be able to measure at very high count rates. A resolution of 13 eV at 284eV was measured at 20,000 counts per second [20]. In 1997, the NIST Boulder group demonstrated a resolution of 7.2 eV at 6 keV using TES based microcalorimeters [3]. In 1999, the Milano group demonstrated 5 eV resolution using neutron transmutation doped (NTD) Ge thermistors [6].

Energy-dispersive, imaging detectors are being developed as well. One scheme for doing this involves arraying large numbers of energy dispersive detectors, where each detector functions as an image pixel [21-23]. Researchers at NIST have been developing multiplexing technology for arrays of TES based calorimeters [24]. Another scheme involves coupling one absorber to several detectors (thermal or athermal). In this scheme,

the location of an absorption event can be found by comparing the measurements of the several detectors to each other [25,26].

[1] David T. Attwood, *Soft x-rays and extreme ultraviolet radiation : principles and applications* (Cambridge University Press, New York, 1999).

[2] D. McCammon, W. Cui, M. Juda *et al*., "Thermal calorimeters for high resolution X-ray spectroscopy," Nuclear Instruments & Methods in Physics Research, Section A Spectrometers, Detectors and Associated Equipment) **A326** (1-2), 157-65 (1993).

[3] D. A. Wollman, K. D. Irwin, G. C. Hilton *et al*., "High-resolution, energy-dispersive microcalorimeter spectrometer for microanalysis," Journal of Microscopy **188 pt.3**, 196-223 (1997).

[4] S. E. Labov, M. Frank, J. B. leGrand *et al*., "Cryogenic Detector Development at LLNL: Ultraviolet, X-Ray, Gamma-Ray and Biomolecular Spectroscopy," Proc. 7th Int. Workshop on Low Temperature Detectors LTD-7, 27 July - 2 August 1997, Munich, Germany, pub. by MPI Physik, ISBN 3-00-002266-X, avail. from urg@mppmu.mpg.de.

[5] M. Frank, L. J. Hiller, J. B. le Grand *et al*., "Energy resolution and high count rate performance of superconducting junction X-ray spectrometers," Review of Scientific Instruments **69** (1), 25-31 (1998).

[6] A. Alessandrello, J. W. Beeman, C. Brofferio *et al*., "High energy resolution bolometers for nuclear physics and X-ray spectroscopy," Physical Review Letters **82** (3), 513-15 (1999).

[7] D. Chow, M. A. Lindeman, M. F. Cunningham *et al*., "X-Ray and Gamma-Ray Spectrometers using Bulk Absorbers coupled to Mo/Cu Multilayer Superconducting

Transition Edge Sensors," The 8th Int. Workshop on Low Temperature Detectors (LTD-8), 1999 to be published in Nuclear Instruments & Methods in Physics Research

[8] M. Frank, S. E. Labov, G. Westmacott *et al*., "Energy-sensitive cryogenic detectors for high-mass biomolecule mass spectrometry," Mass Spectrometry Reviews **18** (3-4), 155-186 (1999).

[9] M. F. Cunningham, M. A. Lindeman, D. Chow *et al*., "Mo/Cu Superlattice Transition Edge Sensor with Thin-Film Absorbers," The 8th Int. Workshop on Low Temperature Detectors (LTD-8), 1999 to be published in Nuclear Instruments & Methods in Physics Research.

[10] A. Peacock, P. Verhoeve, N. Rando *et al*., "On the detection of single optical photons with superconducting tunnel junction," Journal of Applied Physics **81** (11), 7641-6 (1997).

[11] M. P. Bruijn, F. B. Kiewiet, M. L. van den Berg *et al*., "High quality superconducting tunnel junctions on Nb and Ta single for radiation detection," Applied Physics Letters **71** (9), 1252-4 (1997).

[12] M. Frank, C. A. Mears, S. E. Labov *et al*., "Cryogenic high-resolution X-ray spectrometers for SR-XRF and microanalysis," Journal of Synchrotron Radiation **5** (PT3), 515-517 (1998).

[13] H. Netel, M. Frank, S. E. Labov *et al*., "Initial Development of a Superconducting Crystal X-Ray and Gamma-Ray Spectrometer," SPIE Proceedings **2518**, 244 (1995).

[14] M. Frank, C. A. Mears, S. E. Labov *et al*., "High-efficiency detection of 66000 Da protein molecules using a detector in a matrix-assisted laser desorption/ionization time-of-

flight mass spectrometer," Rapid Communications in Mass Spectrometry **10** (15), 1946-1950 (1996).

[15] G. C. Hilton, J. M. Martinis, D. A. Wollman *et al*., "Impact energy measurement in time-of-flight mass spectrometry with cryogenic microcalorimeters," Nature **391** (6668), 672-5 (1998).

[16] D. S. Akerib, P. D. Barnes, Jr., D. A. Bauer *et al*., "Preliminary limits on the WIMP-nucleon cross section from the cryogenic dark matter search (CDMS)," Nuclear Physics B, Proceedings Supplements **70**, 64-8 (1999).

[17] F. Probst, M. Frank, S. Cooper *et al*., "Model for cryogenic particle detectors with superconducting phase transition thermometers," Journal of Low Temperature Physics **100** (1-2), 69-104 (1995).

[18] D. McCammon, W. Cui, M. Juda *et al*., "Cryogenic microcalorimeters for high resolution spectroscopy: current status and future prospects," Nuclear Physics A **A527**, 821-4 (1991).

[19] M. Frank, C. A. Mears, S. E. Labov *et al*., "High-Resolution X-Ray Detectors With High-Speed Squid Readout of Superconducting Tunnel Junctions," Nuclear Instruments & Methods in Physics Research Section a-Accelerators Spectrometers Detectors and Associated Equipment **370** (1), 41-43 (1996).

[20] M. Frank, L. J. Hiller, J. B. le Grand *et al*., "Energy resolution and high count rate performance of superconducting tunnel junction X-ray spectrometers," Review of Scientific Instruments **69** (1), 25-31 (1998).

[21] R. L. Kelley, S. H. Moseley, C. K. Stahle *et al*., "Development of microcalorimeters for high resolution X-ray spectroscopy," Journal of Low Temperature Physics **93** (3-4), 225-30 (1993).

[22] C. K. Stahle, R. L. Kelley, D. McCammon *et al*., "Microcalorimeter arrays for high resolution soft X-ray spectroscopy," Nuclear Instruments & Methods in Physics Research, Section A Spectrometers, Detectors and Associated Equipment) **370** (1), 173-6 (1996).

[23] D. McCammon, R. Almy, S. Deiker *et al*., "A sounding rocket payload for X-ray astronomy employing high-resolution microcalorimeters," Nuclear Instruments & Methods in Physics Research, Section A Spectrometers, Detectors and Associated Equipment) **370** (1), 266-8 (1996).

[24] J. A. Chervanek, K. D. Irwin, E. N. Grossman *et al*., "Superconducting multiplexer for arrays of transition edge sensors," Applied Physics Letters **74** (26), 4043-5 (1999).

[25] H. Kraus, F. von Feilitzsch, J. Jochum *et al*., "Quasiparticle trapping in a superconductive detector system exhibiting energy and position resolution," Physics Letters B **231** (1-2), 195-202 (1989).

[26] S. Friedrich, K. Segall, M. C. Gaidis *et al*., "Experimental quasiparticle dynamics in a superconducting, imaging X-ray spectrometer," Applied Physics Letters **71** (26), 3901-3 (1997).

Chapter 2

THE SUPERCONDUCTOR TO NORMAL METAL PHASE TRANSITION

2.1 Introduction to the phase transition

Our transition-edge sensors (TES) are thin metal films that are held in the phase transition between the superconducting and normal-metal states. To understand how microcalorimeters based on TES technology function, it is necessary to understand some of the physics of the normal metal state, the superconducting state, and the phase transition. In this chapter, we review several models from solid state physics that we use to explain the dynamics and noise of TES microcalorimeters.

2.2 The normal-metal state: resistance, noise, and heat capacity

2.2.1 Electrical resistance in normal metal films

In normal metals, conduction electrons move freely throughout the metal. When a voltage bias V is applied across a normal metal wire, a gradient in the Coulomb potential forms within the wire. The potential gradient accelerates conduction electrons, causing the electrons to flow to positive Coulomb potential. Individual electrons typically travel many atomic distances until they are inelasticly scattered by imperfections in the metal's crystalline lattice, by impurities in the metal, or by lattice vibrations (phonons). All these scattering processes involve an exchange of energy between the electric current and thermal modes of the metal. Energy is transferred back and forth in a random fashion between the

kinetic energies of the individual electrons and thermal phonons in the metal. If there is a net flow of current in any direction, then on average more energy will be transferred from the motion of the electrons to the thermal vibrations of the crystal than visa versa. Thus, energy from the current flow is irreversibly converted to heat.

Power is required to sustain electrical current flow through normal metal conductors. When a current of magnitude I flows through a normal metal wire, there is a finite voltage drop V in the direction of current flow. The electrical resistance is $R = V / I$. Energy is dissipated with a power $P = I^2 R$. In normal metals, resistance does not vary with the applied voltage or current. The resistance depends on the material composition of the conductor, on its shape, and on its temperature.

At room temperature, the dominant effect causing resistance of our metal films is inelastic scattering of electrons with thermal phonons. The number and energy of phonons in a metal are a temperature dependent quantities. At lower temperatures, fewer thermal phonons are present in the metal. As the temperature of a metal is decreased, the electronic resistance due to thermal electron-phonon scattering decreases. In our low-temperature experiments (which are conducted at temperatures ranging from 50 mK to 2 K), the electrical resistance of our metal films is primarily caused by impurity scattering. Impurity scattering of electrons is a temperature independent process. Consequently, the resistance of our metal films is temperature independent in our low temperature experiments.

2.2.2 Fluctuation, dissipation, and Johnson noise in normal metals

The electrical resistance of a normal metal is caused by the coupling of the electron's motion to the energy of thermal modes of the resistor. When an electron scatters inelastically, energy is transferred from the electron to thermal modes of the system or visa versa. The collective effect of many such interactions within the metal is the random exchange of energy between the motion of the electrons (the electric current) and the

thermal modes (the thermal reservoir). A schematic of this process is shown in Fig 2.1. If there is no net electric current flow in the metal and the electrons are at the same temperature as the thermal modes then energy is exchanged back and forth equally between the motions of electrons and the thermal modes. Consequently, the energy exchanged between the current and the thermal reservoir averages to zero. The effect of the coupling between the electrons and the thermal reservoir is to cause fluctuation in the motions of the electrons. These fluctuations are a form of electronic noise in the electric current or the voltage in the metal.

If a metal is biased so that an electric current is conducted through it, then the metal's electrons have a net nonzero average momentum. In this case, random inelastic scattering events in the metal will on average transfer more energy from the motion of the electrons to the thermal modes than visa versa. This occurs because entropy is increased by this process: it is more probable for the directed motion of the electric current to be scattered into random thermal motions than it is for the random thermal motions to be scattered into

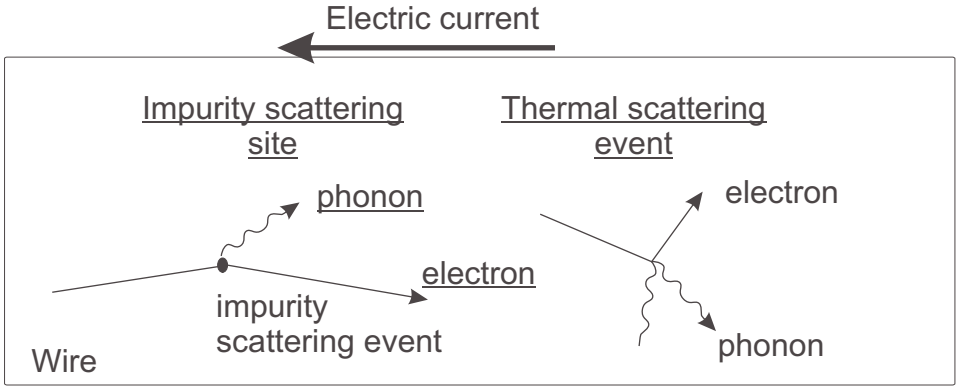

Figure 2.1 Electron scattering in a wire. Electrons are accelerated by a voltage V applied across the wire. Electrons are scattered by impurities or thermal phonons in the metal. The scattering exchanges energy between the kinetic energies of the electrons to thermal vibrations (phonons) in the metal. These scattering events cause fluctuations in the electric current that are responsible for the electrical resistance. The net effect of the scattering is to convert the directed motion of the electric current into random thermal motion.

the directed motion of the electric current. In this case, the fluctuations in the electric current due to inelastic scattering of the electrons have two effects: they are a source of electronic noise and they result in a dissipation of energy from the electric current. Because the same processes cause both fluctuations (noise) and dissipation (electrical resistance), there is fundamental relationship between the electronic noise and the electrical resistance:

$$\left\langle |V(f)|^2 \right\rangle = 4k_B TR\,. \tag{2.1}$$

where k_B is Boltzmann's constant, T is the temperature of the resistor, and R is the resistance. The brackets on the left of equation (2.1) indicate that the equation gives the expectation value of the absolute value of the noise squared. The expectation value of the noise $\langle V(f) \rangle$ is zero. This noise is called Johnson noise after the researcher who first characterized it [1]. A derivation based on simple thermodynamic arguments was presented by Nyquist [2]. A more general treatment of such noise is described by the fluctuation-dissipation theorem [3]. A review of this subject is presented by Reif [4]. In computing the effects of Johnson noise in an electrical circuit, the $V(f)$ noise source is placed in series with the associated resistor.

The scattering events that cause electrical resistance occur at random times. To a very good approximation, the time of any scattering event can be regarded as being uncorrelated to the times of other scattering events. Consequently, Johnson noise, which results from these fluctuations, is frequency independent. (In other words, it is white noise.) The temperature of the thermal reservoir affects the likelihood of energy being scattered from the reservoir to electric current energy. Hence, Johnson noise is temperature dependent.

Johnson noise is the *least* noise that a resistance R due to uncorrelated fluctuations at temperature T can have. It occurs in the limit that a large number of uncorrelated

fluctuations (such as inelastic scattering events) are responsible for dissipation. If electrical resistance R is caused by few uncorrelated fluctuations (such as tunneling of electrons across a tunnel barrier or the motion of magnet flux in a superconductor), then the noise will be larger than the Johnson noise limit. Note that the Johnson noise limit depends on the resistance R, not on the dynamic resistance, dV / dI.

We use TES thermometers, which are electrically resistive, to measure temperature changes in our microcalorimeters. Equation (2.1) is used to calculate a lower limit of the electronic noise of due to TES thermometer with resistance R at temperature T.

2.2.3 Electronic excitations, heat capacity, and thermal conductivity of normal metals

The absorbers of our x-ray microcalorimeters consist of thin metal films. The heat capacity and thermal conductivity of the absorbers significantly affect the performance of our microcalorimeters. Hence, we briefly describe thermal properties of metals.

The electrons in a metal form a Fermi gas. An illustration of the occupation of energy levels of a Fermi gas is illustrated in Fig. 2.2. If the metal is at low temperature, then the electronic states with energies less than the Fermi energy are nearly completely occupied by electrons. The energy levels above the Fermi energy are mostly unoccupied. Only the energy levels whose occupation changes significantly with temperature contribute to the heat capacity.

Most of the electrons that are excited at temperature T by thermal energy in the metal lie within $k_{\mathrm{B}}T$ of the Fermi energy, ε_f. These are the electrons that contribute significantly to the heat capacity. The fraction of electrons in the metal that are excited is approximately $k_{\mathrm{B}}T / \varepsilon_F$. These electrons are typically excited from their ground states with an energy of approximately $k_{\mathrm{B}}T$. If we multiply the number of electrons in the metal N by the fraction

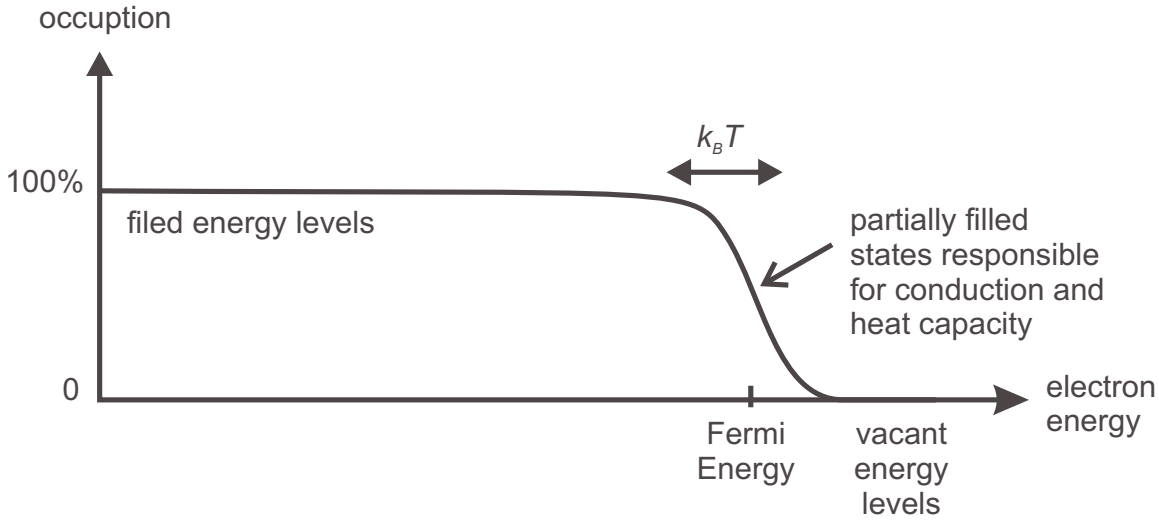

Figure 2.2 Distribution of electrons in a Fermi gas of electrons. The energy states near the Fermi are partially occupied by electrons. These energy states are responsible for the conduction and heat capacity of metals at low temperature.

of electrons that are excited and by the energy of a typical thermal excitation, we find the thermal energy of the electrons is:

$$U_{\mathrm{el}} \approx N \frac{k_{\mathrm{B}} T}{\varepsilon_F} k_{\mathrm{B}} T \,. \tag{2.2}$$

The heat capacity of the electrons is $C_{\mathrm{el}} = dU_{\mathrm{el}} / dT$. From equation (2.2), we find that

$$C_{\mathrm{el}} \approx \frac{2 N k_{\mathrm{B}}{}^2 T}{\varepsilon_F} \,. \tag{2.3}$$

Thus, we find that the electronic heat capacity of a metal is proportional to temperature [5]. The fact that the heat capacity is proportional to temperature will be used later in calculating the effects of the heat capacity on microcalorimeter performance.

Pure metals are good electrical conductors compared to non-metals because the conduction electrons in metals are free to travel throughout the metal. Because the conduction electrons carry heat as well as electric charge, metals are also good thermal conductors. At temperature T, the thermal conductivity κ is proportional to electrical conductivity σ as described by the Wiedemann-Franz Law:

$$\kappa = LT\sigma, \tag{2.4}$$

where L is the Lorenz number. The theoretical value of the Lorenz number is $L = 2.4 \times 10^{-8}\ W\Omega / K^2$. The theoretical value of the Lorenz number is in good agreement with measurements of the Lorentz number of elemental metals at room temperature. However, the real value of the Lorenz number can be as much as an order of magnitude smaller for some metals at low temperatures[5]. In the next chapter, we shall use equation (2.4) to calculate the thermal stability of our TES thermometers.

Thermal vibrations of the metal atoms (phonons) also contribute to the heat capacity and thermal conductivity of a metal. However, the phonon contribution is small compared to the electronic contribution at low temperatures. Therefore, the heat capacity and thermal conductivity of our metal films are approximated by equation (2.3) and equation (2.4).

2.3 The superconducting state

2.3.1 Introduction to superconductivity

As the temperature is decreased from room temperature to temperatures near absolute zero, most elemental metals, many metal alloys, and some other materials undergo a phase transition from the normal state to the superconducting state. The phase transition occurs at the critical temperature T_c. The material superconducts at temperatures less than T_c. The critical temperature depends on the composition of the material.

When a metal is cooled through the critical temperature, a number of the metal's properties change as the metal undergoes the phase transition from the normal metal state to the superconducting state. In the superconducting state, materials have no (direct current) electrical resistance. Bulk superconductors expel magnetic fields. At temperatures far below the critical temperature T_c, the electrons in a superconductor contribute very little to the heat capacity and thermal conductivity of the material.

Kamerlingh Onnes observed zero electrical resistance (to direct current) in several elemental metals at low temperatures, leading to the discovery of the superconducting state [6]. Zero electrical resistance is surprising in the context of the previous discussion of dissipation and noise in normal metals. In light of the previous discussion, it is quite remarkable that inelastic scattering of electrons does not cause dissipation in superconducting metals as it does in the normal state. Lack of electrical resistance in the superconducting state will be described in more detail below.

2.3.2 The Meissner effect

Meissner and Ochfield found that magnetic fields are excluded from superconductors. They found that if magnetic field is applied to bulk normal state material and the material is then cooled into the superconducting state, magnetic fields are expelled as the material goes into the superconducting state. This is process, called the Meissner effect, is illustrated in Fig 2.3. In actuality, magnetic field is not completely expelled from superconductors. Generally, magnetic fields are exponentially screened with depth into a superconductor, but some superconductors (Type II) allow lines of magnetic flux to penetrate through their bulk. This case will be discussed in Section 2.4.3.

A material superconducts at temperatures less than the critical temperature because the free energy of the superconducting state is lower than the free energy of the normal state. (Materials occupy the phase that minimizes their free energy because it is

thermodynamically favorable to do so.) However, additional energy is required to occupy the superconducting phase when a magnetic field is applied. The additional energy is required to expel the magnetic field from the superconductor. For example, the energy of the magnetic field in Fig. 2.3b is higher than the energy of the magnetic field in Fig. 2.3a. If a large enough magnetic field is applied to a superconductor, then the total free energy associated with a material occupying the superconducting state may be larger than the free energy of the normal state. Therefore, a material will not superconduct if such a large magnetic field is applied.

Generally, the free energy of the superconducting state decreases relative to the free energy of the normal state as temperature decreases. When a magnetic field is applied, the free

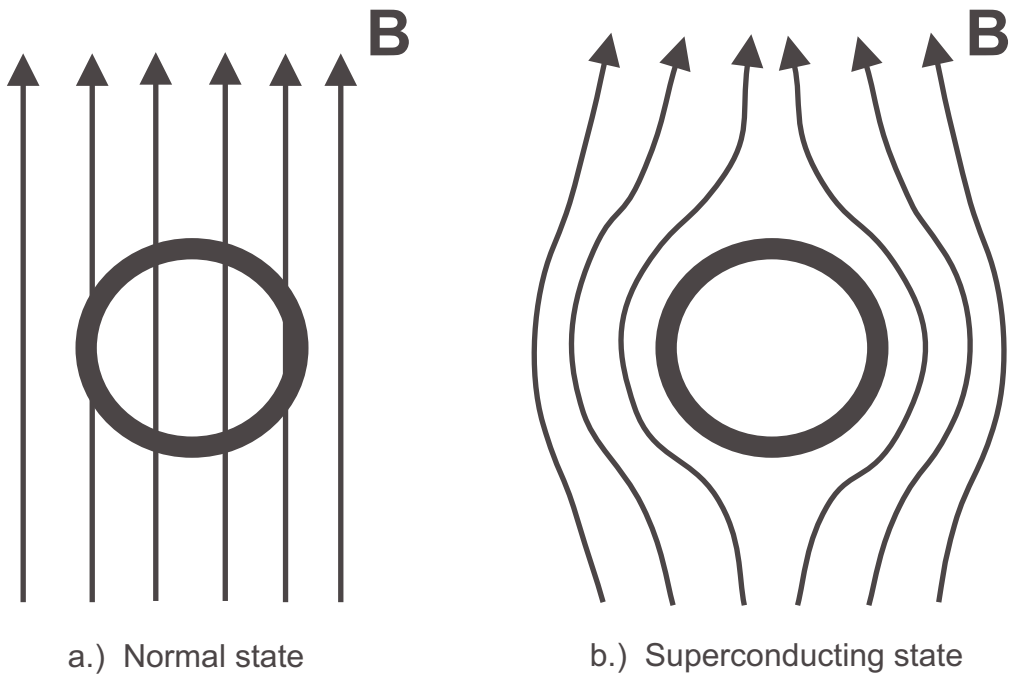

Figure 2.3 The Meissner effect. A static magnetic field permeates a material in the normal state. The magnetic field is expelled when the material is cooled into the superconducting state. Magnetic fields suppress superconductivity because energy is required to expel the flux.

energy associated with superconducting state is increased. In the presence of a magnetic field, the material has to be cooled to a lower temperature in order for the superconducting state to have less free energy than the normal state. Consequently, magnetic fields have the effect of lowering the temperature at which the superconducting to normal-metal phase transition occurs in a superconductor.

For any superconductor at a particular temperature T, there is a critical magnetic field $H_c(T)$. If a magnetic field larger than the critical field is applied to the superconductor, then the superconductor will not superconduct. Instead it will have a finite resistance. An illustration of the temperature dependence of the critical field $H_c(T)$ is shown in Fig. 2.4. The critical field of a superconductor is approximated by

$$H_c(T) \approx H_c(0)(1-(T/T_c)^2). \tag{2.4}$$

Superconductors are affected by externally applied magnetic fields and by magnetic fields from electric current flowing through the superconductor. For any superconducting wire with temperature T, there is a critical electric current $I_c(T)$. If the current conducted through the wire exceeds the critical current $I_c(T)$ then the magnetic field in the wire will exceed the critical field $H_c(T)$ and the wire will be resistive. The critical current of a wire depends both on the critical field $H_c(T)$ and on the shape of the superconducting wire (because the induced magnetic field depends on the current distribution in the wire). The performance of a TES thermometer is greatly affected by the temperature dependence and magnitude of the critical current.

2.3.3 BCS theory: energy gap, heat capacity, and thermal conductivity

The theory of Bardeen, Cooper, and Schrieffer (BCS) provides the basic explanation of superconductivity. In this theory of the superconducting state, it is postulated that

interactions between the electrons and the atomic lattice of a superconductor have the net effect of creating an attractive interaction between the electrons that participate in superconductivity.

In the formulation of BCS theory, Cooper postulated that the attractive potential binds together pairs of electrons with opposite momentum and spin, called Cooper pairs [7]. He showed that the Fermi gas of electrons in a normal state metal is unstable against the formation of a Cooper pair so long as there exists an attractive potential between the paired electrons (even if the attractive force is very small). When a metal is cooled into the superconducting state, electrons that comprise the Fermi electron gas of the normal-metal state form many Cooper pairs. Formation of the Cooper pairs alters the state of the electron gas and lowers its total energy. Cooper pairs continue to form until the state of the electron gas is so altered from the metallic state that formation of additional Cooper pairs no longer lowers the energy of the whole system. Note that electrons are continually exchanged among the Cooper pairs and other unpaired electrons.

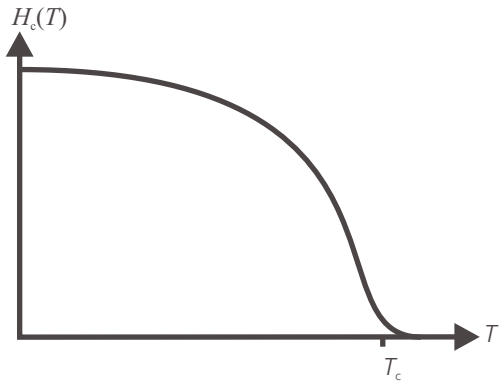

Figure 2.4 The temperature dependence of the critical magnetic field H_c. The critical field is largest at temperature T=0. The critical field decreases as the temperature T approaches the critical temperature T_c. The material is in the superconducting state when the applied magnetic field is less that H_c. In thin films of superconductor, superconductivity does not completely vanish at the critical temperature T_c of the bulk material. Instead, a small critical field persists up to a somewhat higher temperature as illustrated in the figure.

The electrons that are bound in Cooper pairs collectively form the BCS ground state. The BCS ground state is represented by a quantum wave function. The BCS wave function describes the likelihoods of observing various configurations of electrons in the superconductor. Of all the possible quantum states of superconductor, the ground state is the one with the minimum energy. It is the state that a superconductor would occupy if it were at a temperature of absolute zero. Disturbances within the superconductor due to thermal energy, the absorption of photons, or other energy sources can change the configuration of the electrons by creating excitations (so that the electrons are not in the ground state). These excitations are modeled as fictitious particles called quasiparticles. (In actuality, a quasiparticle is a collective mode involving many electrons.) The quasiparticles are fermions that have energy and propagate through the superconductor. A minimum energy per quasiparticle, called the energy gap, is required to create quasiparticles from the ground state. According to BCS theory, the energy gap Δ at a temperature of absolute zero T_c is given by

$$\Delta(0) = 1.76 k_B T_c . \tag{2.5}$$

when there is no magnetic field applied to the superconductor. (In our TES thermometers, the energy gap $\Delta(0)$ is roughly 10 μeV.) The energy gap $\Delta(T)$ decreases to zero as the temperature T of the superconductor approaches the phase transition temperature.

The Cooper pairs of the superconducting state are modeled as bosons. In the superconducting ground state all the Cooper pairs exist in the lowest energy state of the Bose gas of Cooper pairs. A pair of quasiparticles is created when an energetic event breaks up a single Cooper pair. An illustration of the density of quasiparticle states and an excitation event is shown Fig. 2.5. The probability of thermal energy creating an excitation that occupies an energy level with energy E is described by the Fermi function,

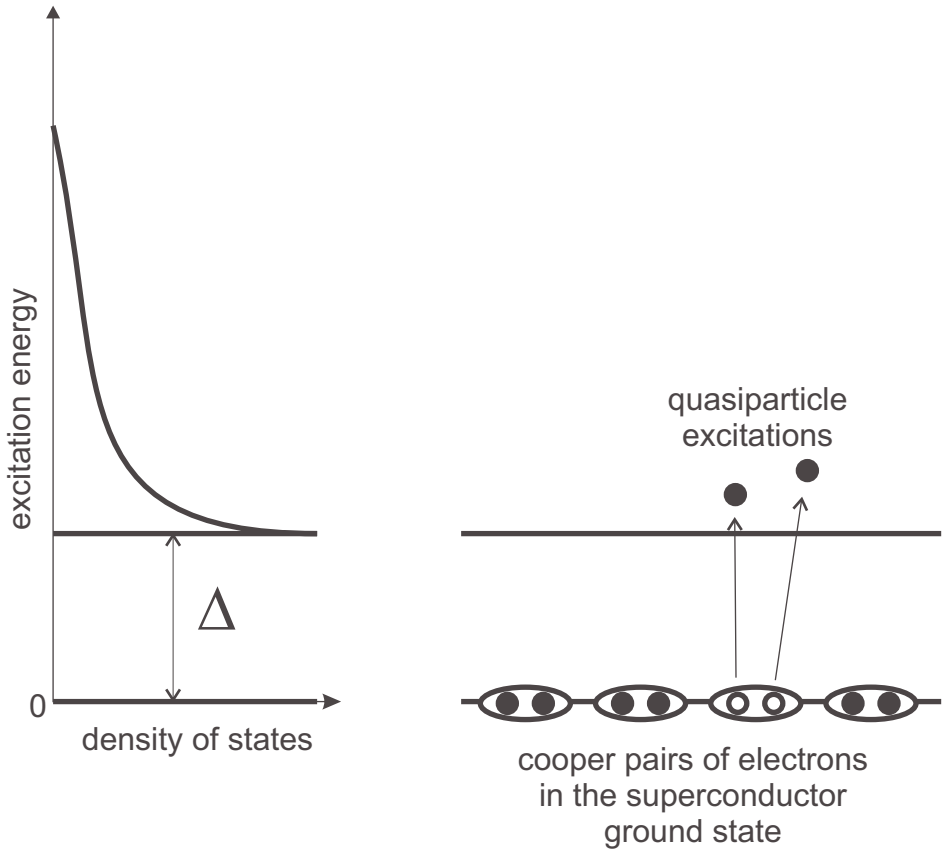

Figure 2.5 Quasiparticle excitations from the superconductor ground state. Quasiparticle excitations are created in pairs. The energy gap Δ is the minium energy of an excitation. In superconductors at temperatures far below the critical temperature T_c, few excitations are created because the thermal energy $k_B T$ is far less than the energy gap Δ. At low temperatures, the electronic heat capacity and thermal conductivity of a superconductor are much smaller than they are in metals in the normal state because there are few quasiparticle excitations.

$$f(E) = \frac{1}{e^{E/k_B T} + 1}. \tag{2.6}$$

The minimum energy E of an excitation is the energy of the gap Δ. At low temperatures, the characteristic thermal energy $k_B T$ is small compared to the energy gap Δ. Consequently, the number quasiparticle excitations decreases exponentially with decreasing temperature.

At low temperature, the superconducting state has small electronic heat capacity and small thermal conductivity compared to the normal metal state because there are relatively few electronic excitations in the superconducting state. The heat capacity of superconductors at temperatures far below T_c is dominated by the heat capacity of the phonon gas in the material. This phonon heat capacity is described by the Debye model:

$$C_{ph} = \frac{12\pi^4}{5} N k_B \left(\frac{T}{\theta_D} \right)^3 , \tag{2.7}$$

where θ_D is the Debye temperature[5].

In our experiments, the thermal properties of superconductors are often used to our advantage. For example, we sometimes use an absorber made of a superconducting metal in our gamma-ray detectors to minimize the heat capacity of the calorimeters. In addition, superconducting electrical wires are used in our refrigerators because they have very low thermal conductivity.

2.3.4 Electrodynamics of BCS superconductors and the London equations

The BCS ground state, which is a quantum phase coherent state, results from the collective interactions of electrons with the atomic lattice. The quantum mechanical properties of the ground state are responsible for the Meissner effect and the lack of electrical resistance in superconductors.

Perturbation theory is used to compute the effects of electromagnetic fields on the BCS ground state. The response of a superconductor to low frequency electromagnetic fields can be computed from the perturbed ground state. From this calculation, the London equations are obtained [8]. The London equations are:

$$\mathbf{E} = \frac{\partial}{\partial t}(\mu_0 \lambda_L \mathbf{J}) \quad \text{and} \tag{2.8}$$

$$\mathbf{B} = \nabla \times (\mu_0 \lambda_L{}^2 \mathbf{J}), \tag{2.9}$$

where λ_L is the London penetration depth, **J** is the supercurrent density, **E** is the electric field and **B** is the magnetic field. Equation (2.8) indicates that electric fields cause the supercurrent to increase until the resulting movement of charge eliminates the electric field in the superconductor. This implies that the current **J** flows without dissipation of energy. By taking the curl of both sides of equation (2.9) and using the expression $\nabla \times \mathbf{B} = \mu_0 \mathbf{J}$ (which is a form of Ampere's Law) to make a substitution, we find that

$$\nabla^2 \mathbf{B} = \mathbf{B} / \lambda_L{}^2 . \tag{2.10}$$

Equation (2.10) implies that the magnetic field is screened exponentially with the penetration depth λ_L into a superconductor. The London penetration depth is typically a very small length. For example, the penetration depth is 16 nm in Al [5]. Consequently, the magnetic field is strongly screened from the interior superconductors (which is the Meissner effect).

2.4 The superconductor-to-normal-state phase transition

When a TES thermometer is in the phase transition, magnetic fields and thermal fluctuations cause the superconducting state to vary as a function of position in the superconductor. For example, regions of normal metal may lie next to regions of superconducting metal. The BCS theory, as originally formulated, is not equipped to handle such variation. Such situations are better described using the theory of Ginzburg and Landau.

2.4.1 The Ginzburg-Landau theory

The Ginzburg Landau (GL) theory describes spatial variations in superconducting state associated with spatial variation of the energy gap Δ. The theory describes the superconducting ground state in terms the order parameter ψ. The order parameter is a complex valued scalar function of spatial location **x** in the superconductor.

$$\psi(\mathbf{x}) = |\psi(\mathbf{x})| e^{i\varphi(\mathbf{x})} \tag{2.11}$$

The magnitude $|\psi(\mathbf{x})|^2$ is the local density of superconducting electrons and is proportional to the energy gap Δ. The order parameter has a phase φ that describes the quantum phase the superconducting state and is also related to the supercurrent density **J**. Because the superconducting state is a coherent state with quantum phase φ, superconductors manifest many quantum mechanical properties, such as quantum interference and quantization of magnetic flux.

A time dependent change in the phase difference $\Delta\varphi$ between two ends of a superconductor is associated with a voltage across the two ends. This property of superconductors is described by the Josephson relation:

$$\frac{d}{dt}\Delta\varphi = \frac{2eV}{\hbar}. \tag{2.12}$$

The GL coherence length ξ is defined as the smallest distance scale over which the order parameter ψ can very. The phase φ, the GL coherence length ξ, and Josephson relation of equation (2.12) are used to describe phenomena occurring in our TES thermometers.

2.4.2 Flux quantization

The interaction between superconductors and magnetic fields that permeate them must be first understood before attempting to describe the physics of TES thermometers in the phase transition. As an example, we consider the case of magnetic flux passing through a hole in a superconducting ring as shown in Fig. 2.6. The magnetic flux penetrating the ring is $n\Phi_0$, where Φ_0 is the flux quantum:

$$\Phi_0 = h/2e = 2.07\times10^{-15}\,\mathrm{Wb}\,. \tag{2.13}$$

The phase φ of the superconductor is rotated by $2n\pi$ as measured around the ring. The order parameter ψ, which depends on the phase φ modulus 2π, must be a single valued function. Therefore n must be an integer. Consequently, the flux passing through the superconducting ring must be an integer multiple of the flux quantum Φ_0. This example is important because magnetic flux can penetrate our TES thermometers, resulting in a similar situation.

2.4.3 Abrikosov flux vortices

Abrikosov [9] analyzed GL theory, to show that there are really two classes of superconductors. One class expels magnetic flux (type I) as illustrated in Fig. 2.3. In type I superconductors, the free energy is minimized by having the minimum possible surface area of the superconducting state to normal state boundary. The second class of superconductors (type II) allows tubes of magnetic flux to penetrate the superconductor as illustrated in Fig. 2.7. The magnetic flux is quantified just as it is in the ring of Fig. 2.6. The free energy is minimized when magnetic flux passes through flux tubes in the superconductor each containing one flux quantum. In the center of each flux tube, there is a region with a diameter of the GL coherence length ξ that is approximately in the normal state. The flux tubes are called Abrikosov vortices.

The material composition of a bulk superconductor determines weather it is type I or type II. However, films of superconductor that are much thinner than the GL coherence length ξ always demonstrate type II behavior. Such is the case for our TES thermometers, which are composed of thin metal films. Therefore, Abrikosov vortices occur in our TES thermometers.

2.4.4 Vortex motion and dissipation

The flux vortices in a superconductor are held in place by pinning sites in the superconductor. Pinning is caused by imperfections in the superconducting material. The presence of a supercurrent density **J** causes the Abrikosov vortices to move in a direction perpendicular to the electric current **J**. The vortices move only if the Lorentz force between the supercurrent and the magnetic field of the vortex exceeds the pinning force.

Vortex motion in a superconducting wire causes a voltage potential V to form across the wire. This occurs because the motion of flux vortices in a direction perpendicular to the

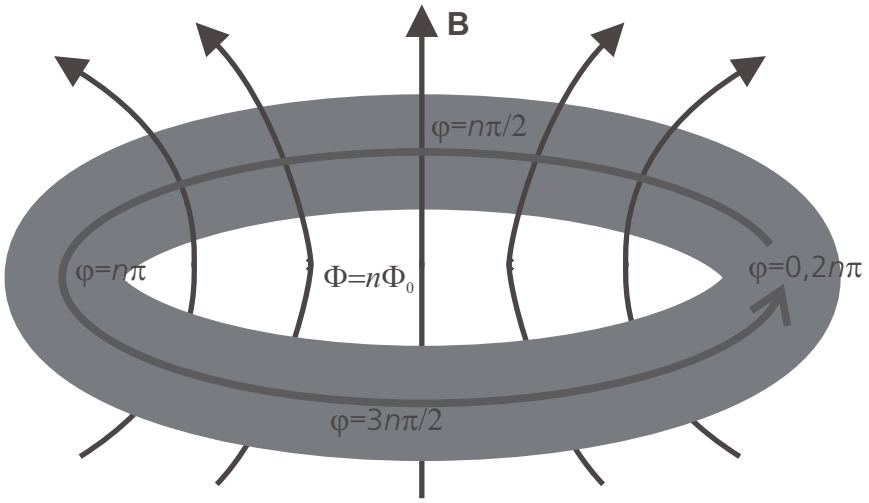

Figure 2.6 Magnetic flux passing through a superconducting ring. The total magnetic flux threading the ring must be a multiple of the flux quantum Φ_0 so that the order parameter Ψ of the superconductor is single valued.

supercurrent causes the phase φ_1 to change on one side of the wire relative to the phase φ_2 of the other side. The rate of change of the phase difference $\Delta\varphi = \varphi_2 - \varphi_1$ determines the voltage across the wire, as described by equation (2.12). For example the lateral motion of a single vortex from on side of a wire to the other side causes the relative phase $\Delta\varphi$ to change by π.

Vortex motion also causes dissipation: if the supercurrent *I* through a superconducting wire induces vortex motion that causes a voltage *V* across the wire, then the power dissipated is $P = IV$. This mechanism is responsible for dissipation in our TES thermometers when they are biased in the transition between the superconducting and normal states. Notice that the mechanism of dissipation in the superconducting state is very different from the

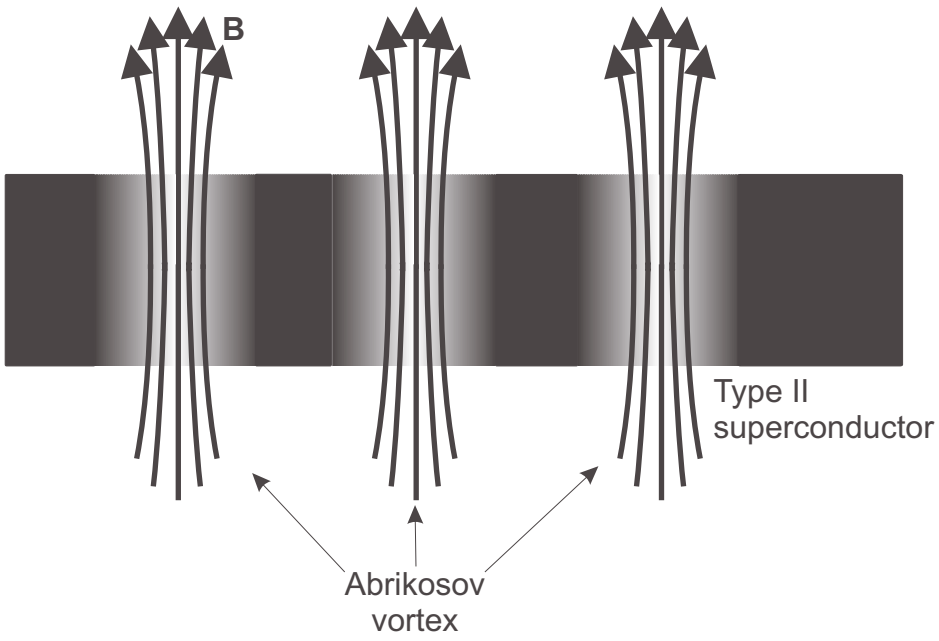

Figure 2.7 Abrikosov vortices in a laminar superconductor as shown in cross section. Superconductivity is suppressed (indicated by light grey) where the magnetic field permeates the superconductor.

mechanism in the normal state.

2.4.5 Fluctuations and dissipation in the phase transition

The appearance of resistance in a TES as it is warmed from the superconducting state into the phase transition is associated with thermal fluctuations in the superconducting state. At temperatures less than several mK below the critical temperature T_c, these fluctuations occur so rarely that they not observable. In the absence of such fluctuations, the superconductor has zero resistance. The energy required to create fluctuations in the superconducting state decreases as the temperature is increased. As the temperature of a superconductor is increased to temperatures near T_c, the rate of fluctuations in the superconducting state increases sharply[8].

These fluctuations are very different from quasiparticle excitations. Thermal fluctuations in the superconducting state cause the phase of one side of the TES to slip with respect to the other side. For example, thermal fluctuations in a TES can lead to the creation of flux vortices. When a current I is conducted through the TES, the motion of the flux vortices causes phase slipping and dissipation. Hence the resulting phase slips generate a voltage V across the TES. If thermal fluctuations create uncorrelated phase slips of magnitude $\Delta\varphi$ then the associated voltage noise is

$$\left|V_{\mathrm{VN}}(0)\right| = \sqrt{\frac{\phi_0 \Delta\varphi}{\pi} V} \tag{2.14}$$

[10]. In general, the noise of uncorrelated phase slips is at least as large as the Johnson noise limit. The actual magnitude of the phase slips depends on the vortex dynamics in the superconductor. If each fluctuation creates a vortex that crosses the width of the superconductor, then $\Delta\varphi = \pi$. If the vortices are bound large bundles, then each flux bundle may cause a much larger phase slip. In the other hand, the vortices only partly cross

the superconductor before being annihilated by a vortex of opposite magnetic field, then each phase slip event will be less than π.

The energy gap $\Delta(T)$ becomes very small as the temperature T of a superconductor is increased to the critical temperature T_c. When the energy gap is small compared to $k_B T$, many thermal quasiparticle excitations occur. Consequently, the electronic heat capacity and thermal conductivity become much larger as the temperature of a superconductor approaches T_c. In fact, the heat capacity of a superconductor at temperature T_c equals 2.43 times the heat capacity of the normal state electrons at the same temperature according to BCS theory [8]. At temperatures slightly above T_c, the heat capacity of superconductor decreases to the normal state heat capacity. We often estimate the heat capacity and thermal conductivity of our TES thermometers in the phase transition by using the calculated values of the heat capacity and thermal conductivity in the normal metal state, multiplied by the factor 2.43.

[1] J. B. Johnson, "Thermal Agitation of Electricity in Conductors," Physics Review **32**, 97-109 (1928).

[2] H. Nyquist, "Thermal Agitation of Electric Charge in Conductors," Physics Review **32**, 110-113 (1928).

[3] H. B. Callen, "Irreversibility and Generalized Noise," Physical Review **83** (1), 34-40 (1951).

[4] F. Reif, *Fundamentals of statistical and thermal physics* (McGraw-Hill, New York, 1965).

[5] Charles Kittel, *Introduction to solid state physics* (Wiley, New York, 1986).

[6] H. K. Onnes, Comm. Phys. Lab., University of Leyden **120b, 122b, 124c** (1911).

[7] L. N. Cooper, Physics Review **104**, 1189 (1956).

[8] Michael Tinkham, *Introduction to superconductivity* (McGraw Hill, New York, 1996).

[9] A. A. Abrikosov, Sov. Phys.--JETP **5**, 1174 (1957).

[10] C. M. Knoedler, "Phase-slip shot noise contribution to excess noise in superconducting bolometers," Journal of Applied Physics **54** (5), 2773-6 (1983).

Chapter 3

THERMAL PHYSICS AND THE TRANSITION-EDGE-SENSOR CALORIMETER

3.1 Introduction to the transition-edge-sensor

A transition-edge sensor (TES) is a very sensitive thermometer. Typically, the TES thermometer consists a small rectangular thin film of superconductor. (The typical dimensions of TES thermometers in our x-ray microcalorimeters are 100 μm $\times$ 200 μm $\times$ 0.1 μm). A bilayer of two metals (copper and aluminum) is used to form our TES thermometers. The total thickness of the film is less than the GL coherence length. Such thin films behave much as if they are made of one superconductor with properties that depend on the two metal film thicknesses. The thicknesses of the films determine the critical temperature T_c of the superconductor to normal metal phase transition.

Our TES thermometers are fabricated on top of silicon substrates. The silicon substrate acts as a large thermal reservoir, or cold bath. In our experiments, the substrates are cooled to a temperature T_{bath} below the critical temperature T_c of the TES so that the TES superconducts. A bias voltage is applied to the TES. The resulting electric current increases until the critical current I_c of the superconductor is exceeded and the TES becomes resistive. A small bias voltage is chosen so that the resulting Joule heating (which warms the TES) and magnetic fields (which lower the temperature of the phase transition)

do not drive the TES completely into the normal metal state. The TES is held in the phase transition between the superconducting and normal metal states.

In the phase transition, the resistance R of the TES increases rapidly with increasing temperature T of the TES due to fluctuation phenomena as described in Chapter 2. A plot of resistance versus temperature is shown in Fig. 1.5. In the transition, the TES is a very sensitive thermometer. We use TES thermometers in our x-ray microcalorimeters to measure photon absorption events as described in Section 1.3. In this chapter, we shall review thermal physics relating to stable, low noise operation of TES microcalorimeters.

3.2 The coupling of the TES to a cold bath

In abutting bulk materials, the thermal coupling between the phonons of the different materials is described by the acoustic mismatch between the materials. In materials with differing acoustic impedances, acoustic waves (phonons) are reflected at the boundary between two materials. The associated thermal conductance across a boundary between two materials is called the Kapitza coupling.

However, our TES thermometers are so thin that they can not be regarded as bulk materials. The thickness of a TES is smaller than the typical wavelength of thermal phonons at 100 mK [1]. Consequently, the phonons are not efficiently reflected at the boundary between the TES and the silicon substrate on which it rests. Therefore, phonons are readily exchanged between such a thin film the substrate. In our microcalorimeter design shown in Fig. 1.6, part of our TES thermometers lies on the substrate. The phonons in that part of the device are well coupled to the thermal reservoir at temperature T_{bath}. Hence the Kapitza coupling is large for such thin films [1].

At the temperatures we operate our devices, the coupling between the electrons and the phonons in a TES is relatively weak compared to the Kapitza coupling. The electron-phonon coupling in copper has been measured. The coupling power is described by the equation

$$P_{e-p} = \Sigma\Omega\left(T^N - T_{\text{bath}}{}^N\right), \tag{3.1}$$

where N=5, $\Sigma \cong 1\times10^9\,\text{WK}^{-5}\text{m}^3$, T is the temperature of the electrons, T_{bath} is temperature of the phonons, and Ω is the volume in which the electron phonon coupling occurs [1-3]. The thermal coupling is $G \equiv \partial P / \partial T$. In our devices, the volume Ω is the volume of the TES that lies directly on the silicon substrate. The electron phonon coupling determines the coupling between the microcalorimeter and the cold bath.

3.3 Constraints on the normal-state resistance of TES thermometers

In operation, electric current I flows through a TES thermometer. Joule heating from the electric current warms the TES and holds the TES in the phase transition. However, the Joule heating from the current can cause spatial instability in the TES.

As an example, we shall examine the effects of Joule heating in a TES in which the width and thickness of the TES are small compared to the GL coherence length ξ. In this case, the TES may be regarded as being a one dimensional wire. In this example, the thermal coupling g (per volume element) to the bath and the specific heat capacity c are constant with respect to position in the wire x and temperature $T(x)$ of the TES. The thermal conductivity κ of the TES is also constant. The temperature of the substrate T_{bath} is held constant at a temperature less than the critical temperature T_c of the TES. A constant

current density J is conducted through TES. The current causes Joule heating that elevates the temperature $T(x)$ of TES above the bath temperature T_{bath}. The electrical resistivity ρ is a function of the temperature T. (The current dependence of the resistivity ρ is neglected because the current density J is constant.) The differential equation that describes the rate of change of the temperature in the TES with time t is

$$c\frac{dT}{dt} = -g_{\text{bath}}(T - T_{\text{bath}}) + J^2\rho(T(x)) - \kappa\frac{\partial^2 T}{\partial x^2}. \tag{3.2}$$

The first term on the right side of equation (3.2) describes the cooling power in the substrate. The second term describes the Joule heating power within the TES. The third term describes thermal conduction within the TES.

At equilibrium, the temperature $T(x)$ is constant with respect to position x and equal to T_0. The equilibrium electrical resistance is ρ_0. For small perturbations in temperature T from equilibrium temperature T_0, the resistance can be approximated by

$$\Delta\rho(x) \cong \left.\frac{\partial\rho}{\partial T}\right|_{I,T_0} \Delta T(x) = \rho_0\alpha'\frac{\Delta T(x)}{T_0}, \tag{3.3}$$

where $\Delta\rho(x) \equiv \rho(x) - \rho_0$, $\Delta T(x) \equiv T(x) - T_0$, and $\alpha' \equiv (T_0/\rho_0)\partial\rho/\partial T$. Equation (3.2) then reduces to the linear differential equation:

$$\frac{d}{dt}\Delta T = \left(\frac{1}{\tau_{e\text{ff}}} + \frac{\kappa}{c}\frac{\partial^2}{\partial x^2}\right)\Delta T, \tag{3.4}$$

where the effective thermal time constant is

$$\frac{1}{\tau_{\text{eff}}} \equiv -\frac{g}{c} + \frac{J^2 \rho_0}{cT_0} \alpha' . \tag{3.5}$$

When the TES is operated with a large current density J, the Joule heating dominates over the cooling to the bath. Therefore, we make the approximation that

$$\frac{1}{\tau_{\text{eff}}} \cong \frac{J^2 \rho_0}{cT_0} \alpha' . \tag{3.6}$$

We assume that the power of the cooling is described by equation (3.1). The equilibrium power p_0 is given by

$$p_0 = J^2 \rho_0 = \Sigma\Omega(T^N - {T_{\text{bath}}}^N) . \tag{3.7}$$

Using $g \equiv \partial p / \partial T = N p_0 / T_0$ we find that

$$J^2 \rho_0 \cong g T_0 / N , \tag{3.8}$$

where we have made the approximation that $T^N >> {T_{\text{bath}}}^N$. This approximation is valid when Joule heating, due to large current in the TES, elevates the temperature far above the bath temperature. In this approximation, equation (3.6) becomes

$$\frac{1}{\tau_{\text{eff}}} \cong \frac{g}{c} \frac{\alpha'}{N} . \tag{3.9}$$

Assuming that no heat is conducted out of the ends of the TES, the solution of equation (3.4) is subject to the constraint that $\partial T / \partial x = 0$ at $x = 0$ and $x = l$. The solution is written as a sum of cosine components with wavelengths $\lambda = 2l / n$:

$$\Delta T = \sum_{n=1}^{\infty} T_n \exp\left[\left(\frac{1}{\tau_{\text{eff}}} - \frac{\kappa}{c}\left(\frac{n\pi}{l}\right)^2\right)t\right]\cos\left(\frac{n\pi x}{l}\right). \tag{3.10}$$

The *n*th component with decrease exponentially with time if

$$\frac{1}{\tau_{\text{eff}}} - \frac{\kappa}{c}\left(\frac{n\pi}{l}\right)^2 < 0\,. \tag{3.11}$$

The thermal conductivity κ of a TES in the phase transition is approximately is given by the Wiedemann-Franz law of equation (2.4), which is written as

$$\kappa = LT/\rho_{\text{n}}\,, \tag{3.12}$$

where L is the Lorenz number an ρ_{n} is the normal state resistivity.

If the n=1 component of equation (3.10) is stable, then all the components in which n>1 are also stable. For the case that n=1, equation (3.11) is rewritten as

$$\rho_{\text{n}} l < \frac{\pi^2 LT}{gl}\left(\frac{N}{\alpha'}\right) \tag{3.13}$$

where we made substitutions using approximation (3.9) and equation (3.12). We divide both sides of equation (3.13) by the cross sectional area of the TES to find that the normal state resistance R_{N} of the TES is constrained by

$$R_{\text{N}} < \frac{\pi^2 LT}{G}\left(\frac{N}{\alpha'}\right), \tag{3.14}$$

where G is the thermal conductance between the TES and the substrate. (Equation (3.14) is stated in a paper by Kent Irwin [4]. The computation was first described to me by Blas Cabrera [5].)

We have now obtained a constraint on the normal resistance of a TES. Using the values of Table 3.1, we find that the normal resistance R_N of the TES must be less than 1 Ω for the TES to be stable when operated at high power. If the normal resistance is greater than 1 Ω, then Joule heating causes spatial temperature variations to increase with time rather than decrease.

Parameter	**Typical value**	**Typical variation in value**
α'	100	5
L	2.4×10^{-8} WΩ / K^2	5
G	1 nW / K	10
N	5	1.25
T	100 mK	1.5
$R_N < \frac{\pi^2 LT}{G}\left(\frac{N}{\alpha'}\right)$	$R_n < 1$ Ω	25

Table 3.1 The values typically used in determining the resistance limit of a TES. The typical values are estimated for a TES in a x-ray microcalorimeter operated at about 100 mK. An illustration of such a microcalorimeter is shown in Fig. 1.6. In any particular x-ray microcalorimeter, each of the values can vary from the estimated values of this table by significant factors listed in the third column. For the "typical" x-ray microcalorimeter, we find that the normal resistance must less than 1 Ω. For other x-ray microcalorimeters, this estimate may be off by 25 times.

As indicated in Table 3.1, the estimate may vary by a factor of 25 depending of the particular microcalorimeter. (Here, I have assumed that the errors multiply. Therefore, the errors of each of the terms add in quadrature only after the logarithm of both sides of equation (3.14) is taken.) The 1 Ω upper limit of the normal resistance is a crude estimate based on a number of approximations: the TES was approximated as being a one dimensional wire, the thermal conductivity was estimated from the Wiedemann-Franz Law, the energy associated with the formation of domain boundaries between superconducting and normal regions was neglected, and the thermal coupling was estimated from values of "typical" x-ray TES microcalorimeters. Nevertheless, real TES thermometers do suffer from spatial instability due to Joule heating. To minimize the effect, we try to keep thermal conductance across the TES as large as reasonably possible. Consequently, we design our TES thermometers to have an electrical resistance less than 1 Ω.

Calculations of resistance fluctuations in two dimensional resistive thermometers have been carried out by Voss and Clarke [6,7]. They found that resistance fluctuations can result in $1/f$ noise. In general, the spatial instability is less severe in two dimensional TES thermometers than it is in one dimension because the electric current is free to wind around highly resistive hot spots in two dimensions.

Experimental concerns place a lower limit on the resistance of the TES thermometer. Our TES thermometers are measured with a bias circuit as shown in Fig. 4.2. The contact points between the wires and other elements in the circuit contribute a small parasitic resistance of about 10 mΩ. The normal resistance of the TES should be much larger than the parasitic resistances. Based on the these considerations, we have usually designed our TES thermometers to have a normal state resistance R_n of several hundred mΩ.

3.4 The effective temperature and the thermodynamic energy resolution

As previously described, a microcalorimeter is thermally coupled to a large heat reservoir maintained at constant temperature T_{bath}, called the cold bath. An illustration of the thermal coupling is shown in Fig. 3.1. The thermal conductance G between the microcalorimeter and bath is the dominate thermal coupling between the microcalorimeter and the environment. The internal energy within a calorimeter fluctuates due the random, thermodynamic exchange of energy between the calorimeter and the bath. A thermometer, such as a TES, is used to measure changes in internal energy U of a microcalorimeter. Note that even when the temperature of a microcalorimeter is constant, the measurements made by a thermometer will fluctuate due to thermodynamic noise. This occurs because thermometers actually measure thermal energy, not temperature. (The *average* energy in a thermometer corresponds to a particular temperature.)

The thermodynamic fluctuations of the internal energy are a form of noise in the microcalorimeter. These fluctuations, when combined with other noise, limit the energy resolution of a microcalorimeter. We shall now present a calculation of the thermodynamic fluctuations in a microcalorimeter in thermal equilibrium with the bath so that the microcalorimeter temperature T equals the bath temperature T_{bath}.

In this calculation, we divide the space of all possible microscopic states of the system (which includes the bath and the microcalorimeter) into groups, with each group defining a macrostate. Each macrostate of the system corresponds to the microcalorimeter having internal energy U_1 and the bath having internal energy U_2.

The parameter Ω_1 is the number of microstates of the microcalorimeter that have internal energy U_1. The entropy of the microcalorimeter is given by $S_1 = k_B \ln \Omega_1$. Likewise, the

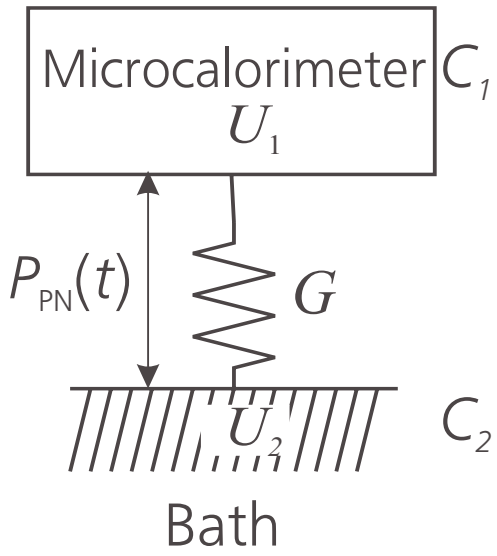

Figure 3.1 The thermal coupling between the microcalorimeter and the bath. The thermal coupling is associated with thermal noise in the microcalorimeter. The thermal noise causes the internal energy of the calorimeter to fluctuate. The transport of energy between the microcalorimeter and the bath is represented by a power source $P_{PN}(T)$.

parameter Ω_2 is the number of microstates of the bath that have internal energy U_2. The entropy of the bath is given by $S_2 = k_B \ln \Omega_2$.

The effective temperature of the microcalorimeter is defined by

$$T_1 = \partial U_1 / \partial S_1 . \tag{3.15}$$

The actual temperature T of the microcalorimeter must remain constant according to the zeroith law of thermodynamics. However, the effective temperature T_1 fluctuates with time as the microcalorimeter wanders from macrostate to macrostate.

Rewriting equation (3.15) as $\Delta S_1 = \Delta U_1 / T_1$ and taking the derivative with respect to temperature results in

$$\frac{\partial S_1}{\partial T} = \frac{\Delta U_1}{\Delta T_1}\frac{1}{T_1} = \frac{C_1}{T_1} \cong \frac{C_1}{T}, \tag{3.16}$$

where $C_1 = \partial U_1 / \partial T_1$ is the heat capacity if the microcalorimeter. We have made the approximation that the effective temperature T_1 approximately equals temperature T because the fluctuations in T_1 are small.

The probability of finding the system in a macrostate with energies U_1 and U_2 is proportional to the number ($\Omega = \Omega_1 \cdot \Omega_2$) of associated microstates because the system is equally likely to visit any particular microstate. The entropy of the system is $S = S_1 + S_2$. The probability of finding the system in a macrostate with entropy *S* is given by

$$p \propto \Omega \propto \exp(\Delta S / k_B) \tag{3.17}$$

where $\Delta S \equiv S - \langle S \rangle$. The entropy $\langle S \rangle$ is the equilibrium value of the entropy *S*. We also define $\Delta S_1 \equiv S_1 - \langle S_1 \rangle$ and $\Delta S_2 \equiv S_2 - \langle S_2 \rangle$. Fluctuations in the entropy *S* are related to fluctuations in the entropy of the bath and microcalorimeter by the following equation:

$$\Delta S = \Delta S_1 + \Delta S_2 . \tag{3.18}$$

The fluctuations in energy of the microcalorimeter correspond to negative fluctuations in the energy of the bath because energy is conserved: $\Delta U_1 = -\Delta U_2$, where $\Delta U_1 = U_1 - \langle U_1 \rangle$ and $\Delta U_2 = U_2 - \langle U_2 \rangle$. From the Second law of thermal dynamics, $\Delta S = \Delta U / T$, we find

$$\Delta S_2 = \Delta U_2 / T = -\Delta U_1 / T . \tag{3.19}$$

The energy ΔU_1 of the microcalorimeter is expressed as a function of entropy S_1 using a Taylor expansion:

$$\Delta U_1 = \frac{\partial U_1}{\partial S_1}\Delta S_1 + \frac{1}{2}\frac{\partial^2 U_1}{\partial {S_1}^2}\left(\Delta S_1\right)^2 + \cdots \quad , \tag{3.20}$$

where we retain terms up to second order. We now express fluctuations in the entropy of the microcalorimeter in terms of fluctuations in the effective temperature:

$$\Delta S_1 = \frac{\partial S_1}{\partial T_1}\Delta T_1 = \frac{C_1}{T}\Delta T_1 , \tag{3.21}$$

where $\Delta T_1 = T_1 - T$. Using equations (3.15), (3.20) and (3.21) we obtain,

$$\Delta U_1 = T\Delta S_1 + \frac{1}{2}\frac{C_1}{T}\left(\Delta T_1\right)^2 . \tag{3.22}$$

Using equations (3.17), (3.19), and (3.22) we find that

$$p \propto \exp\left(\frac{-C_1\left(\Delta T_1\right)^2}{2k_{\mathrm{B}}T^2}\right). \tag{3.23}$$

Equation (3.23) describes the probability of the microcalorimeter having the effective temperature T_1. Apparently, equation (3.23) indicates that the effective temperature T_1 forms a Gaussian distribution centered on temperature T with standard deviation

$$\sigma_{T1} = \sqrt{\frac{k_{\mathrm{B}}T^2}{C_1}} \tag{3.24}$$

Fluctuations in the effective temperature are related to energy fluctuations by $\Delta U_1 = C_1 \Delta T_1$. Therefore, the standard deviation of the energy fluctuations is $\sigma_{U1} = (k_B T^2 C_1)^{1/2}$ [8]. The full-width-half-max of width of the energy fluctuations is

$$\Delta U_{\mathrm{FWHM}} = 2.35\sqrt{k_B T^2 C_1} \tag{3.25}$$

Equation (3.25) relates the temperature and heat capacity of a microcalorimeter to fluctuations in the internal energy.

In basic thermodynamic texts, the above result is often proved using Maxwell-Boltzmann statistics. However, it is important to include the above calculation in this thesis for two reasons. First, the above calculation makes it clear that equation (3.25) applies to any microcalorimeter regardless of the quantum statistics involved. In the above calculation, no assumption was made with regard to the type of quantum statistics that apply to the gas inside the microcalorimeter: it applies to Maxwell-Boltzmann, Fermi-Dirac, or Bose-Einstein statistics. It even applies to calorimeters that contain both a Bose gas and a Fermi gas. This is important because the heat capacity of a microcalorimeter is dominated by either fermions or bosons depending on whether the absorber is a metal or dielectric. Second, the above calculation demonstrates the difference between the effective temperature and actual temperature. The effective temperature is a measure of the internal energy of the calorimeter as in the above calculation. Thermometers measure effective temperature, not actual temperature. The actual temperature is the effective temperature averaged over a large ensemble of identical systems. (Note that the temperature is not a time average of the effective temperature in one system because the temperature may vary with time.)

3.5 Thermal noise

The thermal energy fluctuations, which were described in Section 3.4, correspond to energy being exchanged between the bath and the microcalorimeter. The energy exchange causes a power $P(t)$ to be transferred from the bath into the microcalorimeter as illustrated in Fig. 3.1. The power is frequency independent because the energy exchange is a frequency independent process. The power needed to generate the fluctuations in energy ΔU_{FWHM} in the microcalorimeter, depends on the thermal conductance G between the bath and the microcalorimeter. The power is given by

$$\left\langle \left| P_{\mathrm{PN}}(f) \right|^2 \right\rangle = 4 k_{\mathrm{B}} T^2 G \,. \tag{3.26}$$

If the bath temperature T_{bath} is not equal to the temperature T of the microcalorimeter, the power of the thermal noise is

$$\left\langle \left| P_{\mathrm{PN}}(f) \right|^2 \right\rangle = 2 k_{\mathrm{B}} \left(T^2 + {T_{\mathrm{bath}}}^2 \right) G \tag{3.27}$$

[9,10]. This thermal noise is often called *phonon* noise by people in our field because it is often associated with the exchange of phonons between the microcalorimeter and a thermal reservoir. In our calorimeters, the heat capacity is dominated by the electrons. Therefore, the thermal noise is actually dominated by exchange of the energy between the electrons in the calorimeter and phonons in the bath.

3.6 Exceeding the thermodynamic energy resolution

One might expect that the energy resolution of a calorimeter of temperature T and heat capacity C_1 can not be better than the scale of the thermodynamic fluctuations in the

microcalorimeter ΔU_{FWHM}, which is described by equation (3.25). However, it is possible to measure energy fluctuations smaller than ΔU_{FWHM} with a calorimeter. An illustration of how this is possible is given in Fig. 3.2. The internal energy of the calorimeter fluctuates by an amount ΔU_{FWHM} over long time intervals. However, the internal energy of the calorimeter is correlated over time intervals shorter than the thermal time, $\tau_{\mathrm{th}} = C_1 / G$. Therefore, the internal energy of a calorimeter fluctuates less over shorter time intervals. Measurements of the microcalorimeter energy that take place over time intervals much smaller than τ_{th} can achieve much higher energy resolution than ΔU_{FWHM}.

When TES based x-ray microcalorimeters are operated at low power, the response of the microcalorimeter to the absorption of an x ray is a pulse in temperature (as shown in Fig. 1.3) which has a decay time τ_{th}. In this case, the ratio of signal to electronic noise is small for frequencies higher than frequency $f_{\mathrm{th}} = 1/(2\pi\tau_{\mathrm{th}})$. The bandwidth of the measurement extends approximately from zero frequency up to the frequency f_{th}. Therefore, measurement occurs on time scales comparable to τ_{th}. This results in an energy resolution approximately equal to the thermodynamic fluctuations of equation (3.25).

When a sensitive TES is operated at sufficiently high power, the gain of the calorimeter boosts the signal over the noise for a range of frequencies. In addition, electrothermal feedback in the microcalorimeter causes the pulses to be shortened or the effects Johnson noise to be reduced significantly, as will be described in Chapter 4. In these cases, the signal dominates over the electronic noise in a bandwidth that extends from zero frequency to frequencies higher than f_{th}. The bandwidth in which the signal dominates over the noise increases with α' [10,11]. Therefore, a TES microcalorimeter with $\alpha' >> 1$ can far exceed the thermodynamic energy resolution, which is described by equation (3.25). The resolution of a microcalorimeter will be discussed further in Chapter 4.

3.7 Design criteria

We design our TES microcalorimeters to obtain high energy resolution and high quantum efficiency. In optimizing the design of our calorimeters, we must consider their thermodynamic properties. Some of the more important factors influencing detector design are:

- **Thermodynamic noise**. The heat capacity and temperature of a microcalorimeter must be small to minimize the noise from thermodynamic fluctuations as described in Section 3.4. Our heat capacity is chosen to be approximately 1 pJ/K so that we can achieve an energy resolution of approximately several eV at 100 mK for a moderately sensitive TES.

- **Thermal conductance within the TES**. Our TES thermometers are designed to have a normal state electrical resistance of approximately 0.1 Ω. Larger resistance causes poor

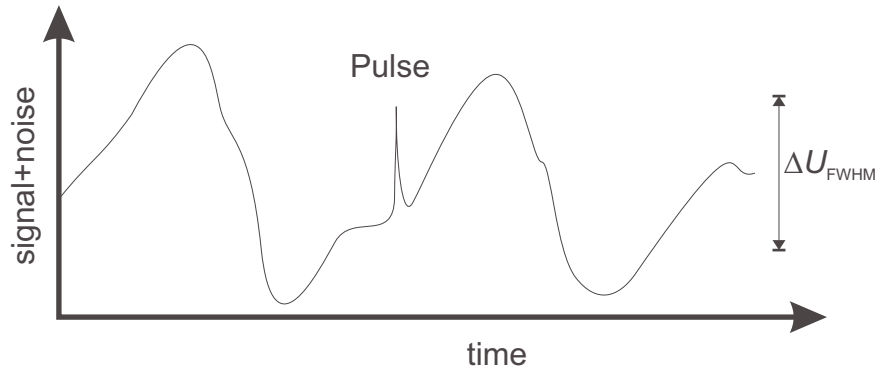

Figure 3.2 Thermodynamic fluctuations and energy resolution. In the figure, a small pulse is shown in the presence of larger noise. The noise is generated by internal fluctuations of a microcalorimeter. Fluctuations of magnitude ΔU_{FWHM} occur over time scales longer than $\tau_{th}=C_1/G$. Electrothermal feedback in a microcalorimeter can cause pulses to be shorter than τ_{th}. In this figure, absorption events with energies less than ΔU_{FWHM} are easily distinguished from the noise because much of the associated signal occurs at higher frequencies than does the majority of the noise. Even without pulse shortening, the energy resolution can exceed the thermodynamic limit if the signal dominates over the noise in a bandwidth larger than $G_1/2\pi C$. Electrothermal feedback, pulse shortening, signal, and noise are described in detail in Chapter 4.

thermal conductivity in the TES, which leads to spatial instabilities as described in Section 3.3.

- **Thermal conductance between the microcalorimeter and the bath**. The number of x rays a calorimeter can measure per second is limited by the decay time of the pulses produced by the microcalorimeter. The decay time is determined by thermal time *C/G* and other factors as will be described in Chapter 4. Microcalorimeters with larger thermal conductance *G* have faster count rates. However, if the thermal conductance *G* is too large, then the heat will leak out of the microcalorimeter before the signal can be recorded. We design our microcalorimeter to have coupling to the bath *G* between 1 to 10 pJ/K so that we can count at a rate of hundreds of counts per second. The value of the thermal conductance *G* is determined by the volume of the TES that lies on top of our silicon substrate as described in Section 3.2.

- **Thermal diffusion in the absorber and TES**. Heat must diffuse throughout a microcalorimeter on a much shorter time scale than the decay time of a pulse from the microcalorimeter. Otherwise, the amplitude of the pulses will be reduced, energy resolution will be degraded, and absorption events occurring in different places in the observer will cause differing responses in the microcalorimeter. I designed our microcalorimeters so that heat is able to diffuse across the length of the microcalorimeter in several microseconds. The thermal conductivity in the metals films of our microcalorimeters limits their size to be no larger than several hundred microns. (An estimate of the thermal conductivity is obtained from the Wiedemann-Franz law (2.4), using the measured electrical conductivity of our metal films.)

We shall describe the design of these devices further in Chapter. 5.

[1] F. C. Wellstood, C. Urbina, and J. Clarke, "Hot-Electron Effects in Metals," Physical Review B-Condensed Matter, 5942-5955 (1994).

[2] A. C. Anderson and R. E. Peterson, "The thermal resistance between electrons and phonons in copper," Physics Letters A **38a** (7), 519-20 (1972).

[3] M. L. Roukes, M. R. Freeman, R. S. Germain *et al*., "Hot electrons and energy transport in metals at milliKelvin temperatures," Physical Review Letters **55** (4), 422-5 (1985).

[4] K. D. Irwin, G. C. Hilton, D. A. Wollman *et al*., "Thermal-response time of superconducting transition-edge sensors," Journal of Applied Physics **83** (8), 3978-85 (1998).

[5] Blas Cabrera (informal communication).

[6] R. F. Voss and J. Clarke, "1/f noise from systems in thermal equilibrium," Physical Review Letters **36** (1), 42-5 (1976).

[7] R. F. Voss and J. Clarke, "Flicker (l/f) noise: equilibrium temperature and resistance," Physical Review B (Solid State) **13** (2), 556-73 (1976).

[8] R. K. Pathria, *Statistical mechanics* (Butterworth-Heinemann, Oxford, 1996).

[9] E. H. Putley, Infrared Phys. **4**, 1 (1964).

[10] K. D. Irwin, "Phonon-Mediated Particle Detection Using Superconducting Tungsten Transition-Edge Sensors," Ph.D. Thesis, Stanford, 1995.

[11] S. H. Moseley, J. C. Mather, and D. McCammon, "Thermal detectors as X-ray spectrometers," Journal of Applied Physics **56** (5), 1257-62 (1984).

Chapter 4

MICROCALORIMETER THEORY

4.1 Introduction to microcalorimeter theory

In most previous analyses of bolometers and microcalorimeters [1-5], the devices considered were modeled as resistive thermometers, whose resistance is a function of temperature and is independent of the electrical current conducted through them. However, the resistance of most low temperature thermal sensors actually depends on both temperature and current. Therefore, the standard bolometer theory does not strictly apply to practical devices except in special limits when the current dependence can be neglected. Some current dependent effects were included in work by Mather [6] and Frank et al. [7]. Our model, presented here, includes all first-order current-dependent effects and provides a broader description of resistive microcalorimeters.

Our theory is a generalization of bolometer theory. The derivation is more straightforward than that presented in the bolometer theory papers of Jones [2], Mather [3,6], and Moseley et. al. [4] because we proceed more directly by linearizing the differential equations, rather than using complex impedance formalism.

Our model describes microcalorimeters that consist of an absorber strongly coupled to a thermometer as shown in Fig. 4.1. An energetic event in the absorber, such as the absorption of an x-ray photon, increases the temperature of the absorber and thermometer. The change in temperature causes a proportional change in electrical resistance of the thermometer. The microcalorimeter is weakly coupled to a cold bath so that the

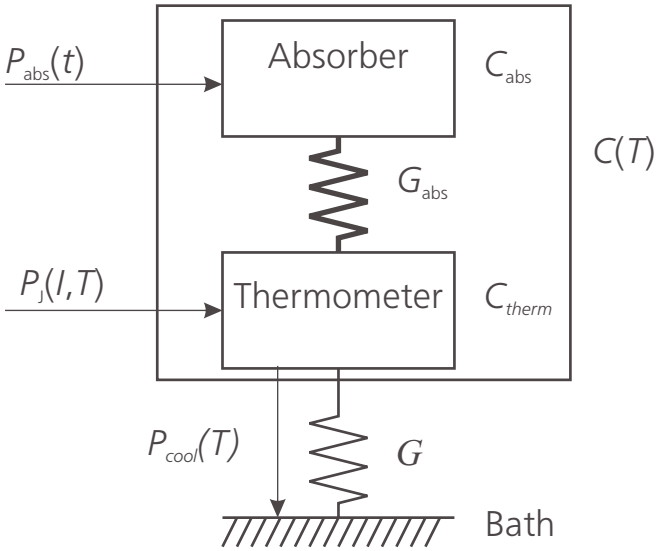

Figure 4.1. The thermal circuit of a simple microcalorimeter. The particle absorber is thermally connected to a thermometer by a strong thermal conductance G_{abs}. The absorber and thermometer are coupled to a cold bath by a weaker thermal coupling G. Ideally, the absorber and thermometer act like one thermal element with temperature T and heat capacity $C(T)$. Under operating conditions, Joule heating $P_J(I,T)$ in the thermometer elevates the equilibrium temperature of the thermometer and absorber above the bath temperature T_{bath}. Absorption of a particle in the absorber causes a heating power $P_{abs}(t)$ which temporarily increases the temperature T above equilibrium. This pulse in temperature is measured by the thermometer.

temperature returns to an equilibrium value after the event occurs. Thus, the response of a microcalorimeter to an event is typically a temperature pulse with a sharp rise and an exponential decay. The amplitude of the pulse is proportional to the energy of the event.

For simplicity, we assume that the thermometer and absorber thermally equilibrate very quickly and have practically the same temperature T. Then, the state of the microcalorimeter can be described by just two differential equations and two dynamic variables: the temperature of the microcalorimeter T, and the electric current through the thermometer I. Large calorimeters [8-12] and other calorimeters in which the absorber is weakly coupled to the thermometer will be described in Section 4.17. A thermal model for large calorimeters was developed by Proebst et al. [9], but they did not include current dependent effects.

In the following sections, we present our microcalorimeter model, and we describe conditions under which microcalorimeters operate in a stable, unstable, or oscillatory fashion. Electrothermal feedback, which is the interaction between the electrical and thermal circuits, and the effects of Joule heating in microcalorimeters are discussed. We derive new expressions for the pulse shape and theoretical limiting energy resolution. We include a discussion of the effects of amplifier noise and finite bandwidth on the energy resolution of these detectors. In Section 4.15, we provide an example of the application of the model to a transition-edge-sensor microcalorimeter.

4.2 Current-temperature model

4.2.1 The electrical circuit

We analyze microcalorimeters with thermometers connected to electronic bias circuits equivalent to the one shown in Fig. 4.2. This electrical circuit consists of a Thevenin equivalent voltage V_{th}, a Thevenin equivalent resistor R_{th}, an inductance L, and a resistive thermometer R. Changes in temperature of the thermometer result in changes in current or voltage at the thermometer. In this model, the thermometer is a resistor $R(I,T)$ whose resistance is a function of both the electric current I through it and its temperature T. Throughout this paper, we derive expressions for the current through the thermometer. However, the model also applies to the case when the voltage across the thermometer is measured.

The inductance L includes parasitic inductance in the circuit and the inductance of the input coil of a dc SQUID current amplifier, if one is used to measure the current though the thermometer. The electrical capacitance of the thermometer is neglected. This is a valid assumption when the RC time is much faster than the L/R time of the electrical circuit.

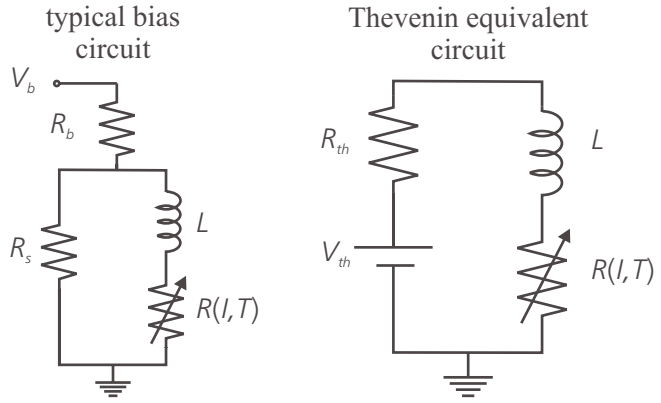

Figure 4.2. An example electrical bias circuit of a microcalorimeter and the Thevenin equivalent circuit. For the example circuit, the Thevenin equivalent voltage is $V_{th}=V_bR_s/(R_s+R_b)$ and the Thevenin equivalent resistance is $R_{th}=R_sR_b/(R_s+R_b)$. The thermometer's resistance R depends on current I and temperature T. The combination of the Thevenin equivalent voltage V_{th} and resistance R_{th} can apply either a current or a voltage bias to the thermometer depending on the value of R_{th}. The inductance in the circuit is L. Changes in temperature of the thermometer affect the current and voltage at the thermometer.

This circuit provides a current bias or voltage bias to the thermometer depending on whether the resistance R_{th} is large or small compared to the thermometer resistance $R(I,T)$. If the resistance R_{th} is large compared to $R(I,T)$, the bias circuit provides a current bias. If the resistance R_{th} is small compared to $R(I,T)$, the circuit biases the thermometer with a near constant voltage bias at low frequency. The thermometer is always current biased at frequencies greater than the R/L frequency of the circuit due the inductance L of the circuit.

The electrical circuit is described by the following equation:

$$L\frac{dI}{dt} = V_{th} - I(R_{th} + R(I,T)) \tag{4.1}$$

4.2.2 The thermal circuit

The thermal circuit is shown in Fig. 4.1. In our model, the thermometer is strongly coupled to the absorber and only weakly coupled to the bath at temperature T_{bath}. During operation,

the Joule heating power, $P_{\mathrm{abs}}(t)$, due to electric current in the thermometer, elevates the temperature of the thermometer and absorber above the bath temperature.

In this model, we assume that the thermometer and absorber can be regarded has having a common temperature, T, and a common heat capacity, $C(T)$. This is true if the thermometer and absorber are much better coupled to each other than they are to the cold bath and if the characteristic time of the electrical circuit is much slower than the time it takes for the thermometer and absorber to thermally equilibrate. In this case, the thermometer and absorber can be regarded as equilibrating instantaneously. Events in the absorber can be regarded as causing instantaneous changes in the temperature of the combined absorber-thermometer system. In this approximation, an event depositing an energy E into the absorber at time $t = t'$ can be described as an input power $P_{\mathrm{abs}}(t) = E\delta(t - t')$, where $\delta(t - t')$ is the Dirac delta function. The above assumptions are reasonable for many types of microcalorimeters. However, the model can be easily extended to the case in which energy slowly arrives into the microcalorimeter, as will be described in Section 4.17.

The thermal circuit is described by the following equation:

$$C(T)\frac{dT}{dt} = P_{\mathrm{J}}(I,T) - P_c(T,T_{\mathrm{bath}}) + P_{\mathrm{abs}}(t) \tag{4.2}$$

where $P_J(I,T) = I^2 R(I,T)$ is the Joule heating due to the electrical bias, and $P_{\mathrm{c}}(T,T_{\mathrm{bath}})$ is the power of the cooling into the cold bath.

We assume that the cooling of the microcalorimeter into the cold bath is described by a power law,

$$P_c(T, T_{\text{bath}}) = K(T^N - {T_{\text{bath}}}^N). \tag{4.3}$$

The constants K and N depend on the geometry of the detector and on the means by which the detector is thermally coupled to the cold bath.

4.3 Operating point

In order to function as part of a microcalorimeter, the thermometer must be operated near a stable equilibrium point. The equilibrium conditions are given by setting the derivatives and $P_{abs}(t)$ in equations (4.1) and (4.2) to zero. The current in equilibrium I_0 is given by

$$I_0(R_0, T_0) = \sqrt{\frac{K\left({T_0}^N - {T_{\text{bath}}}^N\right)}{R_0}}, \tag{4.4}$$

where R_0 and T_0 are the resistance and temperature of the thermometer at equilibrium. The thermometer is in electronic equilibrium when the voltage across the inductor is zero and the voltage across the thermometer is $V_0 = I_0 R_0$.

The temperature T and current I are also constrained by the relationship between current, temperature, and resistance $R(I,T)$:

$$R(I,T) = R_0. \tag{4.5}$$

This relationship is determined by the type and the design of the thermometer used in the microcalorimeter.

Both equations (4.4) and (4.5) are satisfied when a microcalorimeter is at equilibrium. For a particular value of R_0, the simultaneous solution of the two equations defines the operating

point (I_0, T_0). An illustration of the intersection of solutions to these equations for a transition-edge-sensor microcalorimeter is given in Section 4.15.

4.4 Linear approximation near equilibrium

In order to derive simple analytical expressions for stability, pulse shape, noise, and energy resolution, it is necessary to simplify the differential equations that describe the microcalorimeter. Near equilibrium, (I_0, T_0), equations (4.1) and (4.2) can be approximated by coupled linear partial differential equations and can be written in the following form:

$$\frac{d}{dt}\begin{pmatrix}\delta I\\ \delta T\end{pmatrix}=\begin{pmatrix}-\tau_{\mathrm{el}}^{-1} & -A\\ B & \tau_{\mathrm{eff}}^{-1}\end{pmatrix}\begin{pmatrix}\delta I\\ \delta T\end{pmatrix}, \tag{4.6}$$

where $\delta I = I - I_0$ and $\delta T = T - T_0$.

These linearized equations are obtained by rewriting (4.1) and (4.2) so that only the derivatives appear on the left side of the equations. Then, the Taylor expansion in I and T of the right sides of the equations is taken at the equilibrium point, (I_0, T_0). Terms of order higher than first order in δI and δT are neglected. The matrix contains four constants which represent coefficients of the first order terms in the Taylor expansion. We now define these coefficients and describe their physical meaning.

The electric time constant, τ_{el}, gives the characteristic response time of the electrical circuit. It is similar to the L/R time of the circuit, but it also includes effects due to the current dependence of the resistance of the thermometer. It measures how quickly the electrical circuit can respond to resistance changes of the thermometer.

$$\frac{1}{\tau_{\mathrm{el}}} = \frac{1}{L}(R_{\mathrm{th}} + R_0(1+\beta)) \tag{4.7}$$

The β parameter measures how sharply the resistance of the thermometer increases with increasing current at the operating point

$$\beta \equiv \frac{I_0}{R_0}\left[\frac{\partial R(I,T)}{\partial I}\right]_{\substack{I=I_0 \\ T=T_0}} \tag{4.8}$$

For semiconductor thermistors $\beta < 0$. For superconducting transition-edge-sensors $\beta > 0$.

The effective thermal time constant, τ_{eff}, gives the time scale of thermal changes in the microcalorimeter. The effective thermal time constant in turn depends on two other time constants,

$$\frac{1}{\tau_{\mathrm{eff}}} = \frac{1}{\tau_{\mathrm{J}}} - \frac{1}{\tau_{\mathrm{th}}}. \tag{4.9}$$

The thermal cooling time constant, τ_{th}, represents the characteristic time scale of the cooling into the cold bath in the absence of electrothermal feedback.

$$\frac{1}{\tau_{\mathrm{th}}} \equiv \left[\frac{\partial}{\partial T}\left(\frac{P_{\mathrm{c}}(T,T_{\mathrm{bath}})}{C(T)}\right)\right]_{\substack{I=I_0 \\ T=T_0}} = \frac{G_0}{C_0}\left(1 - \frac{\gamma}{N}\left(1 - \frac{{T_{\mathrm{bath}}}^N}{{T_0}^N}\right)\right), \tag{4.10}$$

where $G(T) = \partial P_{\mathrm{c}}(T,T_{bath})/\partial T = KNT^{N-1}$ is the thermal conductance between the thermometer and the cold bath, $G_0 = G(T_0)$, $C_0 = C(T_0)$, and γ is the sensitivity of the heat capacity to changes in temperature,

$$\gamma \equiv \frac{T_0}{C_0}\left[\frac{\partial C(I,T)}{\partial T}\right]_{\substack{I=I_0 \\ T=T_0}}. \tag{4.11}$$

Because the absorber usually has a much higher heat capacity than the thermometer, the value of γ is usually determined by the absorber material. For normal metals, $\gamma = 1$. For semiconductors at low temperature and for a superconductors well below the transition temperature, $\gamma = 3$. The γ parameter is negative for a superconductor in the phase transition between the superconducting and normal metal states.

The Joule heating time constant, τ_J, measures the time scale of changes in the Joule heating due to temperature perturbations.

$$\frac{1}{\tau_J} \equiv {I_0}^2\left[\frac{\partial}{\partial T}\left(\frac{R(I,T)}{C(T)}\right)\right]_{\substack{I=I_0 \\ T=T_0}} = \frac{{I_0}^2 R_0}{C_0 T_0}(\alpha' - \gamma) \tag{4.12}$$

The parameter α' describes how sharply the resistance increases with increasing temperature at the operating point,

$$\alpha' \equiv \frac{T_0}{R_0}\left[\frac{\partial R(I,T)}{\partial T}\right]_{\substack{I=I_0 \\ T=T_0}}. \tag{4.13}$$

The value of α' is a measure of the thermometer's sensitivity to temperature changes. Note that α' in equation (4.13) is not exactly the same as the commonly used term $\alpha = (T/R)dR/dT$. The constant α' is the *partial* derivative of the thermometer resistance with respect to temperature and is evaluated at the operating current I_0. In practice, α' is difficult to measure. The sensitivity of resistive thermometers are usually measured at low currents to avoid self-heating. Values of α measured at low current is typically used as a

benchmark for the sensitivity of these thermometers. The values of α derived from these measurements will typically be larger than α'. We discuss the implications of this in Section 4.14.

The cross terms, *A* and *B*, in equation (4.6) are defined as follows:

$$A \equiv \frac{I_0}{L}\left[\frac{\partial R(I,T)}{\partial T}\right]_{\substack{I=I_0 \\ T=T_0}} = \frac{I_0 R_0}{L T_0}\alpha', \tag{4.14}$$

$$B \equiv \frac{1}{C_0}\left[\frac{\partial P_J(I,T)}{\partial T}\right]_{\substack{I=I_0 \\ T=T_0}} = \frac{I_0 R_0}{C_0}(2+\beta). \tag{4.15}$$

The product of the cross terms describes the strength of the coupling between the electrical and thermal parts of the system. The electrothermal coupling time constant τ_{etc} is defined by

$$\frac{1}{{\tau_{\text{etc}}}^2} \equiv AB = \left(\frac{R_0}{L}\right)\left(\frac{{I_0}^2 R_0}{C_0 T_0}\right)(2+\beta)\alpha'. \tag{4.16}$$

As described in Section 4.6, the value of τ_{etc} pertains to the stability of the microcalorimeter.

4.5 Dynamical solution for small perturbations

The solution to equation (4.6) of the linear model in Section 4.4 describes the shape of a pulse resulting from the rapid absorption of a small amount of energy, *E*. An energetic event at time $t = 0$ causes a perturbation from equilibrium, which results in a exponential pulse of the form:

$$\begin{pmatrix} \delta I \\ \delta T \end{pmatrix} = \frac{\Delta T}{I_{\mathrm{d}} T_{\mathrm{r}} - I_{\mathrm{r}} T_{\mathrm{d}}} (I_{\mathrm{d}} \vec{x}_1 e^{-t/\tau_{\mathrm{r}}} - I_{\mathrm{r}} \vec{x}_2 e^{-t/\tau_{\mathrm{d}}}), \tag{4.17}$$

where $\Delta T = (T_0 / \gamma)(\sqrt{1 + 2\gamma E / C_0 T_0} - 1) \cong E / C_0$ is the temperature rise caused by the event. The approximation is valid in the limit that $dC(T)/dT << {C_0}^2 / 2E$.

The eigenvalues λ_1 and λ_2 of the matrix presented in equation (4.6) give the rise time τ_{r} and the decay time τ_{d} of the current pulse:

$$\lambda_1 = -\frac{1}{\tau_{\mathrm{r}}} = \frac{1}{2}\left(\frac{1}{\tau_{\mathrm{eff}}} - \frac{1}{\tau_{\mathrm{el}}}\right) - \sqrt{\left(\frac{1}{\tau_{\mathrm{eff}}} + \frac{1}{\tau_{\mathrm{el}}}\right)^2 - \frac{4}{{\tau_{\mathrm{etc}}}^2}} \tag{4.18}$$

$$\lambda_2 = -\frac{1}{\tau_{\mathrm{d}}} = \frac{1}{2}\left(\frac{1}{\tau_{\mathrm{eff}}} - \frac{1}{\tau_{\mathrm{el}}}\right) + \sqrt{\left(\frac{1}{\tau_{\mathrm{eff}}} + \frac{1}{\tau_{\mathrm{el}}}\right)^2 - \frac{4}{{\tau_{\mathrm{etc}}}^2}} \tag{4.19}$$

In Section 4.7, the rise and decay times will be discussed in more detail.

The eigenvectors give the directions of the rise and the decay of the pulse in (*I*,*T*) space. The eigenvectors of the matrix are

$$\vec{\mathrm{x}}_1 = \begin{pmatrix} I_{\mathrm{r}} \\ T_{\mathrm{r}} \end{pmatrix} = T_{\mathrm{x}} \begin{pmatrix} -B^{-1}({\tau_{\mathrm{r}}}^{-1} + {\tau_{\mathrm{eff}}}^{-1}) \\ 1 \end{pmatrix} \tag{4.20}$$

and

$$\vec{\mathrm{x}}_2 = \begin{pmatrix} I_{\mathrm{d}} \\ T_{\mathrm{d}} \end{pmatrix} = T_{\mathrm{x}} \begin{pmatrix} -B^{-1}({\tau_{\mathrm{d}}}^{-1} + {\tau_{\mathrm{eff}}}^{-1}) \\ 1 \end{pmatrix}, \tag{4.21}$$

where T_x is an arbitrary constant. The directions of the eigenvectors determine the shape of the pulse, but their absolute magnitudes have no significance. The ratio of the components of $\vec{x}_2$ gives the ratio of current δI to temperature δT in the tail of the pulse.

The current change as a function of time after an absorption event of energy E is

$$\delta I = \frac{\Delta T}{B}\left(1+\frac{\tau_r}{\tau_{eff}}\right)\left(1+\frac{\tau_d}{\tau_{eff}}\right)\frac{e^{-t/\tau_r}-e^{-t/\tau_d}}{\tau_d-\tau_r} \quad \text{for} \quad t \geq 0. \tag{4.22}$$

As an example, a pulse in a microcalorimeter which is described in Section 4.15 is shown in Fig. 4.3. In (I,T) space, the pulse has three legs and is roughly triangular. In the first leg, the temperature rises by ΔT, which increases the resistance $R(I,T)$ because $\alpha' > 0$ in this example. Since the temperature rise is instantaneous in this model, the current does not change during the first leg. In the second leg, the increased resistance causes a decrease in current. This is the rise of the current pulse. In the third and final leg, the temperature and resistance decrease so that the current increases. This is when the decay of the current pulse occurs. At the end of the final leg the microcalorimeter is returned to equilibrium.

4.6 Stability of the microcalorimeter

Researchers seek the highest possible energy resolution from microcalorimeters. High energy resolution requires that the thermometers have large $|\alpha'|$ and that they be operated at high power so that the signal dominates over amplifier noise. However, if the power and $|\alpha'|$ are too large, microcalorimeters may become unstable due to positive feedback and will not work at all. Therefore it is important to describe the conditions under which a microcalorimeter operates in a stable fashion.

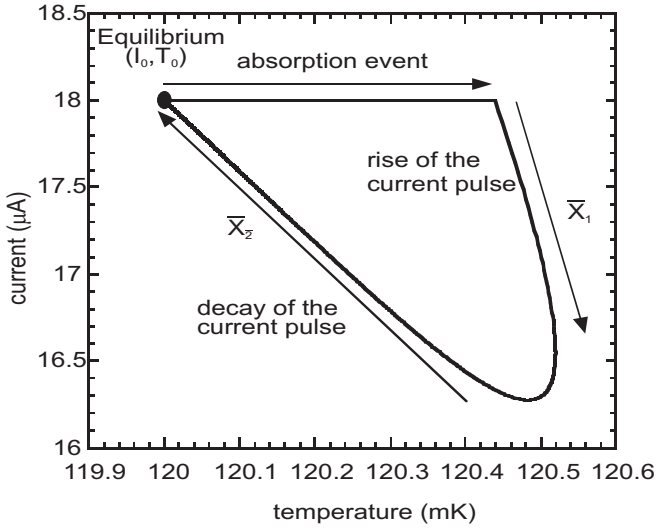

Figure 4.3. A pulse in current and temperature for a voltage-biased microcalorimeter with α', β, and γ greater than zero. The microcalorimeter's parameters are described in Section 4.15. Absorption of a particle elevates the temperature and resistance of the thermometer above equilibrium. During the rise of the current pulse, current decreases and temperature increases. The decay of the pulse returns the microcalorimeter to equilibrium.

The rise and decay times in equations (4.18) and (4.19) determine how a microcalorimeter responds to absorption events or other perturbations. A summary of the types of behavior expected based on the linear model of Section 4.4 is shown in Fig. 4.4.

If the rise and decay times are positive real numbers, the microcalorimeter is stable and not oscillatory, which is the usual way microcalorimeters are operated. This case is shown in Fig. 4.4a. The requirement that both the rise and decay time be positive numbers results in three constraints. Two of these constraints pertain to whether a microcalorimeter is stable or unstable. The third constraint pertains to whether a microcalorimeter responds to absorption events with exponentials or sinusoids. The two stability constraints are

$$\tau_{\mathrm{eff}}^{-1} < \tau_{\mathrm{el}}^{-1} \tag{4.23}$$

and

$$\tau_{\mathrm{eff}}{}^{-1}\tau_{\mathrm{el}}{}^{-1} < \tau_{\mathrm{etc}}{}^{-2}. \tag{4.24}$$

The constraint to avoid oscillatory behavior is

$$\left(\frac{1}{\tau_{\mathrm{eff}}}+\frac{1}{\tau_{\mathrm{el}}}\right)^2 > \frac{4}{\tau_{\mathrm{etc}}{}^2}. \tag{4.25}$$

Note that these inequalities can not be simplified by taking their reciprocals because the time constants τ_{el}, τ_{eff}, and $\tau_{\mathrm{etc}}{}^2$ can be either positive or negative. A microcalorimeter will have pulses that decay exponentially to equilibrium only if all three constraints are satisfied. Inequality (4.23) describes how fast the electrical circuit time τ_{el} must be to feedback against the effective thermal time τ_{eff} in order for the microcalorimeter to be stable. Inequality (4.24) describes how large the electrothermal coupling constant $\tau_{\mathrm{etc}}{}^2$ must be for the system to stable. Inequalities (4.23) and (4.24) are satisfied when the real parts of the of the eigenvalues λ_1 and λ_2 are negative. Inequality (4.25) places an upper limit on the coupling constant $\tau_{\mathrm{etc}}{}^2$. This inequality is satisfied when both eigenvalues λ_1 and λ_2 are real numbers. Notice that if τ_{eff} is negative and τ_{el} and $\tau_{\mathrm{etc}}{}^2$ are positive (as is the case for a transition-edge sensor based microcalorimeter operated at low power), a microcalorimeter is stable regardless of how fast or slow the electronics may be.

If the electrothermal coupling is very strong, then

$$\left(\frac{1}{\tau_{\mathrm{eff}}}+\frac{1}{\tau_{\mathrm{el}}}\right)^2 < \frac{4}{\tau_{\mathrm{etc}}{}^2} \tag{4.26}$$

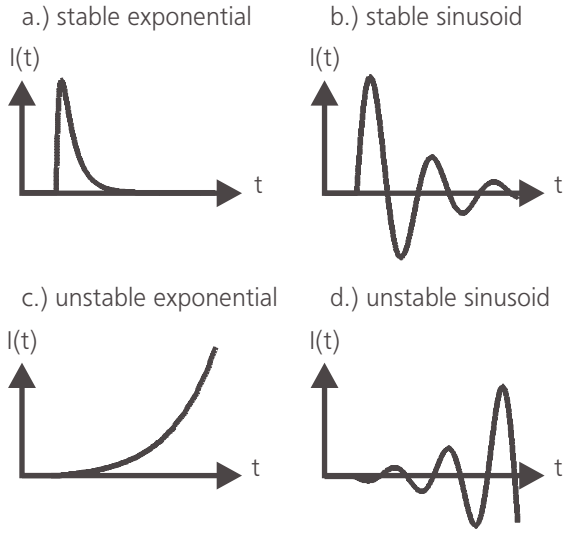

Figure 4.4. Microcalorimeters can respond to perturbations from equilibrium in a stable (a,b) or unstable (c,d) and a exponential (a,c) or oscillatory (b,d) fashion. The response of a particular microcalorimeter depends on the electrical and thermal circuits and on α', β, and γ of the calorimeter.

In this case, the eigenvalues λ_1 and λ_2 are not real numbers. Such a microcalorimeter is characterized by sinusoids rather than exponential pulses. Whether these sinusoids decay or increase with time depends on whether inequalities (4.23) and (4.24) are satisfied or not. Examples of the oscillating responses are shown in Fig. 4.4c and Fig. 4.4d.

If either inequality (4.23) or inequality (4.24) does not hold, then the equilibrium is unstable because one or both of the eigenvalues λ_1 and λ_2 have positive real parts. In this case, the system will diverge from equilibrium exponentially until the nonlinear terms in the differential equations become important. Examples of unstable responses are shown in Fig. 4.b and Fig. 4.d. The relationship between stability and feedback in the microcalorimeter is discussed in Section 4.8.

4.7 Electrothermal feedback in a microcalorimeter

We now describe electrothermal feedback in microcalorimeters in more detail. Electrothermal feedback is the interaction between the electrical and thermal circuits. Microcalorimeters with no significant electrothermal feedback, respond to absorption events with pulses that decay to equilibrium exponentially with the decay time τ_{th}. Electrothermal feedback can cause a microcalorimeter to oscillate or become unstable as described in the previous section. Electrothermal feedback can also lengthen or shorten pulses. Electrothermal feedback depends on both the signs and magnitudes of the time constants τ_{th}, τ_{J}, τ_{el}, and the coupling constant ${\tau_{\mathrm{etc}}}^2$.

If there is positive electrothermal feedback, pulses are lengthened so that the decay time is greater than τ_{th}. If there is negative electrothermal feedback, pulses are shortened compared to τ_{th}. In this section, we give examples in which the feedback is positive or negative.

In practical microcalorimeters, τ_{el} is often positive and the rise time is often much shorter than the decay time because the inductance L is small. In this case, the rise time of the pulse is approximately equal to τ_{el} and the decay time is

$$\tau_{\mathrm{d}} \cong \left(\frac{1}{\tau_{\mathrm{th}}} + \frac{\tau_{\mathrm{el}}}{{\tau_{\mathrm{etc}}}^2} - \frac{1}{\tau_{\mathrm{J}}} \right)^{-1}. \tag{4.27}$$

The first term on the right side of equation (4.27) `describes the decay time of the microcalorimeter in the limit that there is little electrothermal feedback. The second and third terms describe how the decay time τ_{d} is modified by electrothermal feedback. Specifically, the second term describes how the decay time is affected by coupling between

the electric and thermal circuits. The third term describes the influence of Joule heating on the decay time.

We substitute in for τ_{el}, τ_J, and $\tau_{etc}{}^2$ into equation (4.27) using equations (4.7), (4.12), and (4.16). We then obtain

$$\tau_d \cong \left(\frac{1}{\tau_{th}} + \frac{I_0{}^2 R_0}{C_0 T_0} \left(\left(\frac{R_0(2+\beta)\alpha'}{R_{th}+R_0(1+\beta)} \right) + (\gamma - \alpha') \right) \right)^{-1} \tag{4.28}$$

When the Joule power I^2R is zero, there is no pulse shortening or lengthening as can be seen in equation (4.28). The effect of electrothermal feedback on the decay time τ_d is increases with increasing Joule power. The sign of the feedback depends on α', β, γ, and whether the thermometer is voltage or current biased.

4.7.1 Current bias

A thermometer is current biased in the limit that $R_{th} \to \infty$. In this case the decay time is

$$\tau_d \cong \left(\frac{1}{\tau_{th}} + \frac{I_0{}^2 R_0}{C_0 T_0} (\gamma - \alpha') \right)^{-1} \tag{4.29}$$

Equation (4.29) indicates that pulses are lengthened if $\alpha > \gamma$ and shortened if $\alpha < \gamma$. Current bias produces negative electrothermal feedback in semiconductor thermometers because α' of these devices is negative and γ is positive. Current bias produces positive feedback in superconducting transition-edge-sensor thermometers with large positive α'.

4.7.2 Voltage bias

A thermometer is voltage biased in the limit that $R_{\mathrm{th}}, L \to 0$. In this case the decay time is

$$\tau_{\mathrm{d}} = \left(\frac{1}{\tau_{\mathrm{th}}} + \frac{{I_0}^2 R_0}{C_0 T_0} \left(\frac{\alpha'}{1+\beta} + \gamma \right) \right)^{-1} \tag{4.30}$$

Equation (4.30) indicates that pulses are shortened when $\beta \succ -1$ and

$$\alpha' > -\gamma(\beta + 1). \tag{4.31}$$

Transition-edge-sensor based microcalorimeters, for example, are subject to negative electrothermal feedback when they are voltage biased at high power because β is positive and α' is large and positive in these devices.

Inductance in the electronic circuit provides a current bias at high frequencies. Therefore, if the inductance L is not small, inductance effects tend to oppose the effects of a voltage bias. In that case, equation (4.19) must be used to calculate the decay time.

4.7.3 Instability and positive feedback

The effects of electrothermal feedback on microcalorimeter stability can be summed up as follows: When operated at high power, current-biased thermometers with large positive values of α' are not stable due to positive feedback. Voltage biased thermometers with large positive values of α' are also unstable at high power because inductance in the circuit provides a current bias and positive feedback at high frequencies. When operated at high power, voltage-biased thermometers with large negative values of α' and $\beta > -1$ are also unstable due to positive feedback. However, electrothermal feedback does not cause current-biased thermometers with negative values of α' to become unstable at high power.

4.8 Joule heating

As previously stated, the τ_J term represents the effects of Joule heating in the microcalorimeter. It is positive when α' is positive. When τ_J is positive Joule heating tends to push the system away from equilibrium (unless it is counteracted by other components of the electrothermal feedback as discussed below). A positive perturbation in the temperature of the microcalorimeter away from the equilibrium temperature causes increased Joule heating in the thermometer which in turn may drive the microcalorimeter's temperature still farther above equilibrium. Therefore, Joule heating is a potential source of instability in thermometers with positive α'. Three different modes of stable electrothermal feedback are distinguished from each other by how large the Joule heating term is in comparison to the thermal cooling term τ_{th}.

4.8.1 Weak Joule heating

The effects of Joule heating are weak when

$$\left|\tau_J\right| > \tau_{th}. \tag{4.32}$$

In this mode, cooling into the cold bath dominates over Joule heating. If τ_{el} is positive, a microcalorimeter with weak Joule heating is stable whether it is voltage biased or current biased and whether α' is positive or negative. In this mode, the effective thermal time τ_{eff} is negative. The effective thermal time τ_{eff} and decay time τ_d are significantly lengthened if τ_J nearly equals τ_{th}. Weak Joule heating occurs when α' is small or when bias power $P_{abs}(t)$ is relatively low.

4.8.2 Strong Joule heating

Strong Joule heating occurs when

$$\left|\tau_{\mathrm{J}}\right| < \tau_{\mathrm{th}} \tag{4.33}$$

In this mode, the Joule heating is stronger than the cooling into the cold bath. In thermometers with negative α', such as semiconductor based thermometers, the Joule heating time τ_{J} is negative. In those devices, Joule heating shortens the effective thermal time τ_{eff} and the decay time τ_{d}.

In thermometers with positive α', such as transition-edge sensors, Joule heating is a source of positive feedback. However, the tendency of the Joule heating to make the microcalorimeter unstable can be counteracted if the thermal circuit is strongly coupled to a fast electrical circuit which provides negative feedback.

A microcalorimeter with strong Joule heating and positive α' is stable under the following conditions:

$$\tau_{\mathrm{eff}}\tau_{\mathrm{el}} > {\tau_{\mathrm{etc}}}^{2}, \quad \text{and} \tag{4.34}$$

$$\tau_{\mathrm{eff}} > \tau_{\mathrm{el}}. \tag{4.35}$$

Note that we were able to rewrite (4.23) and (4.24) this way here because we have assumed that τ_{eff}, τ_{elec}, and τ_{etc} are all positive.

Inequality (4.35) is satisfied when

$$\frac{{I_0}^2 R_0}{C_0 T_0}(\alpha' - \gamma) < {\tau_{\mathrm{el}}}^{-1}, \tag{4.36}$$

which limits how large α' and the Joule power may be.

In the limit that $\alpha' >> -\gamma$, $\alpha' >> N$, and ${T_0}^N >> {T_{\text{bath}}}^N$, then (4.34) is satisfied when $R_{\text{th}} < R_0$. This means that if the Joule heating is strong and α' is positive, a microcalorimeter must be approximately voltage biased to be stable. Because α' is a large positive number for TES thermometers, TES microcalorimeters must be voltage biased to operate at high power.

4.8.3 Very strong Joule heating

The Joule heating is very strong if

$$\left|\tau_{\text{J}}\right| << \tau_{\text{th}}\,. \tag{4.37}$$

This is a special case of the strong Joule heating described above. The stability conditions (4.34) and (4.35) apply to this case as well.

In this mode, cooling into the substrate can be neglected. Then, $\tau_{\text{eff}} = \tau_{\text{J}}$, and the power from an absorption event $P_{abs}(t)$ is nearly entirely canceled by a decrease in Joule heating [1]. By conservation of energy,

$$\int (P_{\text{abs}}(t) + P_{\text{J}}(I,T) - P_{\text{J}}(I_0,T_0))\,dt \cong 0\,, \tag{4.38}$$

where I and T are both functions of time as given by equation (4.17). The above result is not restricted to the linear model; it applies even when nonlinear terms are included.

4.9 Self calibration

Microcalorimeters are self calibrating. The relationship between energy and pulse amplitude in the linear model is given by equation (4.22). The energy of an absorption event can be obtained directly from the measurement of a current pulse without need for

independent calibration if the parameters in equation (4.22) are known from theory or direct measurement.

In general, the parameters in equation (4.22) must be known precisely in order to calculate the energy of an event. However, if the rise time τ_r and the decay time τ_d are much less then the thermal cooling time τ_{th} due to very strong Joule heating, then equation (4.38) implies that the absorption of energy E causes a decrease in Joule heating approximately equal to E. Under these conditions, the energy of an event in a voltage-biased microcalorimeter with positive α' and negligible inductance L is

$$E \cong -V_0 \int_0^\infty \delta I \, dt \, . \tag{4.39}$$

Similarly, when thermometers with negative α' are current biased at high power so that there is strong Joule heating, the energy of an event is

$$E \cong -I_0 \int_0^\infty \delta V \, dt \tag{4.40}$$

where $\delta V = V - V_0$ is the pulse in voltage. In these cases, the energy of an event can be easily obtained from the integral of a current or voltage measurement, without need of detailed knowledge of the parameters that describe the microcalorimeter [1].

4.10 Noise in the linear model

The response of a microcalorimeter varies from measurement to measurement due to thermal noise. We model the noise in microcalorimeters by adding noise terms to the differential equations. A voltage noise term V_{VN} is added to the electrical equation to account for voltage fluctuations due to Johnson noise and other sources of electronic noise

in the thermometer. In this section, we neglect other sources of electronic noise such as Johnson noise $V_{Rth}(t)$ associated with the series resistance R_{th} in order to simplify the calculation. Such electronic noise is described in Section 4.13. Note that with proper choice of resistors, it is often possible to design a circuit such that noise from the microcalorimeter dominates over any Johnson noise from other circuit elements.

Fluctuations in the power dissipated in the thermometer due to voltage noise $V_{\text{VN}}(t)$ in the thermometer are modeled by adding a voltage noise power term $P_{\text{VN}}(t)$ to the thermal equation. The voltage noise power term $P_{\text{VN}}(t)$ represents how the power dissipated in the thermometer varies with the fluctuation in current and voltage at the thermometer. $P_{\text{VN}} = IV_{\text{VN}} = (I_0 + \delta I)V_{\text{VN}}$. The voltage noise power term is approximated to first order by $P_{\text{VN}} \cong I_0 V_{\text{VN}}$. This approximation is valid when I_0 is much larger than the typical fluctuations in the current δI. Energy fluctuations due to phonon noise are included by adding a phonon noise power term $P_{\text{PN}}(t)$ to the thermal equation.

At this point, it is valuable to point out that previous microcalorimeter papers can cause some confusion about what is actually measured by microcalorimeters. Previous authors formulated their descriptions of microcalorimeters in a way that appears to indicate that thermal noise represents fluctuations in the temperature of a microcalorimeter [1,3,13], which is not true. When a microcalorimeter is at thermodynamic equilibrium, it is the internal energy of the microcalorimeter that fluctuates, not the temperature itself. The confusion is cleared up by noting that they implicitly used the notion of an *effective* temperature in describing the internal energy in calorimeters. As described in Section 3.4. The distinction between temperature and effective temperature is that the effective temperature is a function of the internal energy of a specific calorimeter, but the actual temperature is a thermodynamic quantity that depends on an ensemble average of a large number of identical macroscopic systems. For the remainder of this thesis, variable T

represents effective temperature of a specific calorimeter. The resistance $R(I,T)$ of a particular thermometer depends on the effective temperature of that thermometer, not on an ensemble average.

The differential equations with noise terms are

$$L\frac{dI}{dt} = V_{\text{th}} - I(R_{\text{th}} + R(I,T)) - V_{\text{VN}}(t) \tag{4.41}$$

and

$$C(T)\frac{dT}{dt} = P_{\text{J}}(I,T) - P_c(T,T_{\text{bath}}) + P_{\text{abs}}(t) + P_{\text{VN}}(t) + P_{\text{PN}}(t)\,. \tag{4.42}$$

The electrical circuit with a voltage noise source $V_{\text{VN}}(t)$ included is illustrated in Fig. 4.5. The figure also includes a voltage noise source $V_{Rth}(t)$ which we neglect in this section but will describe in Section 4.13. The thermal circuit with phonon noise and voltage noise source terms is illustrated in Fig. 4.6.

The linearized equations for small perturbations from equilibrium are,

$$\frac{d}{dt}\begin{pmatrix}\delta I\\ \delta T\end{pmatrix} = \begin{pmatrix}-\tau_{\text{el}}^{-1} & -A\\ B & \tau_{\text{eff}}^{-1}\end{pmatrix}\begin{pmatrix}\delta I\\ \delta T\end{pmatrix} + \begin{pmatrix}-V_{\text{VN}}(t)/L\\ (P_{PN}(t) + I_0 V_{\text{VN}}(t))/C_0\end{pmatrix}. \tag{4.43}$$

The Fourier transform of equation (4.43) gives,

$$2\pi i f\,\frac{d}{dt}\begin{pmatrix}\delta I\\ \delta T\end{pmatrix} = \begin{pmatrix}-\tau_{\text{el}}^{-1} & -A\\ B & \tau_{\text{eff}}^{-1}\end{pmatrix}\begin{pmatrix}\delta I\\ \delta T\end{pmatrix} + \begin{pmatrix}-V_{\text{VN}}(f)/L\\ (P_{PN}(f) + I_0 V_{\text{VN}}(f))/C_0\end{pmatrix}. \tag{4.44}$$

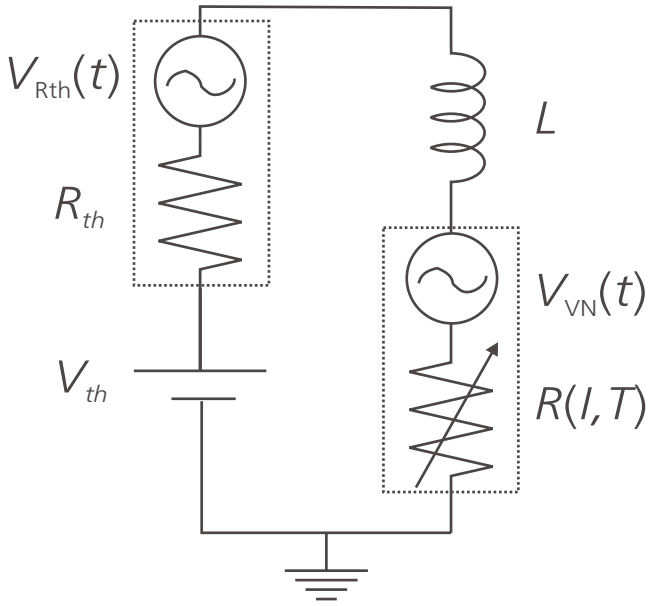

Figure 4.5. The electrical circuit with voltage noise source $V_{\mathrm{VN}}(t)$ due to voltage fluctuations in the thermometer and voltage noise source $V_{\mathrm{Rth}}(t)$ due to voltage noise from shunt or bias resistors. The noise due to $V_{\mathrm{VN}}(t)$ is described in Section 4.10. The noise due to $V_{\mathrm{Rth}}(t)$ is described in Section 4.13.

We solve for δI_{f} and δT_{f}, which are the Fourier transforms of the displacements of the current and temperature from equilibrium. We find $\left|\delta I_f\right|$ and $\left|\delta T_{\mathrm{f}}\right|$ by multiplying by the complex conjugate. Note that the voltage noise and the phonon noise are assumed to be uncorrelated to each other, so they add in quadrature. This assumption is valid if the resistance and temperature remain close to their equilibrium values R_0 and T_0. The current noise obtained from equation (4.44) is given by

$$\left|\delta I_{\mathrm{f}}\right|^2 = \left|D(f)\right|^2 \left(\left((2\pi f)^2 + {\tau_{\mathrm{VN}}}^{-2} \right) \frac{\left|V_{\mathrm{VN}}(f)\right|^2}{L^2} + A^2 \frac{\left|P_{\mathrm{PN}}(f)\right|^2}{{C_0}^2} \right), \qquad (4.45)$$

where

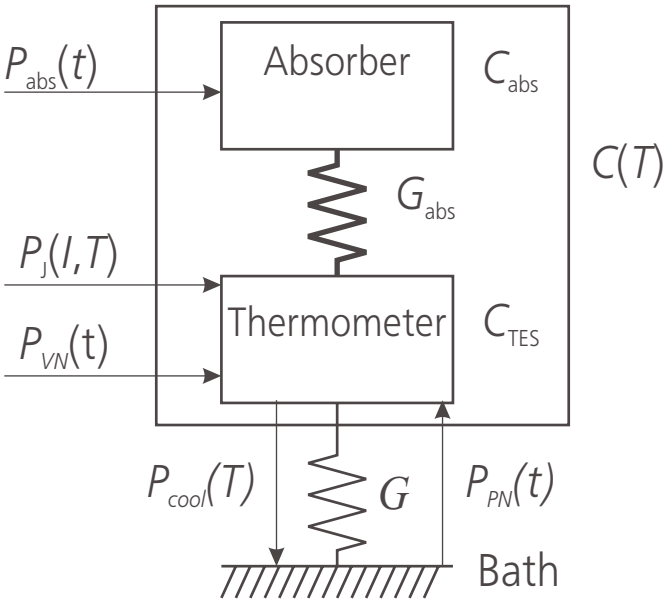

Figure 4.6. The thermal circuit with a phonon noise power term $P_{PN}(t)$ and a voltage noise power term $P_{VN}(t)$ included. The phonon noise is caused by the thermal coupling of the thermometer to the bath. The voltage noise power is caused by voltage fluctuations in the thermometer.

$$D(f)^{-1} \equiv \det\begin{pmatrix} -\tau_{el}^{-1} + i2\pi f & A \\ -B & -\tau_{eff}^{-1} + i2\pi f \end{pmatrix} \tag{4.46}$$

and

$$\tau_{VN}^{-1} \equiv \left| \tau_{eff}^{-1} - \frac{AI_0L}{C_0} \right|. \tag{4.47}$$

The first term on the right side of equation (4.47) is derived from the voltage noise term V_{VN} in equation (4.41). The second term is obtained from the voltage noise power P_{VN} in equation (4.42). If the effects of voltage noise in the electrical circuit opposes the effects of voltage noise power in the thermal circuit then these two terms have opposite signs and there is a reduction in the voltage noise in the thermometer [3].

The spectral density for positive frequencies of the phonon noise [1] is given by

$$\left|P_{\mathrm{PN}}(f)\right|^2 = 2k_{\mathrm{B}}G_0({T_0}^2 + {T_{\mathrm{bath}}}^2)\,. \tag{4.48}$$

The first term in equation (4.48) is due to phonons diffusing from the microcalorimeter into the cold bath. The second term represents the phonons that diffuse into the microcalorimeter from the bath. If the voltage noise is dominated by the Johnson noise of the thermometer, then the spectral density for positive frequencies of the voltage noise is $\left|V_{\mathrm{VN}}\right| = 4k_{\mathrm{B}}T_0R_0$.

The theoretical current noise in a microcalorimeter due to Johnson noise and phonon noise is calculated using equation (4.45). A plot of current noise as a function of frequency f is shown in Fig. 4.7. The noise is plotted for an example microcalorimeter which is described in Section 4.15. In the figure, the Johnson noise begins to increase near frequency $1/(2\pi\tau_{\mathrm{VN}})$. The Johnson noise and the phonon noise roll off at frequencies greater than $1/(2\pi\tau_{\mathrm{VN}})$. The Johnson noise and phonon noise roll off faster still at frequencies greater than $1/(2\pi\tau_{\mathrm{el}})$. Amplifier noise and noise due to R_{th}, which are also shown in the figure, are discussed below in Section 4.13.

4.11 Optimal energy resolution

The noise equivalent power (NEP) is defined such that the ratio of signal power $P_{\mathrm{abs}}(f)$ to noise equivalent power $\left|\mathrm{NEP}(f)\right|$ equals the ratio of signal to noise. Using this definition, we can now calculate the noise equivalent power for noise sources within a microcalorimeter:

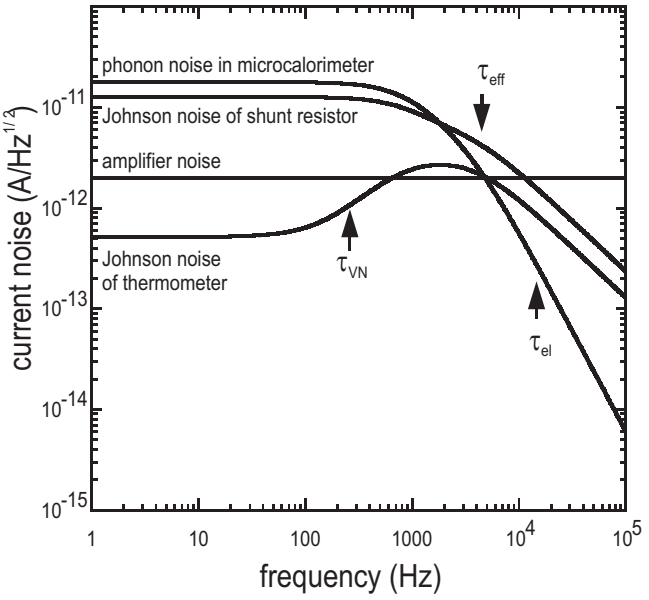

Figure 4.7. A theoretical calculation of the current noise due to phonon noise, Johnson noise, and amplifier noise for the example microcalorimeter described in Section 4.15. At low frequency, the Johnson noise is reduced due to partial cancellation of the Johnson voltage in the electrical circuit by the Johnson noise power in the thermal circuit.

$$\left|\mathrm{NEP}(f)\right|^2 = \frac{{C_0}^2 \left|\delta I_\mathrm{f}\right|^2}{A^2 \left|D(f)\right|^2}, \tag{4.49}$$

where δI_f includes the measured current fluctuations from all noise sources within the microcalorimeter. In the ideal case, the voltage noise and the phonon noise dominate over other forms of noise. Then, δI_f is given by equation (4.45) and

$$\left|\mathrm{NEP}(f)\right|^2 = \left|\mathrm{NEP}_\mathrm{VN}(f)\right|^2 + \left|\mathrm{NEP}_\mathrm{PN}(f)\right|^2 . \tag{4.50}$$

In the following discussion, we shall assume voltage noise and thermal noise do not significantly vary during a response to an energetic event in the microcalorimeter. This is valid for the case of small perturbations in which temperature and resistance vary by a small

amount in response to an energetic event. Therefore, we keep the zero-order noise terms and neglect the noise terms of higher order.

If the voltage noise is white, as is the case for Johnson noise in a resistor or independent phase slips in a superconductor [14], then the noise equivalent power can be written as

$$\left|\mathrm{NEP}_{\mathrm{VN}}(f)\right|^2 = \frac{{C_0}^2\left((2\pi f)^{-2} + {\tau_{\mathrm{VN}}}^{-2}\right)}{A^2 L^2}\left|V_{\mathrm{VN}}(f)\right|^2 \tag{4.51}$$

$$= \left|\mathrm{NEP}_{\mathrm{VN}}(0)\right|^2\left(1 + (2\pi f)^2\,{\tau_{\mathrm{VN}}}^{-2}\right) \tag{4.52}$$

where

$$\left|\mathrm{NEP}_{\mathrm{VN}}(0)\right| = \frac{C_0 T_0}{I_0 R_0}\frac{1}{\left|\tau_{\mathrm{VN}}\alpha'\right|}\left|V_{\mathrm{VN}}(0)\right|^2 . \tag{4.53}$$

The voltage noise equivalent power tends to infinity as the applied voltage $V_0 = I_0 R_0$ goes to zero because the voltage noise dominates over the signal at low power.

If the voltage noise is dominated by Johnson noise in the thermometer, then the voltage noise at zero frequency is given by

$$\left|V_{\mathrm{VN}}(0)\right| = \sqrt{4k_{\mathrm{B}}T_0 R_0} . \tag{4.54}$$

If the voltage is dominated by independent phase slips of magnitude $\Delta\varphi$, the voltage noise at zero frequency is given by

$$\left|V_{\mathrm{VN}}(0)\right| = \sqrt{\frac{\phi_0 \Delta\varphi}{\pi} V_0} \tag{4.55}$$

where ϕ_0 is the flux quantum. Sources of voltage noise, such as voltage noise due to phase slips or vortex motion in a transition-edge sensor, may cause the voltage noise to be significantly larger than the Johnson noise value [14].

The phonon noise equivalent power is independent of frequency, since the phonon noise varies with frequency just as the signal does,

$$\left|\mathrm{NEP}_{\mathrm{PN}}(f)\right|^2 = \left|P_{\mathrm{PN}}(f)\right|^2 = 2k_{\mathrm{B}}G_0({T_0}^2 + {T_{\mathrm{bath}}}^2). \tag{4.56}$$

The noise equivalent powers of the example microcalorimeter described in Section 4.15 are plotted in Fig. 4.8. The figure shows that the Johnson noise equivalent power increases at frequencies greater than $1/2\pi\tau_{\mathrm{VN}}$. Amplifier noise, which is also plotted in the figure, will be discussed in Section 4.13.

The energy resolution of a microcalorimeter, when optimally filtered [15], is given by an integral of the noise equivalent power [4]

$$\Delta E_{\mathrm{FWHM}} = 2.35\left(\int_0^\infty \frac{4\,df}{\left|\mathrm{NEP}(f)\right|^2}\right)^{-1/2}. \tag{4.57}$$

Upon integrating, we find that the energy resolution is given by

$$\Delta E_{\mathrm{FWHM}} = 2.35\sqrt{\left|\tau_{\mathrm{VN}}\right\|\mathrm{NEP}_{\mathrm{VN}}(0)\left\|\mathrm{NEP}(0)\right|}. \tag{4.58}$$

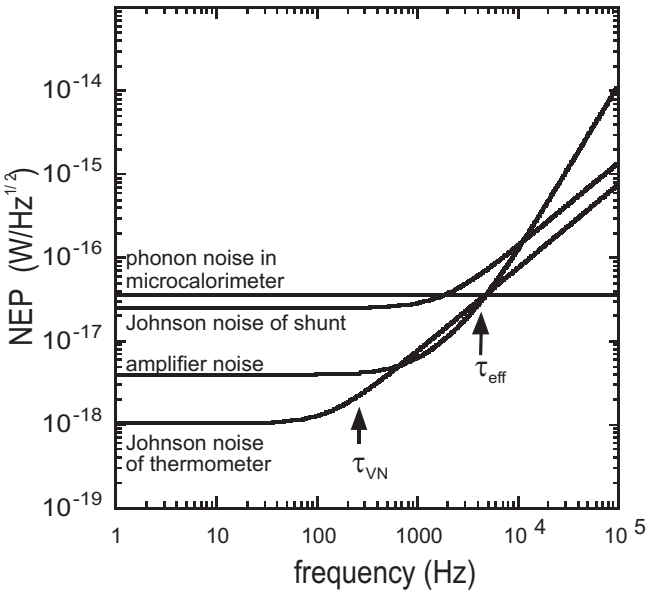

Figure 4.8. A theoretical calculation of noise equivalent power (NEP) due to phonon noise, Johnson noise, and amplifier noise for the example microcalorimeter described in Section 4.15.

This is the energy resolution of a microcalorimeter whose dominant sources of noise are phonon noise and white voltage noise in the microcalorimeter. It is the optimal energy resolution obtainable from a microcalorimeter with a resistive thermometer. In Section 4.13, we present a more general result which includes amplifier noise and noise due to R_{th}, which are often significant in real microcalorimeters. In Section 4.14, we compare the result in equation (4.58) to results obtained by other authors.

4.12 Bandwidth and energy resolution

In Section 4.11, we derived the resolution of the microcalorimeter in the limit that the amplifier has infinite bandwidth. We now consider a microcalorimeter in which the measurement of the current through the thermometer are limited to a bandwidth $0 < f < f_{\mathrm{max}}$ by the gain of an amplifier or by a limited digital sampling rate. As before,

we assume a microcalorimeter in which phonon noise and white voltage noise are the dominate sources of noise. In this case, we find

$$\Delta E_{\mathrm{FWHM}} \cong 2.35\left(\int_0^{f_{\max}} \frac{4\,df}{\left|\mathrm{NEP}(f)\right|^2}\right)^{-1/2} = \sqrt{\frac{\pi/2}{\arctan(f_{\max}/f_0)}}\,\Delta E_{\infty}, \qquad (4.59)$$

where

$$2\pi f_0 = \frac{1}{\tau_{\mathrm{VN}}}\sqrt{1+\frac{\left|\mathrm{NEP}_{\mathrm{PN}}(0)\right|^2}{\left|\mathrm{NEP}_{\mathrm{VN}}(0)\right|^2}}\,, \qquad (4.60)$$

and ΔE_{∞} is the resolution for infinite bandwidth given by (4.58). The frequency f_0 is the lowest frequency such that $\left|\mathrm{NEP(f)}\right|^2 \geq 2\left|\mathrm{NEP(0)}\right|^2$.

The bandwidth of the readout electronics $f_{\max}$ must be as large as f_0 or the measured energy resolution of the microcalorimeter will not be within a factor $\sqrt{2}$ of the optimal energy resolution (which is also called the theoretical limiting resolution). This gives an estimate of how fast electronic amplifiers must be in order for the microcalorimeter to operate near the optimal resolution.

4.13 Amplifier noise and other noise

In our model, the effects of various forms of noise are included by adding terms to the electrical circuit equation (4.41), the thermal circuit equation (4.42), and the linearized equations for small perturbations (4.43). We have included phonon noise and white voltage noise in the microcalorimeter. Other sources of noise such as the Johnson noise in the

electrical circuit, amplifier noise, infrared photon noise, microphonics, and radio-frequency interference can also be included, as can forms of voltage noise that are not white, such as noise due to random magnetic flux motion in transition-edge sensors. Note that the optimal filter formalism is based on the assumption that noise appearing at any one frequency is uncorrelated to noise at other frequencies. Therefore, we only describe such uncorrelated noise in this chapter.

If the electrical current δI through the thermometer is measured, equation (4.49) relates the NEP of all noise sources to the current fluctuations δI_f. However, if the voltage drop across the thermometer is measured instead of the current, then equation (4.49) is only valid for noise sources internal to the microcalorimeter, such as phonon noise $P_{\mathrm{PN}}(t)$ and voltage noise in the thermometer $V_{\mathrm{VN}}(t)$. For voltage measurements, the NEP of noise sources external to the microcalorimeter, such as noise $V_{\mathrm{Rth}}(t)$ due to shunt or bias resistors, must be calculated using a different expression described at the end of this section.

The effects of amplifier noise can be included into our model analytically. The amplifier noise is expressed as current noise $\left|I_{\mathrm{amp}}(f)\right|$. Assuming the current through the thermometer is measured, the noise equivalent power of the amplifier noise is

$$\left|NEP_{\mathrm{amp}}(f)\right|^2 = \frac{{C_0}^2}{A^2\left|D(f)\right|^2}\left|I_{\mathrm{amp}}(f)\right|^2. \tag{4.61}$$

In Section 4.10, we neglected any electrical noise sources outside the thermometer to simplify the calculation. However, this form of noise can be easily included by adding another voltage noise term $V_{\mathrm{Rth}}(t)$ to equation (4.41). A circuit with electronic noise in the thermometer $V_{\mathrm{VN}}(t)$ and electronic noise outside the thermometer $V_{\mathrm{Rth}}(t)$ is shown

Fig. 4.5. The voltage noise $V_{\mathrm{Rth}}(t)$ does not directly affect the power dissipated in the microcalorimeter as $V_{\mathrm{VN}}(t)$ does because $V_{\mathrm{Rth}}(t)$ does not directly affect the voltage drop across the thermometer. The voltage noise $V_{\mathrm{Rth}}(t)$ only affects the power dissipated in the thermometer by affecting the current flow through the circuit. Therefore, no additional power term is added to equation (4.42).

Bias or shunt resistors in the electrical circuit are represented by the Thevenin equivalent resistance R_{th}. These resistors are a source of Johnson noise in the electrical circuit. This Johnson noise is represented by the voltage noise $V_{\mathrm{Rth}}(t)$. The voltage noise $V_{\mathrm{Rth}}(t)$ is in series with R_{th}. Therefore, the voltage noise term $V_{\mathrm{Rth}}(t)$ is added to the right side of equation (4.41) to include this noise into the model. We solve for the current noise by using the methods of Section 4.10 but with $V_{\mathrm{Rth}}(t)$ included. We find that the additional current noise in the electrical circuit due to the Johnson noise $V_{\mathrm{Rth}}(t)$ is

$$\left|\delta I_{\mathrm{f}}\right|^2 = \left|D(f)\right|^2 \left((2\pi f)^{-2} + {\tau_{\mathrm{eff}}}^{-2}\right) \frac{\left|V_{\mathrm{Rth}}(f)\right|^2}{L^2}, \tag{4.62}$$

where $V_{\mathrm{Rth}}(f)$ is the Fourier transform of $V_{\mathrm{Rth}}(t)$. If the current through the thermometer is measured, the noise equivalent power due to $V_{\mathrm{Rth}}(f)$ is

$$\left|\mathrm{NEP}_{\mathrm{Rth}}(f)\right|^2 = \left|\mathrm{NEP}_{\mathrm{Rth}}(0)\right|^2 \left(1 + (2\pi f)^2 {\tau_{\mathrm{eff}}}^{-2}\right) \tag{4.63}$$

where

$$\left|\mathrm{NEP}_{\mathrm{Rth}}(0)\right| = \frac{C_0 T_0}{I_0 R_0} \frac{1}{\left|\tau_{\mathrm{eff}} \alpha'\right|} \left|V_{\mathrm{Rth}}(0)\right|. \tag{4.64}$$

In the presence of amplifier noise and noise associated with R_{th}, the total noise equivalent power in the microcalorimeter is

$$\left|\mathrm{NEP}(f)\right|^2 = \left|\mathrm{NEP}_{\mathrm{VN}}(f)\right|^2 + \left|\mathrm{NEP}_{\mathrm{PN}}(f)\right|^2 + \left|\mathrm{NEP}_{\mathrm{amp}}(f)\right|^2 + \left|\mathrm{NEP}_{\mathrm{Rth}}(f)\right|^2. \quad (4.65)$$

As before, the voltage noise is thermometer $V_{\mathrm{VN}}(t)$ is assumed to be white. We also assume that the power of amplifier noise is independent of frequency, $\left|I_{\mathrm{amp}}(f)\right| = \left|I_{\mathrm{amp}}(0)\right|$. The noise equivalent power is given by

$$\left|\mathrm{NEP}(f)\right|^2 = a_2(2\pi f)^4 + a_1(2\pi f)^2 + a_0(2\pi f) \quad (4.66)$$

where

$$a_0 = \left|\mathrm{NEP}(0)\right|^2$$

$$a_1 = (2{\tau_{\mathrm{etc}}}^{-2} + {\tau_{\mathrm{el}}}^{-2} + {\tau_{\mathrm{eff}}}^{-2})^{-1}\left|\mathrm{NEP}_{\mathrm{amp}}(0)\right|^2 + \left|\tau_{\mathrm{VN}}\right|^2\left|\mathrm{NEP}_{\mathrm{VN}}(0)\right|^2$$

$$+ \left|\tau_{\mathrm{eff}}\right|^2\left|\mathrm{NEP}_{\mathrm{Rth}}(0)\right|^2$$

$$a_2 = ({\tau_{\mathrm{etc}}}^{-2} - {\tau_{\mathrm{el}}}^{-1}{\tau_{\mathrm{eff}}}^{-1})^{-2}\left|\mathrm{NEP}_{\mathrm{amp}}(0)\right|^2. \quad (4.67)$$

Using equation (4.57), we obtain the energy resolution

$$\Delta E_{\mathrm{FWHM}} = 2.35\left(a_1 a_0\left(1 + \frac{\sqrt{a_2 a_0}}{a_1}\right)\right)^{1/4}. \quad (4.68)$$

Equation (4.68) gives the energy resolution of a microcalorimeter including amplifier noise and noise due to bias or shunt resistors. This resolution can be significantly poorer than the resolution given by equation (4.58).

To obtain the optimal energy resolution, given by equation (4.58), the current fluctuations due to amplifier noise $I_{\text{amp}}(f)$ must be small in comparison to the current fluctuations due to the combined Johnson and phonon noise up to the frequency f_0, which was defined in equation (4.60). In terms of the noise equivalent power, this constraint is

$$\left|\text{NEP}_{\text{amp}}(f)\right|^2 << \left|\text{NEP}_{\text{VN}}(f)\right|^2 + \left|\text{NEP}_{\text{PN}}(f)\right|^2, \quad \text{for} \quad f < f_0 . \tag{4.69}$$

For white amplifier noise this constraint is met under the following condition:

$$\left|I_{\text{amp}}\right|^2 << 2\left(\left|\text{NEP}_{\text{VN}}(0)\right|^2 + \left|\text{NEP}_{\text{PN}}(0)\right|^2\right)\frac{A^2 D(f_0)}{{C_0}^2} . \tag{4.70}$$

White amplifier noise in the example microcalorimeter of Section 4.15 is illustrated in Fig. 4.7. The noise equivalent power of the example amplifier noise increases at frequencies greater than $1/(2\pi\tau_{\text{eff}})$ as illustrated in Fig. 4.8. In the example, the amplifier noise is comparable to the Johnson noise and phonon noise at frequencies greater than 1 kHz. Therefore, the energy resolution is affected, as will be described in Section 4.15.

The noise equivalent power $\left|\text{NEP}_{\text{Rth}}(f)\right|$ of the Thevenin resistor should be small for frequencies $f < f_0$ in order to obtain the optimal energy resolution given by equation (4.58):

$$\left|\text{NEP}_{\text{Rth}}(f)\right|^2 << \left|\text{NEP}_{\text{VN}}(f)\right|^2 + \left|\text{NEP}_{\text{PN}}(f)\right|^2, \quad \text{for} \quad f < f_0 . \tag{4.71}$$

If the current through the thermometer is measured, the Thevenin equivalent resistance R_{th} should be chosen to be small compared to the thermometer resistance R_0 in order to minimize noise (assuming that the R_{th} resistor is at the same temperatures as the thermometer). The noise can also be minimized by operating with bias or shunt resistors at low temperature.

Noise due to R_{th} for the example microcalorimeter of Section 4.15 is shown in Fig. 4.7 and Fig. 4.8. In the example, the noise due to R_{th} dominates over other sources of noise in the frequencies range of 2 kHz to 10 kHz. Therefore, the energy resolution is significantly poorer than the optimal energy resolution given by equation (4.58).

If the voltage drop across the thermometer is measured instead of the electrical current through it, then the NEP of the noise associated with R_{th} is

$$\left|\mathrm{NEP}_{\mathrm{Rth}}(f)\right| = \left|\frac{C_0}{AL}\right| \left|\mathrm{V}_{\mathrm{VN}}(f)\right| \left|\left(-\tau_{\mathrm{eff}}{}^{-1} + i(2\pi f)\right) + \frac{1}{(i2\pi f + R_0 / L)D(f)}\right|. \qquad (7.72)$$

When measuring the voltage drop across the thermometer, the NEP is minimized by choosing R_{th} to be much larger than R_0.

4.14 Discussion

The optimal resolution of a resistive microcalorimeter was given by equation (4.58), where the current and temperature dependence of the thermistor have been taken into account along with phonon noise and Johnson or other voltage noise. Equation (4.59) describes how the resolution is degraded by limited bandwidth $f_{\max}$ of a measurement. In equation (4.68), we present the total energy resolution including white amplifier noise I_{amp} and noise from other resistors in the electrical circuit.

If the bandwidth $f_{\max}$ is much greater than f_0 as defined in equation (4.60), and if the amplifier noise I_{amp} is small so that inequality (4.70) is satisfied, and if the noise associated with R_{th} is small such that inequality (4.71) is satisfied, then the energy resolution is approximately given by equation (4.58). We now proceed to write the energy resolution given by equation (4.58) in various limits and then compare our results to previous calculations of the energy resolution of a microcalorimeter.

4.14.1 Phonon-noise limited microcalorimeter

In microcalorimeters, the voltage noise is often much less significant than the phonon noise at low frequencies. In the case that the noise equivalent power of the voltage noise at zero frequency is much less than the noise equivalent power of the phonon noise at zero frequency so that $\left|NEP(0)\right| \cong \left|NEP_{\text{PN}}(0)\right|$, the energy resolution in equation (4.58) is approximated by

$$\Delta E_{\text{FWHM}} \cong 2.35\sqrt{\left|\tau_{\text{VN}}\right|\left|\text{NEP}_{\text{VN}}(0)\right|\left|\text{NEP}_{\text{PN}}(0)\right|}\,. \tag{4.73}$$

We now assume that the dominant source of voltage noise is the Johnson noise of the resistive thermometer, which is the optimal case. Using equations (4.53), (4.54), and (4.56) and simplifying, we obtain

$$\Delta E_{\text{FWHM}} \cong 2.35\sqrt{\frac{4k_{\text{B}}{T_0}^2 C_0}{\left|\alpha'\right|}}\sqrt{1+\frac{{T_{\text{bath}}}^2}{{T_0}^2}}\sqrt{\frac{G_0 T_0}{2{I_0}^2 R_0}}\,. \tag{4.74}$$

The above expression can be rewritten using the following expression:

$$\frac{G_0 T_0}{{I_0}^2 R_0} = N\left(1 - \frac{{T_{\text{bath}}}^N}{{T_0}^N}\right)^{-1} \tag{4.75}$$

which is obtained from equation (4.4) by using $G(T) = \partial P_{\text{c}} / \partial T$ and $P_c = P_J = {I_0}^2 R_0$. The result of this substitution is

$$\Delta E_{\text{FWHM}} \cong 2.35\sqrt{\frac{4k_{\text{B}}{T_0}^2 C_0}{|\alpha'|}\sqrt{\frac{N}{2}}}\sqrt{\sqrt{1 + \frac{{T_{\text{bath}}}^2}{{T_0}^2}}\left(1 - \frac{{T_{\text{bath}}}^N}{{T_0}^N}\right)^{-1/2}} . \tag{4.76}$$

This is the optimum energy resolution of a microcalorimeter whose only noise sources are Johnson noise of the thermometer and phonon noise, where the Johnson noise is much less than phonon noise at low frequencies. This approximation gives the energy resolution of a microcalorimeter in terms of five parameters, T_0, T_{bath}, C_0, α', and N. From equation (4.76), we see that energy resolution of a microcalorimeter may be less than the energy fluctuations of a bolometer in thermodynamic equilibrium, $2.35\sqrt{k_{\text{B}}{T_0}^2 C_0}$, which is in agreement with previous theory [1,4].

In the limit that the bath temperature T_{bath} is much smaller than T_0, equation (4.76) reduces to

$$\Delta E_{\text{FWHM}} \cong 2.35\sqrt{\frac{4k_{\text{B}}{T_0}^2 C_0}{|\alpha'|}\sqrt{\frac{N}{2}}} . \tag{4.77}$$

The optimal resolution of a microcalorimeter in equation (4.77) is similar to the result obtained by Irwin [1] for the special case of a voltage-biased transition-edge sensor in extreme electrothermal feedback where the only noise sources are Johnson noise and

phonon noise. However, the α' term is defined differently than α was by Irwin and others. We describe the difference in definition in more detail below.

In the limit that $T_0 - T_{\mathrm{bath}}$ is small, we can make the approximation that $1 + {T_{\mathrm{bath}}}^2 / {T_0}^2 \cong 2$ and $1 - {T_{\mathrm{bath}}}^N / {T_0}^N \cong N(1 - T_{\mathrm{bath}} / T_0)$. In this approximation, equation (4.76) reduces to

$$\Delta E_{\mathrm{FWHM}} \cong 2.35 \sqrt{\frac{4 k_{\mathrm{B}} {T_0}^2 C_0}{|\alpha'|} \left(1 - \frac{T_{\mathrm{bath}}}{T_0}\right)^{-1/2}} \,. \tag{4.78}$$

Equation (4.78) is similar to the result obtained by Irwin [1] for a current-biased or voltage-biased transition-edge sensor with negligible feedback, where the only sources of noise are Johnson noise and phonon noise.

There are some important differences between our result and the previous results by Irwin. Because our derivation is more general, results given in equations (4.58) and (4.76) apply no matter whether the feedback is extreme, strong, weak, or negligible and apply for both positive and negative α'. The microcalorimeter may be current or voltage biased. Our model includes effects of the inductance L. The current dependence of the resistive thermometer is included in our model and is represented by the β parameter. The temperature dependence of the heat capacity is also included and is represented by the γ parameter. The coupling between the electrical and thermal circuits is explicitly represented by the τ_{etc} parameter. Our theory resembles the previous theory of Irwin only in the limit that L, β and γ are small. Also, the form of our result is very different if the Johnson noise is not small compared to the phonon noise at low frequencies or if other forms of noise are included.

4.14.2 Voltage-noise limited microcalorimeter

As an example of how our results can differ from previous results, we consider the case in which voltage noise is much larger than the phonon noise at all frequencies so that $\left|\mathrm{NEP}(0)\right| \cong \left|\mathrm{NEP}_{\mathrm{VN}}(0)\right|$. This may apply when a microcalorimeter is operated at low power or when α' is small. In this case, the energy resolution in equation (4.58) is approximated by

$$\Delta E_{\mathrm{FWHM}} \cong 2.35\sqrt{\left|\tau_{\mathrm{VN}}\right|\left|\mathrm{NEP}_{\mathrm{VN}}(0)\right|^2}\ . \tag{4.79}$$

We assume, as before, that the voltage noise is dominated by Johnson noise in the thermometer. We then use equations (4.53) and (4.54) to obtain

$$\Delta E_{\mathrm{FWHM}} \cong 2.35\sqrt{\frac{4k_{\mathrm{B}}{T_0}^2 C_0}{\alpha'^2\left|\tau_{\mathrm{VN}}\right|}\frac{C_0 T_0}{{I_0}^2 R_0}}. \tag{4.80}$$

Note that the approximation in equation (4.80) is not valid in the limit that τ_{VN} is so large that the phonon noise is larger than the voltage noise. Equation (4.80) is the energy resolution of a microcalorimeter whose dominant source of noise at all frequencies is Johnson noise from the thermometer. When equation (4.80) is a valid approximation, the energy resolution E_{FWHM} in equation (4.80) is larger (worse) than the energy resolution given in equation (4.79).

4.14.3 Resolution limited by and phonon noise and voltage noise

A more general but more complex expression can be similarly obtained from equation (4.58), without using the approximations $\left|NEP(0)\right| \cong \left|NEP_{\mathrm{PN}}(0)\right|$ or $\left|NEP(0)\right| \cong \left|NEP_{\mathrm{VN}}(0)\right|$. This expression is

$$\Delta E_{\mathrm{FWHM}} = 2.35\sqrt{\left|\tau_{\mathrm{VN}}\right|\left|\mathrm{NEP}_{\mathrm{VN}}(0)\right|\sqrt{\left|\mathrm{NEP}_{\mathrm{VN}}(0)\right|^2 + \left|\mathrm{NEP}_{\mathrm{PN}}(0)\right|^2}} \,. \qquad (4.81)$$

Equation (4.81) is just a combination of equation (4.73) and equation (4.79) with the terms in the radical added in quadrature. We now assume as before that the voltage noise is due to Johnson noise in the thermometer. We substitute into equation (4.81) using equations (4.73), (4.74), (4.79) and (4.80). We then obtain

$$\Delta E_{\mathrm{FWHM}} = 2.35\sqrt{4k_{\mathrm{B}}{T_0}^2 C_0\sqrt{\frac{1}{\alpha'^2}\left(1+\frac{{T_{\mathrm{bath}}}^2}{{T_0}^2}\right)\left(\frac{G_0 T_0}{2{I_0}^2 R_0}\right)+\frac{1}{\alpha'^4\left|\tau_{\mathrm{VN}}\right|^2}\left(\frac{C_0 T_0}{{I_0}^2 R_0}\right)^2}} \,, (4.82)$$

which is the resolution of a microcalorimeter limited by phonon noise and Johnson Noise

As previously described, the thermometer sensitivity parameter α' is defined as a partial derivative to be evaluated at the operating point with the current held fixed, whereas in previous theory [1,3,4], the sensitivity α is defined as a total derivative. For most thermometers, including all transition-edge sensors, the value of α' at the operating point is smaller than α measured at low current. Therefore, measurements of α at lower current overestimate the value of α' at the operating point. For example, in one of our devices, we measured resistance versus temperature at a constant voltage V_0=20 nV. From this measurement, we obtained $\alpha = 540$ at a bias current of I_0=100 nA. However, a much lower sensitivity $\alpha \cong 100$ was inferred from the height of measured pulses at higher current I_0=18 μA.

In this section, we described the energy resolution of a microcalorimeter in several special cases. However, in the general case of a microcalorimeter with phonon noise and white voltage noise, equation (4.58) should be used to compute the optimal energy resolution. We

will use equation (4.58) to calculate the resolution of an example microcalorimeter in Section 4.15.

4.15 Example of a TES microcalorimeter

We will now use our general microcalorimeter theory to model a specific device as an illustration of how the theory is applied. We model a hypothetical device that closely resembles microcalorimeters which we have fabricated and tested in our laboratory. Descriptions of actual devices are avoided because consideration of experimental uncertainties in the parameters and various noise sources would complicate the discussion.

We model an x-ray detector based on transition-edge-sensor (TES) technology. The detector layout is shown in Fig. 4.9. It is a thin film device which consists of a photon absorber made of copper coupled to a small TES thermometer. The absorber dimensions are 250 μm by 250 μm by 3 μm. The absorber dominates the heat capacity of the microcalorimeter. At an operating temperature of 120 mK, its heat capacity is C_0=2.2 pJ/K. The parameter γ=1 because it is a normal metal.

The TES is a thin film of superconductor biased in the phase transition between the superconducting and normal states. In the phase transition, the resistance $R(I,T)$ increases with increasing temperature T and increasing current I from zero resistance up to the normal metal resistance R_{N}. Fig. 4.10 is an illustration of the phase transition. The α' and β parameters of a TES depend on how it is fabricated and upon the operating temperature T_0 and the bias current I_0. We have made TES thermometers with α' as large as several thousand, but α' equals 100 is more typical at bias conditions. We estimate $\beta \cong 3$ from measurements of one device.

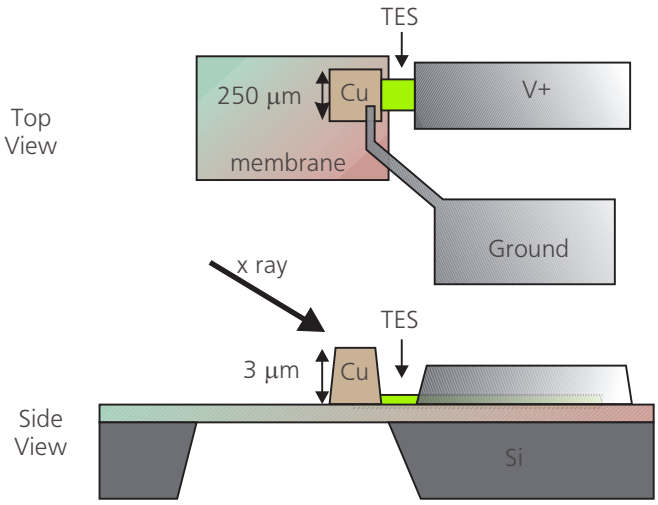

Figure 4.9. A model microcalorimeter closely resembling devices fabricated and tested in our laboratory. The device consists of a copper x-ray absorber that is well coupled to a small transition-edge-sensor (TES) thermometer. Most of the device is on a thin membrane which thermally decouples it from the silicon substrate. The bonding pads which connect the thermometer to the electrical bias circuit are also shown. X rays absorbed in the absorber cause temperature pulses which are measured by the thermometer.

The microcalorimeter is deposited on a silicon substrate which suspends a silicon nitride membrane. The substrate functions as the microcalorimeter's cold bath with temperature T_{bath}. Most of the microcalorimeter lies on the membrane, which thermally decouples it from the bath. A small part of the device lies directly on top of the silicon substrate, providing a small thermal coupling G_0. At 120 mK, this thermal coupling is limited by electron-phonon interaction which implies N=5. The thermal conductivity within the microcalorimeter is large compared to G_0. Therefore, the whole microcalorimeter acts as one thermal element with temperature T.

The model parameters for the described microcalorimeter are given in Table 4.1. We have taken the values of G_0, I_0, R_0, R_{th}, and T_{bath} from actual measurements of a TES microcalorimeter that we fabricated. (Note that the parameter G_0 is related to the other parameters by equation (4.75). The measured value of G_0 given in Table 4.1 is 24% less

than an estimate of G_0 that is obtained from equation (4.75) due to experimental uncertainty in the parameters G_0, I_0, R_0, N, T_0, and T_{bath}.) The values were obtained from measurements of a microcalorimeter that had TES with a phase transition at T_c=123 mK. The width of the transition varied from 0.25 mK at a bias current I of 0.1 μA to several millikelvin wide at a bias current I=18 μA. The value $\alpha' = 100$ is a rough estimate for that device based on measurements of pulse amplitudes and based on the assumption that $\beta \cong 3$. In our experiments, the inductance L is about 0.3 μH. In our example, we choose L=10 μH so that the rise time is more easily visible in our figures.

The electrical circuit of the example microcalorimeter is shown in Fig 4.2. In our example, the bias voltage is V_b=1.2 V, the shunt resistance is R_s=20 mΩ, and bias resistor is R_b=11 kΩ. Hence, the Thevenin equivalent voltage is V_{th}=2.2 μV and the Thevenin equivalent resistance is R_{th}=20 mΩ. The current through the inductor L is measured by a dc SQUID. In our experiments, the current noise from R_s is larger than the noise due to R_b because the resistor R_s is at temperature T_s=2 K. Therefore, its Johnson noise voltage is $\left|V_{\text{Rth}}(f)\right| = \sqrt{4k_b R_s T_s} = 1.4 \text{ pV}/\sqrt{\text{Hz}}$.

The operating point of a TES microcalorimeter in the superconducting to normal metal phase transition is illustrated in Fig. 4.10. The operating point is determined by constraints described in Section 4.3. As shown in the figure, the operating point lies on the transition between the superconducting and normal states. The operating temperature for the example device was estimated to be T_0=120 mK.

When a photon is absorbed in the microcalorimeter, its energy is rapidly thermalized in the absorber and thermometer electrons, and the TES thermometer measures the increase in electron temperature. The response of the microcalorimeter is described by the matrix constants which are computed from the basic parameters in Table 4.1 as described in

Section 4.4. The matrix constants are given in Table 4.2. We note that the electronic time constant τ_{el} is smaller than the L/R time constant due to β being positive. The effective thermal time constant τ_{eff} is positive and is less than τ_{th} because strong Joule heating is causing pulse shortening.

At this point, we can determine that the microcalorimeter is stable and not oscillatory using inequalities (4.23), (4.24), and (4.25). However, if the inductance L were three times larger, then the microcalorimeter would be oscillatory due to current bias at high frequencies. If the inductance L were ten times larger, the microcalorimeter would be unstable.

We can compute pulse shape as described in Section 4.5 from the values in Table 4.2. The pulse shape parameters are given in Table 4.3. We note that the rise time τ_{r} is similar to electrical time constant τ_{el}. Using the values in Table 4.3, we now compute the response of the system to a 6 keV x-ray absorption. The resulting current pulse is plotted in Fig. 4.11, which shows that the absorption event causes a temporary decrease in current I. The associated temperature pulse is plotted in Fig. 4.12. A plot of current vs. temperature is

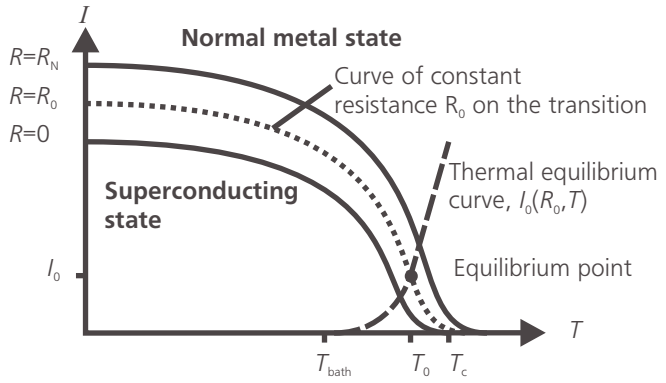

Figure 4.10. An illustration of an operating point of a TES microcalorimeter. The point where the thermal equilibrium curve, which is described by equation (4.4), intersects the curve of constant resistance R_0, which is described by equation (4.5), is the operating point. The operating point lies in the phase transition between the superconducting and normal metal states.

shown in Fig. 4.3. An illustration of the pulse in the context of the superconductor to normal phase transition is shown in Fig. 4.13. As shown in Fig. 4.3 and Fig. 4.12, the absorption event causes the temperature to rise by about 4 mK. After the absorption event, the temperature continues to rise during the rise time of the current pulse due to increased Joule heating as shown in Fig. 4.12. The additional Joule heating occurs because the inductance L provides a current bias at high frequencies. The current and temperature return to equilibrium during the decay of the current pulse.

Section 4.10, Section 4.11 and Section 4.13 describe how to compute various noise sources in the microcalorimeter. We compute the phonon noise, Johnson noise due to the resistance R_0 of the TES, amplifier noise, and noise due to the shunt resistor. Other sources of noise in the electronic bias circuit are assumed to be negligible. The phonon noise and Johnson noise are computed from the parameters in Tables 4.1 and 4.2. The amplifier noise is

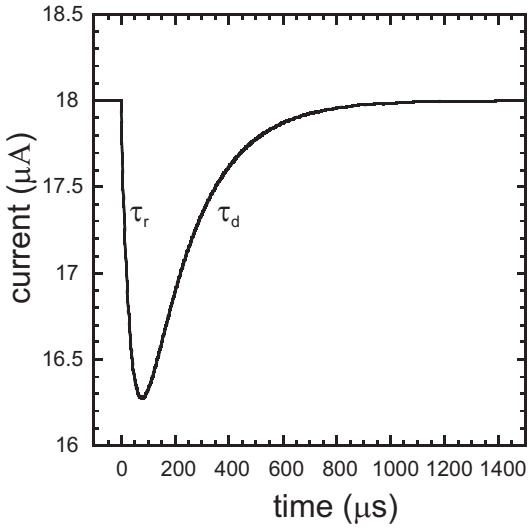

Figure 4.11. A current pulse in the example TES microcalorimeter. In the example, the current drops in response to the absorption of an 6 keV x ray. The current returns to equilibrium in about a millisecond. Note that the inductance chosen for this example is much larger than actual inductances used in order to better illustrate the rise time.

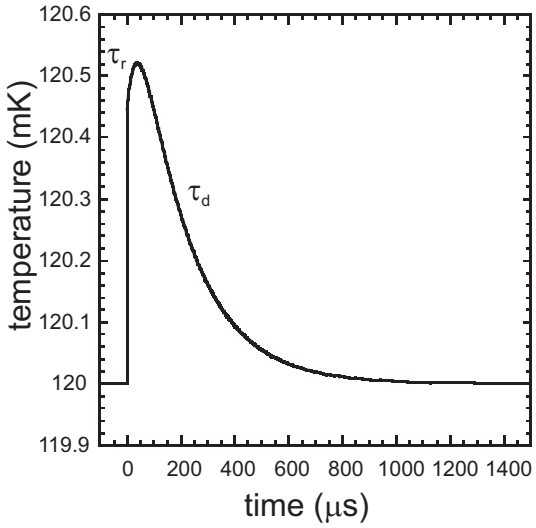

Figure 4.12. A temperature pulse in the example TES microcalorimeter. In the example, the temperature is increased by over 0.4 mK by the absorption of a 6 keV x ray. The temperature continues to rise after the absorption due to increased Joule heating. This occurs because the inductance in the circuit provides a current bias at high frequencies. The temperature is returned to equilibrium in about a millisecond. Note that the inductance chosen for this example is much larger than actual inductances used in order to better illustrate the rise time.

assumed to be $\left|I_{\text{amp}}\right| = 2 \text{ pA} / \sqrt{\text{Hz}}$, which is typical of large-bandwidth low-temperature dc SQUIDs. A plot of current noise from these sources is given in Fig. 4.7. The phonon noise dominates at low frequencies. It rolls off as the gain of the microcalorimeter decreases with increasing frequency. In this microcalorimeter, the phonon noise begins rolling of at frequency $1/(2\pi\tau_{\text{eff}})$

At low frequencies, Johnson noise in the microcalorimeter is suppressed due to the two Johnson noise terms partially canceling as described in Section 4.10 The cancellation of the Johnson noise is most significant at low frequencies because electrothermal feedback is strongest at low frequencies. The Johnson noise begins to increase at frequency $1/(2\pi\tau_{\text{VN}})$, but then decreases at frequencies greater than $1/(2\pi\tau_{\text{el}})$ due to inductance L in the electrical circuit. For the modeled microcalorimeter, the phonon noise is larger than

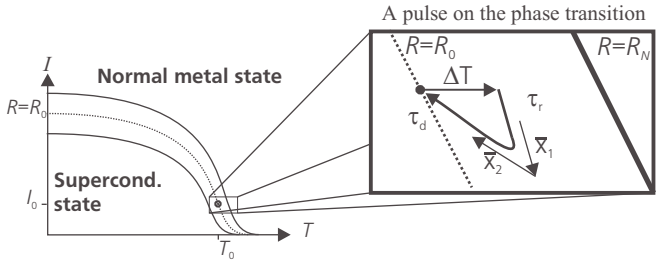

Fig. 4.13. An illustration of a pulse from the example TES microcalorimeter. The directions of the eigenvectors x_1 and x_2 from equations (4.20) and (4.21) are also plotted.

the Johnson noise at low frequency. If the Johnson noise were larger than the phonon noise, the energy resolution would be significantly degraded.

Noise equivalent powers of various noise sources are described in Sections 4.11 and Section 4.13. The noise equivalent powers of the noise sources in the example microcalorimeter are shown in Fig. 4.8. At very high frequencies, the gain of the microcalorimeter is small. Therefore, the noise equivalent power of the amplifier noise and Johnson noise are large at high frequencies.

The time constant τ_{VN} and the noise equivalent powers at zero frequency are given in Table 4.4. These were computed using the data from Tables 4.1 and 4.2. Using these values and equation (4.58), we compute the best possible energy resolution obtainable from the example microcalorimeter: E_{FWHM}=3.0 eV. However, the energy resolution may be worse if a low pass filter were applied to the device. Energy resolution is significantly degraded if the band pass is less than $f_0 = 4700$ Hz as described in Section 4.12 Amplifier noise also degrades the resolution. Using equation (4.70), we find that the amplifier noise should be significantly less than $2.1\ \mathrm{pA}/\sqrt{\mathrm{Hz}}$ in order to avoid degradation of the energy resolution. Since the amplifier noise is $2.0\ \mathrm{pA}/\sqrt{\mathrm{Hz}}$, the best possible energy resolution with this amplifier noise is E_{FWHM}=3.8 eV. This result is obtained from equation (4.68) by

including amplifier noise but neglecting noise V_{Rth} from the shunt resistor R_{s}. The noise due to the shunt resistor R_{s} is shown Fig. 4.7 and Fig. 4.8. It is the dominant noise source in the frequency range of 2 kHz to 10 kHz. Therefore, the noise V_{Rth} significantly affects the energy resolution of the example microcalorimeter. Using equation (4.68), we find that the energy resolution of the example microcalorimeter including amplifier noise and shunt resistor noise is E_{FWHM}=5.2 eV.

Parameter	Value
α'	100
β	3
γ	1
C_0	2.2 pJ / K
G_0	1.8 nW / K
I_0	18 μA
L	10 μH
N	5
R_0	100 mΩ
R_{s}, R_{th}	20 mΩ
T_0	120 mK
T_{bath}	100 mK
T_s	2.0 K

Table 4.1. The basic parameters for the example microcalorimeter. The parameters are chosen to model a hypothetical TES microcalorimeter illustrated in Fig. 4.9. The model microcalorimeter closely resembles actual microcalorimeters fabricated and tested. A hypothetical device is used in order to simplify the exposition of the theory.

Constant	Value	Equation
$L/(R_{th}+R_0)$	83 μs	
τ_{el}	24 μs	4.7
C_0/G_0	1.2 ms	
τ_{th}	1.4 ms	4.10
τ_{J}	82 μs	4.12
τ_{eff}	87 μs	4.9
A	150 $\mathrm{As^{-1}K^{-1}}$	4.14
B	4.1×10^{6} $\mathrm{Ks^{-1}A^{-1}}$	4.15
τ_{etc}	40 μs	4.16

Table 4.2. The basic time constants and cross terms in the linear model.

Constant	Value	Equation
τ_{r}	40 μs	4.18
τ_{d}	190 μs	4.19
E	6 keV	
$\Delta T \approx E/C_0$	0.44 mK	

Table 4.3. Parameters that describe the shape of the pulses in the microcalorimeter.

Constant	Value	Equation
$NEP_{JN}(0)$	1.0×10^{-18} W Hz$^{-1/2}$	4.53, 4.54
$NEP_{PN}(0)$	3.5×10^{-17} W Hz$^{-1/2}$	4.56
$NEP_{AMP}(0)$	3.9×10^{-18} W Hz$^{-1/2}$	4.61
$NEP_{Rth}(0)$	2.5×10^{-17} W Hz$^{-1/2}$	4.64
τ_{VN}	1.2 ms	4.47

Table 4.4. The parameters that describe the noise in the model microcalorimeter

4.16 Summary of the simple microcalorimeter theory

The microcalorimeter theory is a comprehensive dynamical model of resistive microcalorimeters including both temperature and current dependencies of the thermistor. The model describes the behavior of a wide variety of microcalorimeters including semiconductor thermistors $(\alpha' < 0)$ and transition-edge sensors $(\alpha' > 0)$. Various bias conditions are described including current bias, voltage bias, and either weak or strong electrothermal feedback. The model describes the behavior of microcalorimeters in terms of eleven independent parameters: α', β, γ, C_0, I_0, L, N, R_0, R_{th}, T_0, and T_{bath}. Using the model, we determined constraints on the stability of microcalorimeters, and in equation (4.58) we present a general expression for the theoretical limiting energy resolution. Because the model explicitly accounts for both temperature and current fluctuations, the effects of various forms of noise were readily incorporated. In equation (4.68), we present an expression for the total energy resolution of microcalorimeter including amplifier noise and noise from bias or shunt resistors. The formalism is simpler and more general than the formalism in previous models. Therefore, the model can be easily expanded to describe composite bolometers where the absorber and sensor are treated as separate elements. Because the model is simple and comprehensive, it adds insight. The insight provided by

the model has assisted us in the design of our microcalorimeters and in the interpretation of our data.

4.17 Extension of the theory to more complicated calorimeters

The microcalorimeter theory can be extended to more complicated microcalorimeters. As an example, consider the calorimeter illustrated in Fig. 4.14. In this case, the resistive thermometer has temperature T_1 and the absorber has temperature T_2. This type of microcalorimeter is described by three independent variables: the current I, and the two temperatures T_1 and T_2. (Previous authors have described this case without including the current I as a dynamic variable [9].) The thermometer has heat capacity C_1 and the absorber has heat capacity C_2. The thermal conductance G_1 couples the thermometer to the bath. The absorber is coupled the absorber by thermal conductance G_2. (This model resembles some of the gamma-ray calorimeters we have fabricated.)

The electrical circuit is still the same:

$$L\frac{dI}{dt} = V_{\text{th}} - I(R_{\text{th}} + R(I, T_1)), \tag{4.83}$$

where the terms in the equation are defined as described in Section 4.2.1. The thermal circuit is described by two equations. One equation describes the rate of change of the temperature of the thermometer:

$$C_1(T_1)\frac{dT_1}{dt} = P_{\text{J}}(I, T_1) - P_{\text{c}}(T_1, T_{\text{bath}}) + P_{\text{at}}(T_1, T_2), \tag{4.84}$$

where the Joule heating power P_J and the cooling power P_c into the bath are as described in Section 4.2.2. The heat that flows between the absorber and the thermometers is described by the power P_{at}.

The second thermal equation describes the rate of change of the temperature in the absorber:

$$C_2(T_2)\frac{dT}{dt} = -P_{at}(T_1, T_2) + P_{abs}(t), \tag{4.85}$$

where P_{abs}(t) is the power due to the absorption events in the absorber, as was described in Section 4.2.2.

The equations are linearized around equilibrium as was done for a simple microcalorimeter in Section 4.4. The linearized equations are

$$\frac{d}{dt}\begin{pmatrix} \delta I \\ \delta T_1 \\ \delta T_2 \end{pmatrix} = \begin{pmatrix} -\tau_{el} & \text{-A} & 0 \\ B & \tau_{11} & \tau_{21} \\ 0 & \tau_{12} & -\tau_{22} \end{pmatrix}\begin{pmatrix} \delta I \\ \delta T_1 \\ \delta T_2 \end{pmatrix} + \begin{pmatrix} 0 \\ 0 \\ P_{abs}(t)/C_2 \end{pmatrix}, \tag{4.86}$$

where A, B, and τ_{el}, are as defined in Section 4.4. The thermal time constants are $\tau_{11} = \partial(-P_c + P_{at})/\partial T_1$, $\tau_{21} = \partial P_{at}/\partial T_1$, $\tau_{12} = -\partial P_{at}/\partial T_1$ and $\tau_2 = -\partial P_{at}/\partial T_2$. The eigenvalues and eigenvectors of the matrix in equation (4.86) are used to find the response of the microcalorimeter to an absorption event as was described for a simple microcalorimeter in Section 4.5. The Fourier transform of equation (4.86) into frequency f is

$$\mathbf{M}\begin{pmatrix} \delta I \\ \delta T_1 \\ \delta T_2 \end{pmatrix} = \begin{pmatrix} 0 \\ 0 \\ P_{abs}(f)/C_2 \end{pmatrix}, \tag{4.87}$$

where

$$\mathbf{M} = -\begin{pmatrix} -\tau_{\mathrm{el}} - 2\pi f & \text{-A} & 0 \\ B & \tau_{11} - 2\pi f & \tau_{21} \\ 0 & \tau_{12} & -\tau_{22} - 2\pi f \end{pmatrix}. \tag{4.88}$$

The solution is

$$\begin{pmatrix} \delta I \\ \delta T_1 \\ \delta T_2 \end{pmatrix} = \mathbf{M}^{-1} \begin{pmatrix} 0 \\ 0 \\ P_{\mathrm{abs}}(f)/C_2 \end{pmatrix}, \tag{4.89}$$

where $\mathbf{M}^{-1}$ is the inverse of matrix $\mathbf{M}$. Noise terms are included into the linear model as was done for the simple microcalorimeter in Section 4.10. The solution with noise sources

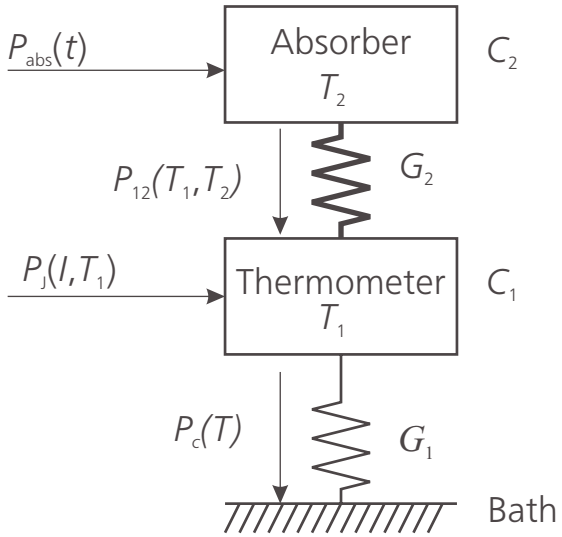

Figure 4.14 A two-element calorimeter. The thermometer is coupled to the cold bath by a thermal conductance G_1. The thermometer is coupled to the absorber by a thermal conductance G_2. The conductance G_2 causes additional phonon noise in the calorimeter. The effects of the phonon noise from G_2 cancel out at low frequencies. This phonon noise adversely affects the energy resolution of the calorimeter unless the conductivity G_2 is very large.

is

$$\begin{pmatrix} \delta I \\ \delta T_1 \\ \delta T_2 \end{pmatrix} = \mathbf{M}^{-1} \begin{pmatrix} V_{VN}(f)/L \\ I_0 V_{VN}(f) + P_{PN1}(f)/C_1 - P_{PN2}(f)/C_1 \\ + P_{PN2}(f)/C_2 + P_{\mathrm{abs}}(f)/C_2 \end{pmatrix}, \tag{4.90}$$

where V_{VN} represents voltage fluctuations due to electronic noise in the thermometer, P_{PN1} is the phonon noise along G_1, and P_{PN2} is the phonon noise along G_2.

The phonon noise P_{PN2} affects both temperature T_1 of the thermometer and temperature T_2 of the absorber by randomly moving energy back and forth between the absorber and the thermometer. However the thermal coupling G_2 tends to equalize the two temperatures. In the limit that G_2 is large compared to $\alpha' G_1$, the absorber and thermometer are well coupled. In this case, the effects of P_{PN2} on the two temperatures cancel. The calorimeter is then equivalent to the simple calorimeter described in the previous sections of this chapter.

If G_2 is not large compared to $\alpha' G_1$, then the phonon noise P_{PN2} produces additional noise that degrades the energy resolution of the calorimeter. At high frequencies (such that $2\pi f$ is much greater than G_2/C_2), the thermometer and absorber are decoupled. (This is the bolometric mode.) In this frequency range, the thermometer measures phonon noise from both P_{PN1} and P_{PN2}. The calorimeter acts like a simple calorimeter with heat capacity C_1 and thermal coupling G_1+G_2, except that the signal from $P_{\mathrm{abs}}(t)$ in the absorber is not well coupled into the thermometer at these frequencies. (I call this the small calorimeter limit because the temperature fluctuations measured by the thermometer depend on capacity C_1 only).

For low frequencies (such that $2\pi f$ is much less than G_2/C_2), the absorber is well coupled to the thermometer. (This is the calorimetric mode.) The calorimeter acts like a simple calorimeter with heat capacity C_1+C_2 and has phonon noise due to P_{PN1} only. (I often refer

to the low frequency limit as the big calorimeter limit because at low frequencies the fluctuation in the temperature measured by thermometer depend on the combined heat capacities of the absorber and the thermometer.)

The noise equivalent power (NEP) of the various noise sources is easily calculable from equation (4.90). For example, the NEP of the phonon noise P_{PN2} is $|(C_2(\mathbf{M}^{-1})_{12} / C_1(\mathbf{M}^{-1})_{13} - 1)||P_{PN2}|$. The NEP of all the noise sources can be computed and inserted into equation (4.57) to calculate the optimal energy resolution.

[1] K. D. Irwin, "Phonon-Mediated Particle Detection Using Superconducting Tungsten Transition-Edge Sensors," Ph.D. Thesis, Stanford, 1995.

[2] R. Clark Jones, "The General Theory of Bolometer Performance," Optical Society of America **43**, 1 (1953).

[3] J. C. Mather, "Bolometer noise: nonequilibrium theory," Applied Optics **21** (6), 1125-9 (1982).

[4] S. H. Moseley, J. C. Mather, and D. McCammon, "Thermal detectors as X-ray spectrometers," Journal of Applied Physics **56** (5), 1257-62 (1984).

[5] P. L. Richards, "Bolometers for infrared and millimeter waves," Journal of Applied Physics **76** (1), 1-24 (1994).

[6] J. C. Mather, "Electrical self-calibration of nonideal bolometers," Applied Optics **23** (18), 3181-3 (1984).

[7] M. Frank, D. Dummer, S. Cooper *et al*., "A calorimetric particle detector using an iridium superconducting phase transition thermometer," Nuclear Instruments & Methods in

Physics Research, Section A (Accelerators, Spectrometers, Detectors and Associated Equipment) **345** (2), 367-78 (1994).

[8] P. Ferger, P. Colling, S. Cooper *et al*., "A massive cryogenic particle detector with good energy resolution," Physics Letters B **323** (1), 95-8 (1994).

[9] F. Probst, M. Frank, S. Cooper *et al*., "Model for cryogenic particle detectors with superconducting phase transition thermometers," Journal of Low Temperature Physics **100** (1-2), 69-104 (1995).

[10] T. Shutt, D. S. Akerib, P. D. Barnes, Jr. *et al*., "Progress of the Cryogenic Dark Matter Search (CDMS) experiment," Nuclear Physics B, Proceedings Supplements **51** (B), 318-22 (1996).

[11] H. V. Klapdor-Kleingrothaus and Y. Ramachers, "Experiments aiming at direct detection of dark matter," European Physical Journal A **3** (1), 85-92 (1998).

[12] D. S. Akerib, P. D. Barnes, Jr., D. A. Bauer *et al*., "Preliminary limits on the WIMP-nucleon cross section from the cryogenic dark matter search (CDMS)," Nuclear Physics B, Proceedings Supplements **70**, 64-8 (1999).

[13] J. C. Mather, "Bolometers: ultimate sensitivity, optimization and amplifier coupling," Applied Optics **23** (4), 584-8 (1984).

[14] C. M. Knoedler, "Phase-slip shot noise contribution to excess noise in superconducting bolometers," Journal of Applied Physics **54** (5), 2773-6 (1983).

[15] A. E. Szymkowiak, R. L. Kelley, S. H. Moseley *et al*., "Signal processing for microcalorimeters," Journal of Low Temperature Physics **93** (3-4), 281-5 (1993).

Chapter 5

FABRICATION

5.1 Introduction to fabrication

Much of our research has been toward the development of transition-edge sensor microcalorimeters for the measurement of x-rays. An illustration of a prototypical device is given in Fig. 1.6. The microcalorimeter consists of a thin-film x-ray absorber well coupled to a thin-film TES thermometer. The device is deposited on a silicon substrate with a suspended membrane. Much of the microcalorimeter lies on top of the membrane so that it is thermally decoupled from the substrate when in operation. In this chapter, we discuss the fabrication of these devices. We describe how the thin membrane is fabricated and how metal films are deposited and patterned into the components of our microcalorimeters.

5.2 Fabrication of substrates for our x-ray microcalorimeters

We fabricated special substrates that suspend thin membranes for use with our microcalorimeters, shown in Fig. 5.1. To make these substrates, we begin with a four-inch diameter silicon wafer. A 0.5 μm thick layer of silicon nitride is deposited on all sides of the wafer. We remove an array of squares in the silicon nitride on the backside of the wafer by use of a reactive ion etch. The wafer is then chemically etched from the backside with a potassium hydroxide solution. The solution etches silicon, but does not significantly etch the silicon nitride. When the wafers are placed in the etching solution, the silicon is etched away in the areas not covered by silicon nitride. The potassium hydroxide solution is

allowed to etch the silicon all the way through to the front side of the wafer, leaving a thin membrane of silicon nitride suspended across the removed sections of silicon.

The silicon crystal is more resistant to etching by potassium hydroxide in the (1, 1, 1) lattice directions than in other directions. The etch preferentially removes silicon in other directions leaving surfaces perpendicular to the (1, 1, 1) lattice directions. The (1, 1, 1)

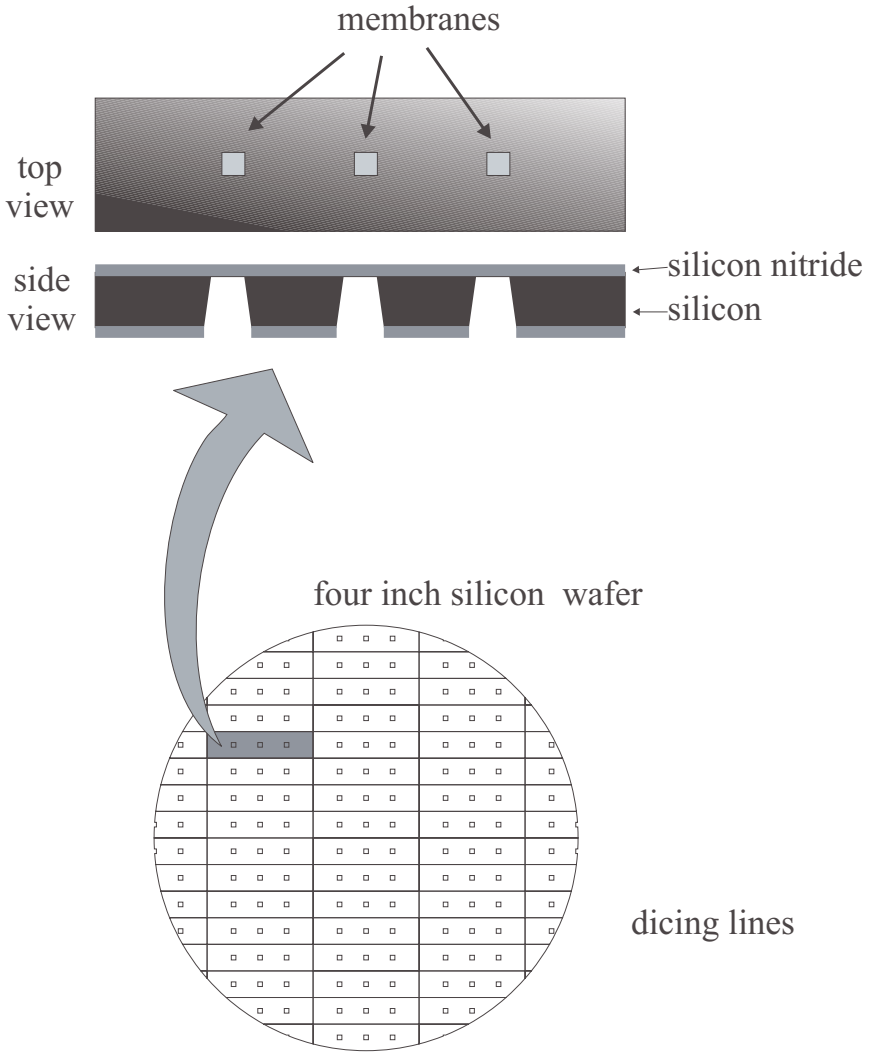

Figure 5.1. Our 1 inch by ¼ inch substrates are fabricated by etching and dicing a four-inch silicon wafer.

directions are 54.74 degrees from vertical. Thus, the cavities below the membranes slope in by 54.74 degrees above horizontal. After the etch, the four inch wafers with suspended membranes are then diced into one inch by one quarter inch wafers. Each one inch by one quarter inch wafer suspends three silicon nitride membranes as shown in Fig. 5.1. Each membrane has dimensions 1.1 mm by 1.1 mm.

Our microcalorimeters are fabricated on top of the one-inch substrates with membranes in our thin film deposition system, which is illustrated in Fig. 5.2. The system was constructed to a large extent by Harrie Netel [1], a fellow graduate student in the cryogenic detector group at Lawrence Livermore National Laboratory. The thin-film deposition system has a load lock for loading samples, and a main chamber for sputtering and ion gunning. The load lock is brought up to atmospheric pressure when samples are loaded into it. It is pumped down to about 10^{-7} Torr otherwise. The main chamber is kept at about 10^{-9} Torr, except during sputtering, ion gunning, or when a sample is being transferred between the load lock and the main chamber.

A precisely machined sample holder, which we call the Ferrari, is shown in Fig. 5.3. When a device is to be fabricated, a substrate is placed in the Ferrari, along with a shadow mask if one is used. The Ferrari holds the mask firmly in position, pressed directly onto the surface of the substrate. The Ferrari is placed in the load lock. After the load lock is pumped down, a gate valve which separates the load lock from the main chamber is opened and the Ferrari is transferred into position for sputtering or ion milling in the main chamber. The gate valve is closed and the main chamber is pumped down before sputtering or ion milling begins.

5.3 Deposition and patterning of thin films

5.3.1 Sputtering

The main chamber of our thin-film deposition system has three sputter guns, which are used to deposit the metal films that comprise our microcalorimeters. One of the guns has a copper target. A second gun has aluminum. The third (tantalum) sputter gun is not used for fabrication of the x-ray microcalorimeters described in this thesis. For sputtering, argon gas is supplied to the system so that the pressure is 10 mTorr of argon. In operation, a sputter gun creates an argon plasma above the sputter target. The sputter guns are biased with a voltage of several hundred volts, which causes a current of argon ions which impact the sputter targets. The ion impacts sputter metal off the surface of the targets. The sputtered metal atoms and molecules radiate upward from the targets and coat surfaces they impinge upon including the exposed surface of the substrate, thereby forming the metal layers of our microcalorimeters. The thickness of the sputtered films is controlled by the electrical power applied to the argon plasma and by the duration the sputtering. (Usually, the power is from 50 W to 200 W, and the duration of sputtering several minutes, depending on the material

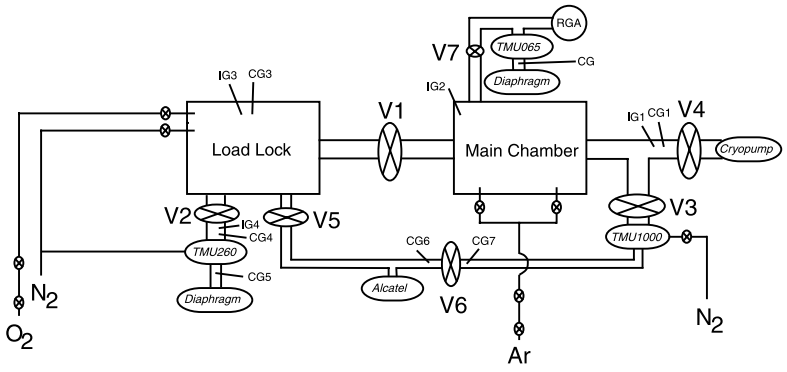

Figure 5.2 A schematic of our thin-film deposition system. Various gate valves are labeled V1 though V7. The pressure in the system is measured by an number of ion gauges and convectron gauges. Samples are loaded into the load lock and then transferred to the main chamber where films are deposited.

sputtered and the thickness of desired film.)

5.3.2 Shadow masking

Shadow masks are thin metal masks which have patterns of holes cut in them corresponding the two dimensional shape of the films to be deposited on the substrate. These masks can pattern structures as small as about $50\ \mu\text{m}$. A shadow mask can have up to eight different patterns for our one inch by one quarter inch substrates. A shadow mask is held just in front of the substrate by the Ferrari, as shown in Fig. 5.3. A shadow mask manipulator, located in the load lock, allows an operator to select the shadow mask pattern to be deposited. The position of the shadow mask can be changed in vacuum, as can the choice of metal to be sputtered, so that several different patterns made of different metals can be deposited without breaking vacuum.

A major disadvantage of shadow mask technology for us is that patterns formed by sputtering through shadow masks are somewhat poorly defined because the sputter target is not a point source. The edges of films sputtered through our shadow mask system are sloped, and about ten microns wide (measured from the 90% to 10% the film thickness). Shadow masking is used to form the absorber and bonding pads of our microcalorimeters because these structures need not have particularly sharp edges

5.3.3 Lift-off

We use a photolithographic lift-off process to obtain films with much sharper edges. In this process, a substrate is coated with photoresist in a clean room and baked so that the photoresist forms a solid layer on the top surface of the substrate. An ultraviolet light and a photomask are used to expose a pattern in the photoresist. The exposed pattern of photoresist is removed, leaving the exposed surface of the substrate where the photo resist was removed. This process produces a mask of photoresist on the surface of the substrate. The substrate with photoresist mask is placed in the thin-film deposition system and

sputtered without a shadow mask. The sputtered films coat the photoresist layer and the exposed sections of substrate. After the sputtering is completed, the substrate is removed from the thin-film deposition system, and it is placed in acetone. The acetone dissolves the photoresist. The metal that is deposited on top of the photoresist flakes off, but the metal that is deposited directly on the substrate sticks to the surface. Thus, the lift-off process leaves a film on the surface of the substrate with the same shape as the pattern on the photomask. Films that we pattern by lift-off have nearly vertical edges. We have found that transition-edge sensors with sharper edges have narrower transitions—and are more sensitive thermometers. Therefore, we often use lift-off to pattern our transition-edge sensors.

5.3.4 Ion milling

The thin-film deposition system has an ion gun in the main chamber, which is used to remove oxidization and etch the surfaces of samples. The ion gun is supplied with 10 mTorr of argon when operated. The ion gun creates an argon plasma, and it accelerates argon ions at the surface of the sample to be etched. The argon ions impact the sample, removing atoms from the surface. We often use the ion gun to remove oxidation from the surface of films that have become oxidized due to exposure to the atmosphere.

5.3.5 Thermal evaporation

In the early stages of our transition-edge sensor work, we used thermal evaporation with a shadow mask to fabricate devices. Our thermal evaporation system, consisted of a stainless-steel bell jar which could be pumped down to 5×10^{-7} Torr, a tungsten boat or wire used to heat metal to its boiling point, and a fixture which held the substrate and shadow mask about a quarter of a meter above the substrate. The source of metal is much smaller than a sputter target and is much further away. Therefore, thermal evaporation, when used in conjunction with a shadow mask, produces films with shaper edges than sputtering through a shadow mask does. (However, the lift-off process produces very well defined

films in either a sputter system or thermal evaporator). Others have produced very good transition-edge sensors using this thermal evaporation [2]. However, our group abandoned thermal evaporation in favor of our much better equipped and cleaner thin-film deposition system, because we were not able to sufficiently control the purity and thickness of our films in our old thermal evaporator.

5.4 Fabrication of our transition-edge sensor microcalorimeters

We have patterned transition-edge sensors in a number of ways in our lab. We have used sputtering, thermal evaporation, shadow mask, and lift-off. We have even patterned transition-edge sensors by cutting deposited films with a razor to get sharp edges. All of these methods have produced working transition-edge sensors. However, our most reproducible microcalorimeters were produced using a combination of sputtering, shadow mask, and lift-off. We will describe microcalorimeters fabricated in this way below.

We designed transition-edge sensor microcalorimeters for measurement of x rays based on the design criteria described in Chapter 3. The heat capacity is small. The thermal conductivity within the microcalorimeter is large. The microcalorimeter is decoupled from the bath. The phase transition is narrow. And, the devices have good absorption efficiency for photon in the 100 eV to 10 keV energy range.

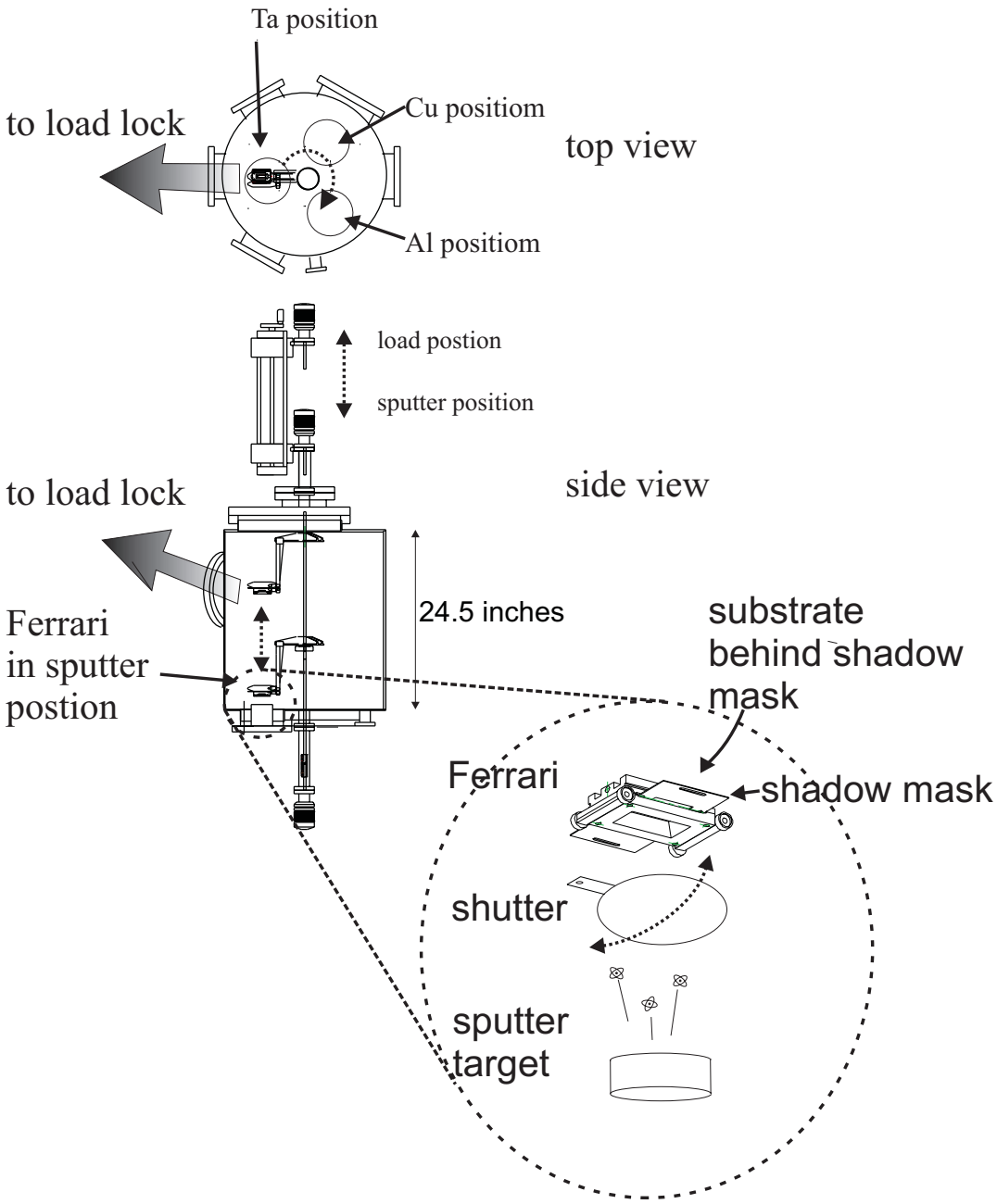

Figure 5.3. Sputtering in our thin-film deposition system. Samples may be placed in the Ferrari along with a shadow mask for pattering. The Ferrari is lowered into position above one of the sputter guns, and thin films are sputtered onto the substrate when the shutter is open.

The microcalorimeters are deposited on top of a membrane substrate which was described in the previous section. They consist of four metal layers: a copper absorber layer, an aluminum wiring layer, and a copper and aluminum bilayer that forms the transition-edge sensor.

5.4.1 The "Sunflower" shadow mask

The microcalorimeters are fabricated using the shadow mask pattern shown in Fig. 5.4. The shadow mask pattern, named "Sunflower", is designed so that four microcalorimeters are deposited on each of the three membranes of a one inch by one fourth in silicon substrate. The microcalorimeters are deposited symmetrically on each membrane in a pattern resembling a sunflower—hence the name of the pattern. The devices are deposited in a symmetrical pattern so that even if the mask is misaligned by 100 microns with respect to the position of the membranes, at least two of the microcalorimeters will be deposited on each membrane.

The mask has eight different positions, numbered 1 through 8 from left to right. Positions

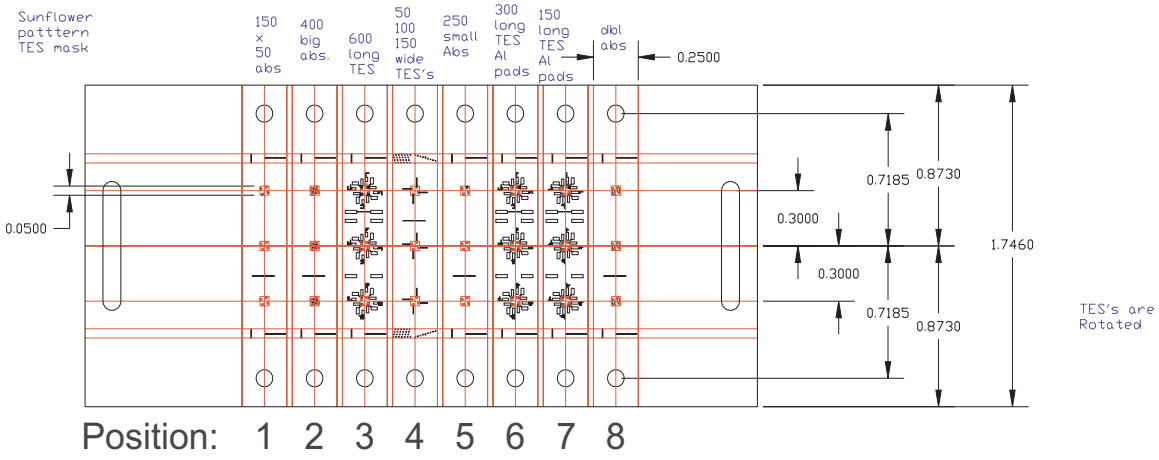

Figure 5.4. The mask used to pattern our devices. This mask is used for both sputtering and photolithography. The different patterns on the mask correspond to absorbers, TES thermometers, contact pads, labels for identification and alignment, and strips for measuring residual resistance ratios (RRR). The dimensions in the figure are given in inches.

1,2,5, and 8 have patterns for various shapes of absorbers. Position 4, is the mask position that is used to form transition-edge sensors. The rectangles in position 4 correspond to transition-edge sensors of widths of 50, 100, and 150 microns. The remaining mask positions are used in patterning the aluminum wiring layer, and they set the length of the transition-edge sensors. Transition-edge sensors of length 150, 300, or 600 microns are produced by using mask position 7,6, or 3, respectively, for the wiring layer. The choice of absorber mask and wiring layer mask determine the two dimensional shape of the microcalorimeters that are produced. The thickness of the films is controlled by the duration and power of the sputtering in the thin-film deposition system.

There are some additional features on the mask besides the wiring layer, absorber, and transition-edge sensor patterns. In the space between the microcalorimeters, long thin strips of metal are deposited along with pads for wire bonding. These are used to check the purity of the metal films that are deposited. An estimate of film purity is obtained from a measurement of the residual resistance ratio (RRR) of these films. Alignment marks also appear in the sides of the mask pattern. They are used to measure the alignment of the various layer with each other after fabrication. Next to each microcalorimeter's wire bonding pads, there are several small squares. The squares create labels that identify and number the microcalorimeters so that they can be easily distinguished from each other.

5.4.2 The fabrication of "Sunflower" microcalorimeters

The deposition process is outlined in Fig. 5.5 and Fig. 5.6. A $1'' \times 0.25''$ silicon substrate with silicon nitride membranes is cleaned, and then this sample is loaded into the Ferrari, with a shadow mask. The clean substrate is illustrated in Fig 5.5a and Fig 5.6a. The shadow mask is set so that position 5 lies over the substrate, which patterns absorbers of dimensions 250 $\times$ 250 microns, along with a resistance ratio strip. The load lock is pumped down, and the Ferrari is transferred to the main chamber in position above the copper sputter gun. Sputtering deposits four square copper absorbers on each membrane as

depicted in Fig. 5.6b. The Ferrari is then transferred back to the load lock, where the mask is transferred from the absorber position to a wiring position, while still under vacuum. Position 7 is often used to so that the transition-edge sensors will be 150 microns long. Next, the Ferrari is transferred back to the main chamber and positioned in place above the aluminum sputter gun. An aluminum wiring layer, 200 nm thick, is sputtered on to the surface, along with a resistance ratio strip, as illustrated in 5.5b and 5.6c. After the copper absorbers and the aluminum wiring layer are deposited, the Ferrari, shadow mask, and sample are transferred back to the load lock and removed from the thin-film deposition system. The sample and shadow mask are then removed from the Ferrari. The exposure to atmosphere causes thin oxide layers to form on the exposed surfaces of the aluminum and copper layers, as illustrated in Fig 5.5c.

The sample is then prepared for lift-off. Photoresist is spun onto the sample, which coats the surface of the substrate and the deposited films, as illustrated in 5.5d. After baking, the sample is placed back into the Ferrari, along with the shadow mask. The mask is set to position 4, which patterns the films used to make the transition-edge sensors. The shadow mask is used as a photomask for the lift-off process. The Ferrari is placed under an ultraviolet light for about a minute, which exposes the pattern of the transition-edge sensors into the photoresist. Then, the exposed pattern of photoresist is chemically removed in the developing process. This process leaves a pattern of photoresist on the surface of the substrate as shown in Fig. 5.5e.

The Ferrari and sample are placed back into the load lock of the thin-film deposition system, without the shadow mask. After pumping down the load lock, the sample is transferred into position above the ion gun. The sample is ion milled for one minute. The ion milling removes oxidation layers formed by exposure to atmosphere, but does not destroy the photoresist, as is illustrated in Fig, 5.5f. After the oxidation is removed from the surfaces where the film is to be deposited, the sample is placed in position above the copper

sputter gun. A copper film is sputtered onto the sample. Then the sample is transferred to the aluminum sputter gun, where an aluminum film is deposited. The aluminum-copper bilayer film that was deposited forms the transition-edge sensor. The ratio of the thicknesses of the two films determines the critical temperature of the phase transition, due to the proximity effect between the aluminum which has a critical temperature of $T_c = 1.2$ K and copper which a normal metal. A plot of phase transition temperature of bilayer films with various thickness of aluminum and copper is shown Fig. 5.7. The data for this plot were measure by Daniel Chow, Harrie Netel, and myself. The plot is reproduced from the Ph.D. thesis of Harrie Netel [1]. The thickness of the films composing one of our TES microcalorimeters is described in Section 7.2.

The sample is removed from the thin-film deposition system and placed in acetone for lift-off to begin. The photoresist dissolves in the acetone. The bilayer that was deposited upon of the photoresist lifts off, leaving the films that form the transition-edge sensors behind, and the fabrication process is completed.

The fabrication process results in twelve transition-edge sensor microcalorimeters which typically have a critical temperature of 80 mk to 200 mk, depending on the ratio of copper to aluminum film thickness in the TES bilayer. These finished devices are shown in Fig.5.5h and Fig. 5.6d. At operating temperature (typically about 100 mK), the aluminum wiring layer superconducts, but the copper absorber is a normal metal. The parts of the bilayer that lie on top of the copper absorbers or the aluminum bonding pads are proximitized, so that they completely normal or superconducting. Only the parts of the bilayer that lie in between the absorbers and the bonding pads function as transition-edge sensors.

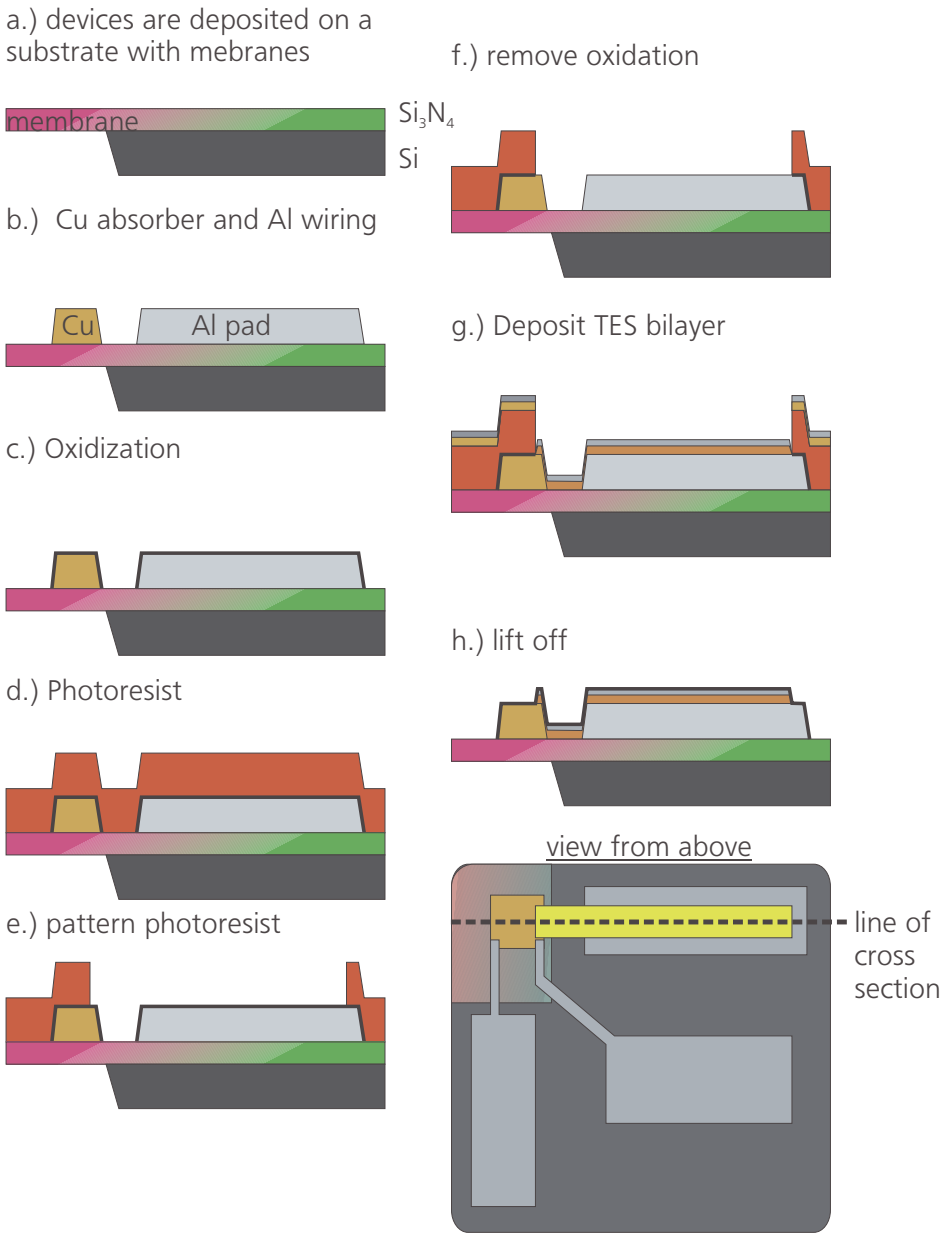

Figure 5.5. The fabrication of our TES microcalorimeters as shown in cross section. First, the absorber and bonding pads are sputtered on to the substrate in the thin-film deposition system, using a shadow mask for patterning (step a-c). Next, the sample is remove from the thin-film deposition system, and a pattern for the TES thermometers is placed on the surface using photolithography (steps d, e). The sample is then placed back into the thin-film deposition system for deposition of the TES thermometers (steps f, g). Finally, the photoresist is lifted off, leaving the thermometers on the substrate (step h).

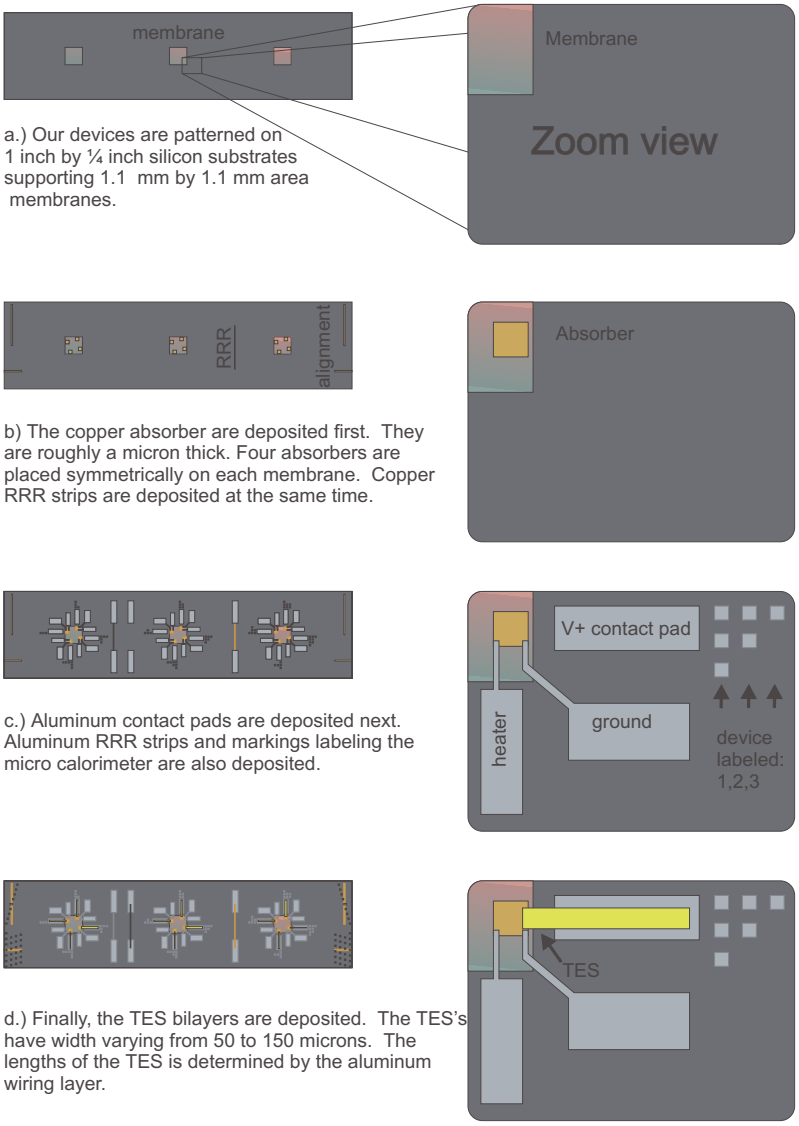

Figure 5.6. An illustration of the deposition of our superconducting transition-edge sensor microcalorimeters for detection of x-rays, as viewed from above. The mask pattern is called "Sunflower" because the calorimeters are distributed symmetrically around the membranes like pedals on a flower.

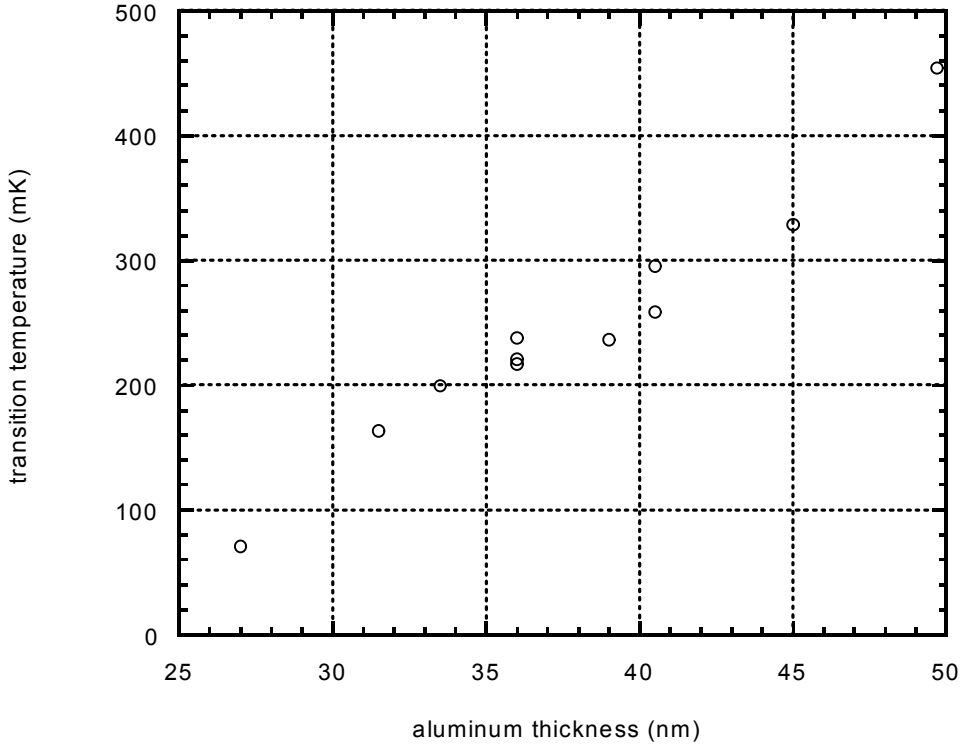

Figure 5.7. Measured transition temperatures of aluminum/copper bilayer films. The transition temperature is plotted as a function of the thickness of the aluminum layer. The thickness of the copper film is 83.0 nm minus the thickness of the aluminum film so that the total thickness of the bilayer film is kept constant.

[1] Harrie Netel, "Low Temperature Gamma-Ray Spectrometers Based on Bulk Superconducting And Dielectric Absorber Crystals," Ph.D. Thesis, University of Twente, 1999.

[2] K. D. Irwin, G. C. Hilton, J. M. Martinis *et al*., "A hot-electron microcalorimeter for X-ray detection using a transition edge sensor with electrothermal feedback," Nuclear Instruments & Methods in Physics Research, Section A Spectrometers, Detectors and Associated Equipment) **370** (1), 177-9 (1996).

Chapter 6

EXPERIMENTAL SETUP

6.1 Introduction to our experimental setup

A large part of the expertise of the cryogenic detector group at Lawrence Livermore National Laboratory pertains to the experimental study of low-temperature detectors. Such expertise is necessary because much of the technology required to run our experiments is not commercially available. Our group designs and constructs our own adiabatic demagnetization refrigerators. Additionally, we install and maintain the wiring, amplifiers, and thermometry in our refrigerators. Also, certain knowledge is required to work safely with technologies involving potential hazards such as cryogenic liquids and high voltage radiation sources. In this chapter, I will describe some of the technologies involved with the experimental study of low-temperature detectors.

6.2 Refrigeration

Our microcalorimeters are designed to be operated at very low temperatures—we typically operate them at a temperature near 0.1 K. Cryogens and adiabatic demagnetization refrigerators (ADR) are used to cool our samples down from room temperature to a fraction of a degree above absolute zero. These refrigerators are designed with great care to isolate inner cold parts of the refrigerator from the room temperature environment of the laboratory.

An illustration of our refrigerators, also called cryostats, is shown in Fig. 6.1. Our cryostats are vacuum bottles, consisting of four progressively colder stages: the room temperature stage, the liquid nitrogen stage, the liquid helium stage, and the ADR stage. The four stages are nested like Russian dolls so that each cold stage lies completely within the next coldest stage. The stages are thermally isolated from each other so that the thermal load on the colder stages is minimized. Low thermal conductivity structural supports hold each of the stages in place. When a cryostat in operation, the air is pumped out from the inside of a cryostat so that the inner pressure is less than 10^{-6} Torr. Thus, thermal isolation is provided by a single vacuum space that separates the stages as shown in the figure.

The room temperature stage, which is the warmest, outermost stage, is a cylindrical aluminum vacuum tight bottle that forms the outside surface of the cryostat. The nitrogen stage is a cylindrical aluminum shell suspended on thermally insulating standoffs within the vacuum space of the cryostat. Part of the nitrogen stage forms a reservoir that is filled with the liquid nitrogen. The nitrogen stage is cooled by liquid nitrogen in the nitrogen reservoir to 77 K. The liquid nitrogen provides continuous cooling power by boiling off into the atmosphere. The nitrogen reservoir has to be refilled about every 12 hours before the nitrogen runs out.

The helium stage and helium reservoir lie within the nitrogen stage. The helium stage is similarly cooled by liquid helium in the helium reservoir. However, at atmospheric pressure, liquid helium boils at 4.2 K—a temperature that is too warm for our ADR stage to work properly. We pump on the helium reservoir to lower the pressure within, which lowers the helium boiling temperature. By pumping on the helium reservoir we lower the temperature of the helium stage to about 2 K, which is a temperature cold enough to operate the ADR. The helium stage provides the 2 K enclosure in which our experiments are conducted.

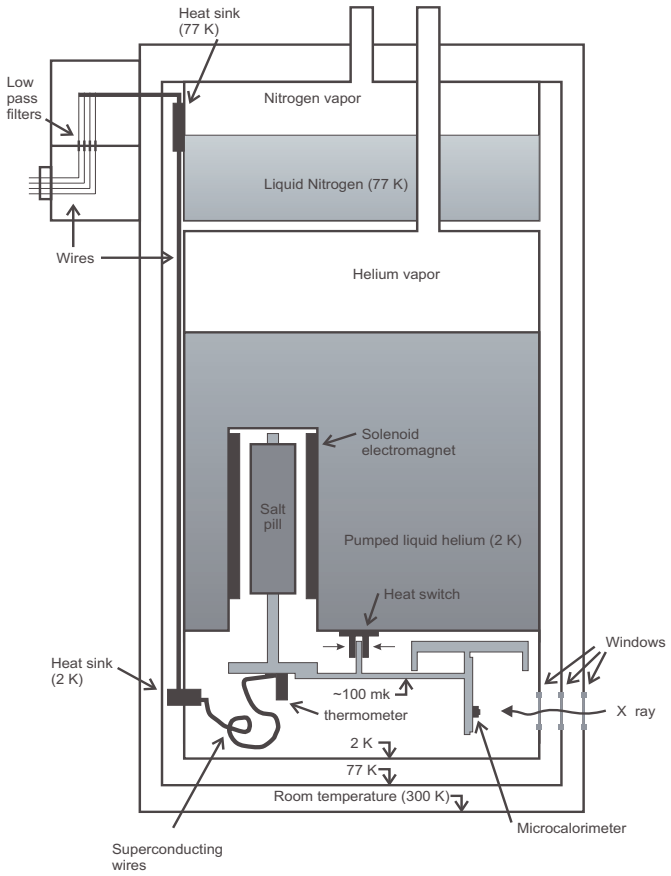

Figure 6.1. An illustration of one of our cryostats in position to conduct an experiment. In this configuration the detector is on the ADR stage in the bottom quarter of the cryostat. The ADR stage is typically regulated at a temperature between 50 and 200 mK. The ADR stage is suspended in the vacuum space enclosed by the 2K pumped helium stage, which is enclosed in the 77K liquid nitrogen stage. The outer most stage is a vacuum tight bottle, which is at room temperature. Wires running in from the outside of the cryostat to the ADR stage are heat sunk on the various stages to minimize thermal loading of the ADR.

The ADR stage is shown in Fig. 6.2. It consists of the crab, which is a receptacle for our microcalorimeters and other devices, a cold plate, which provides a surface to which thermometers and other experimental devices may be anchored, and a magnetic salt pill.

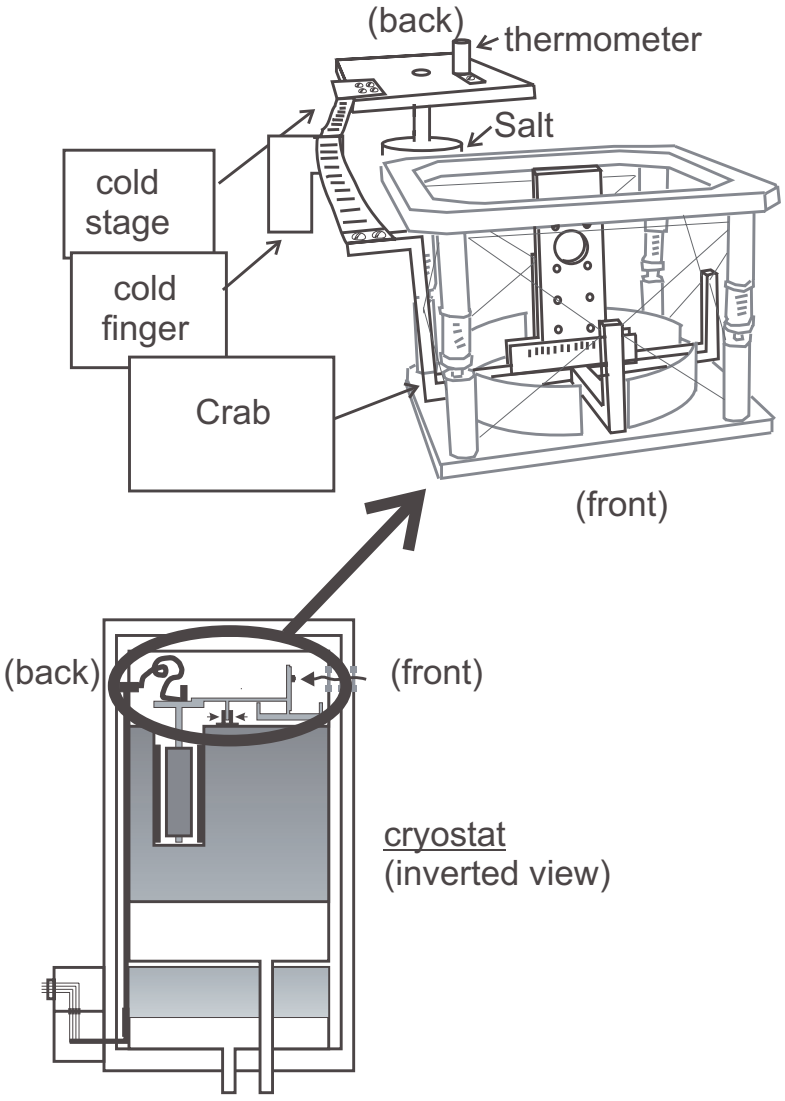

Figure 6.2. The Adiabatic Demagnetization Refrigerator (ADR) Stage. The whole ADR stage is suspended on kevlar strings in the vacuum space of the 2K stage so that it is thermally isolated. It comprises the crab, the cold finger, the cold stage, and the salt pill. The salt pill, which is not shown in the 3-D illustration, provides refrigeration. Microcalorimeters are mounted on the crab. Other devices, such as thermometers, can be mounted on the cold stage. The ADR stage is thermally connected to the heat switch through the cold finger, when the heat switch is closed.

The ADR stage is suspended on taught kevlar strings within the 2 K enclosure. The kevlar strings provide rigid structural support, but they conduct very little heat from the helium stage. The ADR stage and the 2 K stage can be thermally coupled and decoupled by the heat switch. When the heat switch is closed, the ADR stage is well coupled the helium stage. When the heat switch is open, the ADR stage is thermally isolated from the 2 K environment of the helium stage.

The ADR stage is cooled from 2 K down to temperatures as low 50 mK by the adiabatic demagnetization refrigerator (ADR). The ADR consists of a salt pill and a large magnet that work in conjunction with the heat switch and the helium reservoir to provide cooling to the ADR stage.

A crystal of hydrated paramagnetic salt, ferric ammonium alum (FAA), comprises most of the salt pill. When no external magnetic field B is applied to the salt, the magnetic spins of the iron atoms in the salt are randomized. When a magnetic field is applied to the salt pill, a fraction of the spins lines up with the magnetic field. The stronger the magnetic field, the greater the fraction of the spins that line up.

Before describing the refrigeration process, we shall describe the case in which the salt pill is thermally isolated from its environment. In this case, the application of a magnetic field to the salt is a reversible process in the salt: There is no change in entropy of the salt during this process (called magnetization). Application of the magnetic field orders the spins in the salt, producing a net decrease in the entropy of the spin orientations. The loss of entropy in the spin orientations is compensated by an increase in the entropy of the thermal modes of the salt so that there is no net entropy change. Therefore, the temperature of the salt increases when the magnetic field is applied. Conversely, when the magnet field is removed, the spins disorder and the temperature drops in the salt.

We exploit the properties of the magnetic salt to refrigerate our samples. The refrigeration process is as follows: Initially, the cold stage is thermally connected to the pumped helium reservoir by the closed heat switch. This cools the ADR stage to 2 K. Then, a 3 T magnetic field is applied to the salt by a large solenoid electromagnet. The magnetic field causes the spins to order and the temperature of the salt the increase to about 10 K. The salt is then warmer than the liquid helium, so heat flows from the salt pill to the helium through the closed heat switch. The heat flow lowers the entropy in the salt. The pumped helium dissipates the heat by boiling off quicker and cools the salt and the rest of the ADR stage back down to 2K in about 15 minutes. Once the salt is cool again, the heat switch is opened to decouple the cold bath from the helium reservoir. Then, the magnetic field is ramped down (called demagnetization). This causes the spins to disorder, and entropy is conserved by a corresponding drop in temperature. This process reduces the temperature of the salt pill and cold stage from 2 K down to about 50 mK. Thermal loading, which is dominated by heat conduction along wires that connect devices on the ADR stage to laboratory electronics, slowly warms the cold stage back up to 2 K. When the cryostat is working well, the cold stage remains below 100 mK for up to 12 hours.

We are careful to minimize both heat conduction and Joule heating in the wiring. Wires that originate at the room temperature stage are heat sunk at the nitrogen stage and the helium stage. Wires running from the helium stage to the cold stage must have high electrical conductivity but low thermal conductivity. Long, thin superconducting niobium-titanium wires (which are copper-nickle clad) or phosphor-bronze wires are typically used for this purpose because they have relatively low thermal conductivity but high electrical conductivity.

6.3 Mounting the detectors in the cryostat

Our microcalorimeters are mounted onto device holders that are screwed to the crab as shown in Fig. 6.3. In most measurements, a collimator is placed over the microcalorimeters. The collimator has a tiny holes in it above the absorbers of devices to be tested. A hole in the collimator allows x rays to pass through to be absorbed in an absorber. The TES's and the substrates are shielded from x-rays by the collimator.

The device holders have sixteen planar copper wires that can be wire bonded to the wire bonding pads of the microcalorimeters on the substrate. The copper wires are soldered to a connector that plugs into a receptacle on the crab. Some of the superconducting wires leading from the receptacle are connected to our dc SQUID amplifiers. Other wires are led through heat sinks to connectors on the outside of the cryostat, where they are connected to instruments as needed. These wires are used to bias and read out the detectors.

6.4 Temperature regulation

Thermometers are deployed in a cryostat to measure the temperature of various stages. The temperature of the ADR stage is measured using a germanium resistive thermometer (GRT) or a thin film ruthenium oxide thermometer. These thermometers are designed so that their electrical resistance increases rapidly with decreasing temperature. The resistance of these thermometers is read out by our AVS 47 resistance bridge sold by Oxford Instruments. The resistance bridge reads out the resistance through a four wire measurement: It applies a small current to the resistive thermometer through two wires, and it measures the potential difference via the other two. The sensitivity of the temperature measurement is limited by electronic noise in the thermometer. We typically obtain measurements as good several microkelvin.

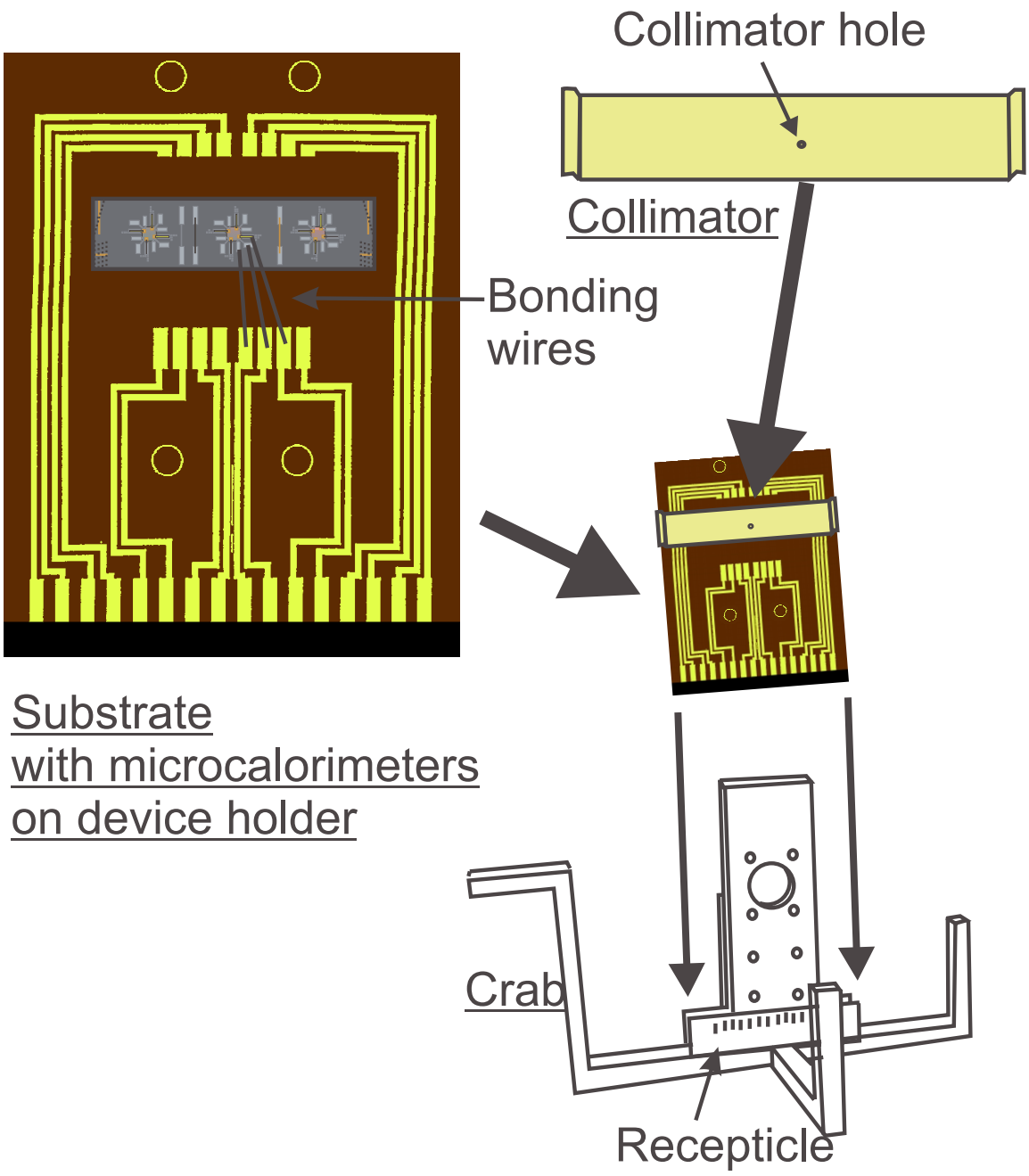

Figure. 6.3. Placement of microcalorimeters on the ADR stage. The substrate is adhered to a sample mount as shown. The aluminum leads of the detector to be measured are wire bonded to copper wires on the sample mount as indicated by black lines. (In this illustration, the TES bias lead, the ground wire, and the heater lead of one microcalorimeters are connected.) A collimator is placed over detectors so that incoming x rays are blocked except over the absorber of the microcalorimeter to be measured. The sample mount is plugged into the crab of the ADR stage. Wires leading from the receptacle on the crab connect the microcalorimeter to the SQUID amplifier and other electronics.

We assume that the fluctuations in the ADR temperature occur at very low frequencies because the C/G time of the ADR stage is much larger than the thermal time constant of the microcalorimeter. The first order effects of this noise on the microcalorimeter performance are negligible because most the signal from the microcalorimeter occurs at much higher frequencies. However, the second order effects of this noise are significant: Low-frequency variations in bath temperature can cause variations in the gain of the calorimeter.

If the gain of the microcalorimeter fluctuates significantly during a measurement, then the amplitudes of the pulses will vary, resulting in broader peaks in the spectrum and poorer energy resolution. The gain of the microcalorimeter is determined by the temperature T of the TES and the electric current I flowing through the TES. The temperature and current are in turn affected by the bath temperature T_{bath}, which is the temperature of the substrate. In normal operation, the temperature of the substrate equals the temperature of the ADR stage. Therefore, it is important to keep the temperature of the ADR stage as stable as possible to minimize fluctuations in the gain of the microcalorimeter. Our experience is that a stability of 5 μK to 10 μK is sufficient for our experiments.

Suppose that a microcalorimeter is used to measure x rays of energy E. In response to the absorption of x rays, the microcalorimeter produces electronic pulses with amplitude a. The amplitudes of the pulses vary by the amount Δa because the bath temperature T_{bath} varies by the amount ΔT_{bath} during the measurement. If the microcalorimeter is calibrated so that pulse amplitude is proportional to x-ray energy, then variations in pulse amplitude cause the energy measurements to vary by energy ΔE.

$$\Delta E = \frac{\Delta a}{a} E \tag{6.1}$$

The amplitude a depends on the power dissipated in the calorimeter. The power depends on the bath temperature. Therefore, we express variations of the pulse amplitude in terms of variations of the bath temperature:

$$\Delta a = \left| \frac{da}{dP_c} \Delta P_c \right| = \left| \frac{da}{dP_c} \right| \left| \frac{dP_{\mathrm{c}}}{dT_{\mathrm{bath}}} \right| \Delta T_{\mathrm{bath}}, \tag{6.2}$$

where the power P_{c} is described by equation (4.3), and ΔP_{c} is the amount the power varies due fluctuations in the bath temperature. From equation (4.3), we obtain

$$\left| \frac{dP_{\mathrm{c}}}{dT_{\mathrm{bath}}} \right| = P_{\mathrm{c}} \frac{N {T_{\mathrm{bath}}}^{N-1}}{T^N - {T_{\mathrm{bath}}}^N}, \tag{6.3}$$

where we have assumed that the microcalorimeter temperature T is held constant by electrothermal feedback. To estimate the effect of the temperature fluctuations, we assume that pulse amplitude is approximately proportional to power P_{c}:

$$\frac{da}{dP_{\mathrm{c}}} \cong \frac{a}{P_{\mathrm{c}}}. \tag{6.4}$$

Using equations (6.1), (6.2), (6.3), and (6.4), we find that

$$\Delta E \cong \frac{N {T_{\mathrm{bath}}}^{N-1}}{T^N - {T_{\mathrm{bath}}}^N} \Delta T_{\mathrm{bath}} E. \tag{6.5}$$

By using equation (6.5), we find that fluctuations in the ADR stage temperature of 5 μK will cause the measurements of 6 keV x rays to vary by approximately 1.5 eV, if N=1, T_{bath}=100 mK, and T_0=120 mK. (These values correspond to the calorimeter described in Chapter 7.)

After demagnetization, the temperature of the ADR stage slowly increases as heat leaks into the ADR stage from various sources, if the temperature is unregulated. (The primary source is usually heat leaking in along the wires that are used to read out devices on the ADR stage.) However, we can regulate the temperature at a constant value (such as 100 mK) by applying a magnetic field to the salt pill. In this approach, we read out the temperature of the ADR stage, as measured by the resistance bridge and a germanium thermometer mounted on the cold stage. If the temperature is below the set point, the magnetic field is increased, thereby warming the salt and the rest of the ADR stage. If the temperature is to high, the magnetic field is reduced. Temperature regulation is accomplished by a Linear Research LR-130 temperature controller. The LR-130 takes in the offset resistance from the set point as an analog voltage input from the resistance bridge. The input is filtered and converted to a voltage output by the LR-130. The voltage output is then converted to a current and sent through the ADR magnet, which applies the magnetic field to the salt pill. Using the LR-130 controller, we can achieve a temperature stability that is limited by the sensitivity to which the temperature can be measured (several microkelvin). The controller can regulate the temperature of the ADR stage on a time scale greater than or equal to the thermal time constant, C/G, of the whole ADR stage, which about 1 second at 100 mK.

An alternative means of temperature regulation has also been employed. This method involves mounting the detectors on a remote cold stage (RCS) which is heat sunk to the ADR stage, but relatively thermally decoupled. A heater (which is a heat sunk 500 kΩ resistor) is also mounted on the remote cold stage, along with a germanium thermometer. The temperature of the remote cold stage is read out and then fed back to the heater by the resistance bridge and the LR-130. The feed back can regulate the temperature of the RCS to a temperature greater than the temperature of the ADR stage. If the temperature of the RCS is below the set point, the current through the heater is increased and the temperature increases due to Joule heating. If the temperature is to high, the current through the heater is

reduced, and the RCS is cooled by heat leaking out to the colder ADR stage. Using the feedback, the temperature of the RCS is controlled to several microkelvin. The thermal response time is much faster than for the ADR stage because the heat capacity of the RCS is much less than the heat capacity of the ADR stage. The C/G time of the RCS is typically 0.1 microsecond.

6.5 Radiation sources

Obviously, sources of x-ray radiation are required to test our x-ray microcalorimeters. We sometimes mount an Fe^{55} radioactive source in our cryostat in front of our detectors to use as a source of x rays. The Fe^{55} radioactively decays into Mn^{55} by electron capture. The newly created Mn^{55} atoms have vacancies in their K electron orbitals. About 85% of the time, Mn Kα (5895 eV) photons are emitted when electrons drop into these vacancies, and Mn Kβ (6490 eV) photons are emitted 15% of the time. The strength and location of the source are chosen so that there are a few absorption events per second in the absorber.

We often use a Henke tube x-ray source. In this electronic source, electrons are accelerated in vacuum across a electric potential of several kilovolts into a target. The target emits emitting x rays through bremsstrahlung and florescence. Many of these x rays are absorbed by a second target, which also fluoresces. Some of the x-rays emitted from the second target pass through the windows into the cryostat, where they irradiate the detector. The Henke tube source is designed so that the experimenter can easily switch between secondary targets. Each secondary target emits a characteristic spectrum of x-ray lines, depending on its elemental composition. For instance, a manganese target emits Mn Kα and Mn Kβ lines. The experimenter can turn off and on the various emission lines by switching between secondary targets made of different elements.

6.6 Detector electronics

6.6.1 The SQUID system

We require large-bandwidth low-noise amplifiers to read out our TES microcalorimeters. Low noise is required in order to obtain the best possible energy resolution: Ideally, the energy resolution of a microcalorimeter is limited by intrinsic noise in the microcalorimeter such as phonon and voltage noise, not by amplifier noise. Large bandwidth is required for two reasons. First, the bandwidth of the electronic amplifier should exceed the bandwidth of the microcalorimeter so all the frequency components of the signal are measured. Second, it is essential to have fast amplifiers in order to accurately measure the shapes of the pulses. The rise of the pulse, which is typically microseconds, is used by the electronics to trigger the measurement of a pulse. Triggering is more accurate if the amplifiers have very wide bandwidth. Also, the rise and decay of the pulse contain information about how long it takes the energy of the pulse to be thermalized in the TES and leak out to the cold bath. Furthermore, irregularly shaped pulses can offer clues as problems with the design of a microcalorimeter.

We primarily use Hypress dc SQUID arrays to read out the current I that is conducted though our TES's. These arrays are sensitive, low noise current amplifiers with large bandwidth. The noise is typically $2\ \mathrm{pA}/\sqrt{\mathrm{Hz}}$, except at low frequencies where there is significant $1/f$ noise. The bandwidth of the SQUID amplifiers, $2.5\ \mathrm{MHz}$, is larger than the bandwidth of our microcalorimeters. These amplifiers are sufficiently fast to accurately measure the shapes of our pulses.

A SQUID current amplifier from Hypress consists of a dc SQUID array, a device input inductance coil, and a feedback inductance coil all mounted on a single chip. An array of SQUIDs is used rather than just one SQUID because the array, which has much larger impedance, is better impedance matched to standard FET-based amplifiers used for readout.

(This allows the SQUID array signal to be measured directly by a measurement of voltage across the array, without bandwidth limiting a.c. modulation typically used in single element DC SQUID electronics.) The input and feedback coils overlap the SQUID array, so that electric current flowing through the coils creates a magnetic flux that passes through the SQUID loops. The voltage across the SQUID array is a periodic function of the magnetic flux through the SQUID array. The magnetic flux from input of feedback coil is proportional to the current through the coil. Therefore the SQUID array provides a measurement of the electric current through the coils.

The response of the SQUID array to current through the input inductance coil is nonlinear. The output of the SQUID system can be made linear by operating it in flux locked loop mode as illustrated in Fig. 6.4. In this mode, an amplifier couples the output of the SQUID back into current through the feedback coil, providing negative feedback. Any changes in current I through the input coil result in opposing changes in feedback current I_{FB} through the feedback coil. The SQUID is flux locked because the magnet flux through the SQUID is held constant by negative feedback. In this scheme, the feedback voltage V_{FB} is proportional to the device current I. The feedback voltage V_{FB} is filtered and measured by our laboratory electronics.

A schematic of a single Hypress SQUID readout channel is shown in Fig. 6.4. In this system, the detector is biased by a regulated voltage V_{b} outside the cryostat. This voltage causes a bias current I_b to flow through the bias circuit. If the TES thermometer $R(I,T)$ has a higher electrical resistance than the shunt resistor R_{s}, then most of the current I_b flows through the shunt. In this case, the bias circuit biases the thermometer with a voltage $V_0 \cong V_{\mathrm{b}} R_{\mathrm{s}} / (R_{\mathrm{b}} + R_f)$. The combination of bias resistor R_b and shunt resistor R_s are chosen so that a bias voltage V_b of a few volts produces a voltage across the thermometer

V_0 of a few microvolts. The combination of the resistor R_f and the capacitor C_f, which are located on the helium stage, function as an RC filter that filters out high frequency noise coming in on the bias line.

The input inductance coil L of the SQUID lies in series with the TES thermometer. When a voltage V_b is applied to the bias circuit, a current I is conducted through the thermometer $R(I,T)$ and the SQUID input coil. The SQUID measures the current flowing through the SQUID input coil. Note that there is also some additional inductance associated with the wiring of the loop containing the shunt resistor R_s, the thermometer $R(I,T)$, and the inductance coil. This additional inductance can be included into L when modeling the circuit. In modeling the response of the microcalorimeter, the circuit is simplified to a

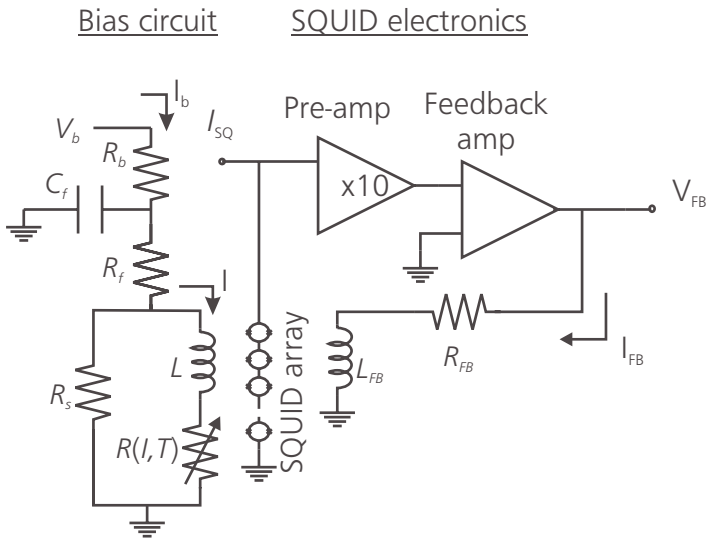

Figure 6.4. A schematic of a SQUID readout circuit. Electrical current *I* that flows through the TES, *R*(*I*,*T*), also flows through the SQUID input coil *L*. The coil *L* generates a magnetic flux through the dc SQUID array that is proportional to the current *I*. When the SQUID is properly biased with current I_{SQ} at low temperature (below the critical temperature of the niobium SQUID arrays), the voltage across the SQUID array is a periodic function of the magnetic flux penetrating the SQUID array. The feedback electronics apply a current I_{FB} through the feedback coil so that magnetic flux from L_{FB} exactly cancels the flux from the input coil *L*. Thus, the flux in the SQUID array is "locked" to a constant value, and the feedback voltage V_{FB} is proportional to the current *I*. An absorption event in the calorimeter causes a pulse in the current *I* and a pulse in the feedback voltage V_{FB}. Feedback voltage pulses are filtered and recorded by our laboratory electronics.

Thevenin equivalent, as shown in Fig. 4.2. In this model, the inductance and capacitance associated with wires and filters that bring the current I_b into the bias loop are neglected. This is a reasonable approximation because I_b is assumed to be slowly varying or approximately constant during a measurement.

The speed of the electronic circuit is approximately described by the time constant $L/(R_s + R_0)$, where R_0 is the equilibrium resistance of the thermometer. The actual electronic time is in not exactly given by this expression because the resistance $R(I,T)$ of the thermometer changes with current I. The effect of current dependent resistance on the electronic time constant were described Section 4.4.

The actual layout of a SQUID system installed into one of our cryostats is shown in FIG. 6.5. The system contains four Hypress SQUID channels. Each SQUID array and associated inductance coil is located on chip a that is sealed in a niobium tube. The tubes superconduct at temperatures below 9.5 K. When superconducting, they expel magnetic flux, thereby insulating the SQUIDs from magnetic noise. Wires connect the inductance coil, the shunt resistor, and a TES thermometer to form the bias loop, as in Fig. 6.4 These wires are shielded in superconducting capillaries made from lead-tin soldiering wire.

6.6.2 Grounding and shielding

The energy resolution that is obtained from a calorimeter can be adversely affected by noise from electronic pickup. This radio frequency noise originates from a.c. power supplies and instruments in the laboratory, computers, monitors, broadcast radio stations, and other sources. Pickup causes noise by inducing spurious voltages and currents in the detectors and other electronics, especially in long wires which act like antennas.

Electrically conductive shielding is a good defense against radio pickup. The conductive metallic cryostat reflects radio-frequency electromagnetic waves, thereby shielding the electronics within. However, radio frequency noise can be brought into the cryostat along wires and in gaps where the cryostat is sealed by nonconductive elements such as rubber o-rings or windows. Cables running between laboratory instruments and the cryostat are also shielded to minimize pickup. Many of the wires leading into the cryostat are low pass filtered to exclude pickup frequencies higher than a kilohertz. However, lines that carry out

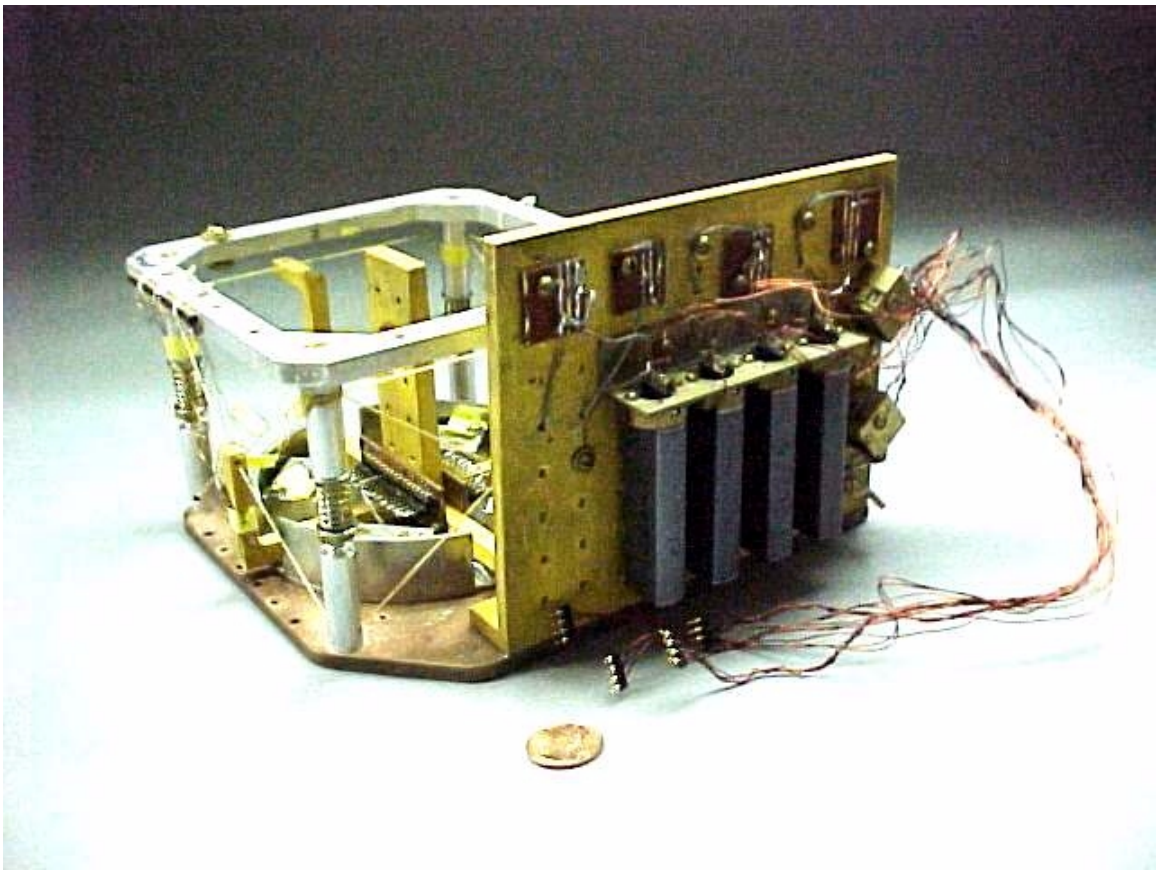

Figure 6.5. The layout of a four channel SQUID system using Hypress SQUID arrays. The SQUID arrays are located on silicon chips in the four dark colored niobium tubes that shied the SQUIDs from stray magnetic fields. The tubes are mounted on a copper plate next to the crab. The whole system is screwed to the 2K helium stage of our cryostat. Each SQUID is connected to a shunt resistor and to a receptacle on the crab (which plugs into the sample mounts that hold our microcalorimeters) by wires that superconduct at low temperature. The SQUID system is plugged into signal and bias lines leading out of the cryostat via copper wires shown on the right.

signals from the microcalorimeters can not be heavily filtered, or else much of the signal would be filtered out. For further protection against radio waves, the cryostat and much of the laboratory electronics are located in a Faraday cage, which is a well grounded metal room that can be tightly sealed shut to radio emissions. Digital electronics and monitors are kept outside the Faraday cage for the most part, because they tend to generate a lot radio-frequency noise. Electric cables leading into the Faraday cage from the outside laboratory are filtered at feedthroughs in the cage to minimize noise.

Detectors and various amplifiers are powered by batteries, rather than by commercial voltage sources that use a.c. power supply from a wall socket. We do this because such sources often have significant ripple, and because power cords plugged into the a.c. power grid radiate radio frequency noise into the Faraday cage.

Careful consideration of the grounding of laboratory instruments is required to minimize radio-frequency pickup. Ideally, all laboratory instruments should be grounded at one point on the Faraday cage to minimize pickup. Instruments should not be multiply grounded because multiple paths to ground create ground loops—ground loops provide low resistance paths that allow large currents to flow in response electromagnetic fields, thereby causing more pickup. When measuring energy spectra, I configured the grounding of our instrumentation as is illustrated in Fig. 6.6. In that configuration, all the electronics inside and outside the Faraday cage were grounded to one point on the cage. The central grounding point is a feed through on the cage that connects the BNC signal cable from the cryostat inside the cage to a BNC cable leading to the digitizer outside the cage. Many of the instruments are powered by the a.c. power grid, but their ground lines have been disconnected from the ground lines in the wall sockets. None of the instruments are allowed to touch grounded parts of the Faraday cage. Grounding is provided by the shielded cables that interconnect the instruments. Note that extreme care must be taken when running an experiment in this configuration. Ground wires can not be safely

disconnected when the instruments are plugged into the a.c. power grid unless an alternate path to ground is provided. Electronics such as the computer monitor must be properly grounded to avoid risk of electrical shock.

As previously stated, Fig. 6.6 illustrates the grounding scheme employed when spectra are measured. However, we often take other kind of measurements, such as IV curves and resistance versus temperature curves of TES's. In those measurements, several signal cables run to the digitizer from inside the cage. The additional lines are required measure quantities such as temperature or bias voltage. The additional connections form ground loops. However, these kinds of measurements are less sensitive to noise than is the acquisition of energy spectra from TES microcalorimeters.

Varying magnetic fields can also generate pickup. The SQUID system and our superconducting devices are enclosed in magnetic shields that block or expel magnetic fields. The ADR magnet is surrounded by a magnetic shield to contain magnetic fields

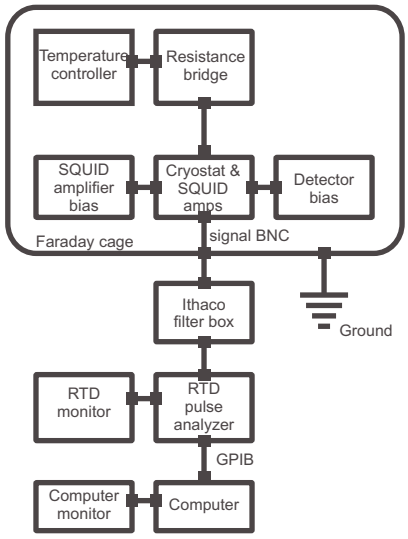

Figure 6.6. A schematic of the grounding scheme used when spectra are recorded from one of our microcalorimeters. In this scheme, all the instruments are grounded to a feedthrough on the Faraday cage. The system is set up so to avoid ground loops because ground loops contribute to electrical pickup. Note that care must be taken to ensure that all instruments remain well grounded when connected to the a.c. power grid, or else there will be an electrical shock hazard.

from the magnet.

6.7 Filtering and data acquisition

The feedback voltage V_{FB} is sent to an Ithaco 4302 broad-band amplifier. The Ithaco amplifier can be set to low-pass filter and high-pass filter the signal over a range of frequencies between 1 Hz and 1 MHz. The Ithaco amplifier can also be set to apply a gain factor of either 1, 10, or 100. The output of the filter box is sent to a Sony Tektronix RTD 710 digitizer. This instrument digitizes the signal, and sends it to the computer by way of GPIB. Lab View software on the computer displays the data on the computer monitor and then stores this the data on hard drive.

The digitizer samples the signal and noise at constant time intervals. Noise at frequencies higher than the sample frequency, appears at low frequencies due to digital aliasing. The analog signal must be low-pass filtered at half the sample frequency (called the Nyquist frequency) to exclude this high frequency noise. The anti-alias filter smoothes out data over time scales less than the sampling time. When anti-alliased, each sample is an average value of the signal plus noise during that sample interval. Therefore, anti-aliasing improves the signal to noise of a measurement. In practice, the signal is often low-pass filtered at a frequency lower than the Nyquist frequency to cut out those frequencies at which there is little signal compared to the noise.

6.8 Data analysis software

As previously described, the signal and noise are recorded on a computer hard disk drive by Lab View programs. The data stored on the computer can take many forms: measurements of current versus voltage characteristics of a TES, resistance versus temperature curves of a TES, measurements of pulses from TES microcalorimeters, noise measurements, etc. There

is a Lab View computer program specifically written to record and display each of these each of these kinds of measurements. (Most of the Lab View software was written by Carl Mears and Larry Hiller, with some small changes made by myself and others). After this data is stored on the computer's hard drive, it is later analyzed by the experimenters, using other software.

The major data analysis tool that we use in our Laboratory is a program called "Filter Pulses". Figure 6.7 illustrates the program's graphical interface. The program was written in Interactive Data Language (IDL). Most of the code was written by me, but significant parts were written by Carl Mears. The main purposes of the filter pulses are to digitally filter recorded pulses from energy-dispersive detectors and to calculate energy resolution. This involves digitally filtering out frequencies in which there is low signal to noise and involves discriminating between various kinds of pulses based on the there pulse shapes.

The digital acquisition of a spectrum of one of our TES microcalorimeters proceeds as follows: When an energetic particle is absorbed in the absorber, the microcalorimeter responds by generating a pulse in current. The current pulse is measured by the SQUID system, which sends a proportional voltage feedback pulse to the digitizer via the filter box. The rise of each pulse triggers the digitizer to record the pulse digitally and send it to the computer. Each pulse is digitally sampled 1024 times. Typically the digitizer is set to store 256 samples before the trigger event and 768 samples from the time of the trigger and after. The sampling time interval is set so that data from the rise and the decay of the pulse are recorded, as well as some the pretrigger data. Typically, thousands of such pulses are recorded in a file for each spectrum that is measured. Information about the sample rate and the voltage scale of the digitizer are recorded along with the pulses.

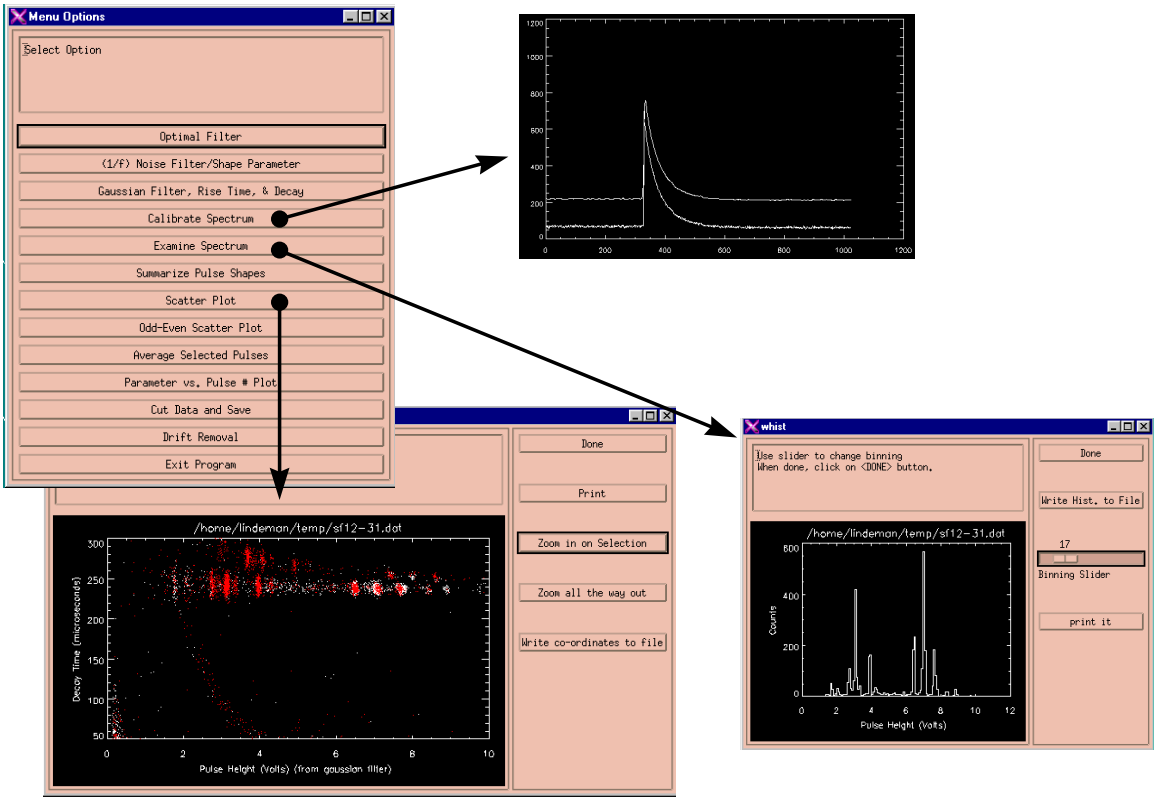

Figure 6.7. The "Filter Pulses" program. This program, which was mostly developed by myself, is used to filter digitized pulses from energy-dispersive detectors. The program can plot measurements of rise time decay time, pulse height or other parameters. The program is used to discriminate between different kinds of pulses based these parameters. The pulses can be filtered using a Gaussian filter, the computed optimal filter (based on the measured noise), or other filters. Measurements of the pulses can be plotted in a number of ways including scatter plots and histograms. The measured energy spectrum is obtained from a histogram of pulse heights. Peaks in such a histogram can be calibrated and fitted to obtain a measurement of energy resolution.

After the pulses are recorded, the program "Filter Pulses" is used to analyze the data. In the initial digital filtering step, "Filter Pulses" prompts the user to select a method of preliminarily filtering the data. Typically the user instructs the program to measure the height of the pulses after they are smoothed by convolution them with a Gaussian curve. The convolution is a digital low-pass filter that is used to smooth out digitization effects and high frequency noise. The rise times and decay times of the pulses, and other measures of pulse shape are also calculated in this step. The calculated pulse heights, decay times, rise

times, and other parameters are stored in arrays. The original data is left unaltered on the disk drive.

At this stage, pulse height can be plotted against rise or decay time or other measurements that discriminated shape. The resulting scatter plots are used to discriminate different kinds of pulses from each another. For example, Fig. 6.7 and Fig. 7.9 shows a scatter plot of pulse height versus decay time. In the figure there are several clusters of pulses. The various kinds of pulses come from different kinds of events in the microcalorimeter. The decay times of pulses vary with the location in which the absorption event occurs. For instance, absorption events in the substrate below a TES microcalorimeter may create pulses with a shorter decay time than absorption events in the absorber. This information can be used to exclude or separate pulses from events outside the absorber.

The program allows the user to select those pulses in the scatter plot that correspond to absorption events in the absorber. I call selection of pulses on the scatter plot "gerrymandering" to remind users not to do this in a way that biases the data. (Gerrymandering is the name of a scheme in which voting districts are drawn unfairly to bias elections.).

The heights of selected pulses can be plotted in a histogram, by selecting various spectrum-plotting options in the program. The binning of the histogram plot can be chosen by the user. (Note that the choice of binning can bias the data if there are too few pulses measured, or if there are too few histogram bins.) The peaks in the histogram correspond to absorption events of different energies. The histogram can be calibrated into units of energy. The peaks in the histogram can be fit to Gaussian or Lorenzian shaped functions, and the FWHM energy resolution is obtained from the fit.

After the initial filtering of data, the user can choose to optimally filter the data. The optimal filter is described in Appendix B. The experimenter must record digitized noise samples as well as digitized pulses for the program to compute the optimal filter. In the standard algorithm, noise samples must be recorded at the same sample rate as the pulse, and the noise sample should not have any pulses in them. For optimal filtering the user is prompted to select out any noise samples that contain pulses. The user is also prompted to select a set of pulses that represent the typical pulse shape to be measured. Using this information, the program computes the optimal filter. When the optimal filter is convolved with a pulse, it measures the pulse height, and it weights those frequencies with higher signal-to-noise ratio more heavily than those frequencies with poor signal-to-noise ratio. The heights of pulses as calculated by the optimal filter can be histogrammed and plotted as before. Usually, we obtain our best energy resolutions from our energy dispersive detectors by using the optimal filter.

Note that the optimal filter only works well if all the pulses have the same shape. Also note that non-random noise, such as 60 Hz pickup from the a.c. power grid, is not best filtered by the optimal filter algorithm because the optimal filter algorithm assumes that the noise has a random phase. Periodic noise can be filtered out much better by just subtracting it out of the data (which is called coherent subtraction).

Chapter 7

EXPERIMENTAL RESULTS

7.1 Introduction to results

Besides modeling, design, and fabrication of microcalorimeters, my research with the LLNL cryogenic detector group involved considerable experimental work with these detectors. I developed an experimental method for characterizing TES microcalorimeters based on the theory of Chapter 4. A part of my experimental work, I assisted fellow graduate students Harrie Netel and Daniel Chow with the characterization, measurement, and analysis of their TES gamma-ray detectors. However, most of my research related to the development of various TES-based microcalorimeters for the measurement of x rays. In this chapter, the discussion is focused the experimental results obtained from x-ray calorimeters fabricated using the "Sunflower" shadow mask as described in Chapter 5.

7.2 The "Sunflower 12-1.2.3" microcalorimeter experiment

Up to the date of the this writing, the highest quality microcalorimeter fabricated in our laboratory is the device called Sunflower 12-1.2.3. The finished device is illustrated in Fig. 7.1. The device was fabricated using the "Sunflower" shadow mask, sputtering, and liftoff as described in Section 6.4.2. The TES consists of a bilayer of 55 nm of copper and 35 nm of aluminum. Our measurements indicate that this ratio of film thicknesses consistently produces TES thermometers with transition temperatures between 110 mK and 130 mK. The absorber of the microcalorimeter consists of a 250 μm $\times$250 μm $\times$3 μm

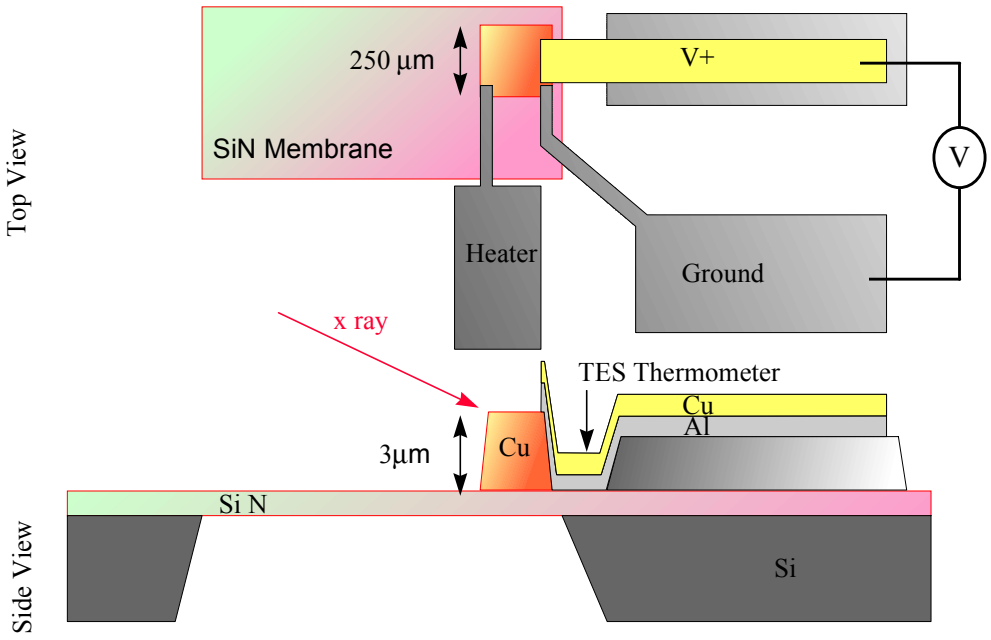

Figure 7.1 The layout of the microcalorimeter, Sunflower 12.1.2.3. The aluminum contact pads, labeled "V+", "Heater", and "Ground", are also shown. The device is shown as seen from above and from the side. The microcalorimeter lies moistly on the 0.5 µm thick membrane, which decouples the microcalorimeter temperature from the substrate temperature. The copper absorber, which dominates the volume and heat capacity of the microcalorimeter, has dimensions 250 µm by 250 µm by 3 µm. The TES formed by a bilayer of 55 nm of copper and 35 nm aluminum in between the absorber and the "V+" wire bonding pad. In operation, an approximate voltage bias is applied across the "V+" and "Ground" leads as illustrated. The electric current conducted through the TES is measured by a SQUID amplifier as described in Chapter 7. An electric current can be sent through the heater lead to ground that warms the microcalorimeter through Joule heating in the absorber. The device is designed to measure changes in temperature due to the absorber of individual x rays in the absorber. Temperature changes from the heater current and x rays are measured by the TES thermometer.

copper film. This film absorbs approximately 30% of 6keV x rays passing through it The device was mounted in one of our cryostats as described in Section 6.3. The ADR was used to cool to roughly 100 mK as described in Section 6.2.

7.2.1 Details of the measurement

The microcalorimeter was measured using a Hypress SQUID as described in Section 6.7.1 It was biased using a bias circuit as shown in Fig. 4.2, with the shunt resistance R_s=20 mΩ. The resistance of the TES and the shunt resistance lie in series with resistance due parasitic

resistances associated with wire bonds and soldier joints that connect the TES thermometer to the SQUID amplifier. These parasitic resistances R_p totaled 14 mΩ in this experiment. The shunt resistor plus the parasitic resistance combine to form a Thevenin equivalent resistance of R_{th}=34 mΩ. When the TES had a resistance much greater than R_{th}, it was approximately voltage biased.

At an operating temperature of 120 mK, the microcalorimeter has a heat capacity of C_0=2.2 pJ/K, which implies that the absorption of a 6 keV x ray will raise the temperature of the microcalorimeter by 0.44 mK.

7.2.2 Measurement of resistance versus microcalorimeter temperature

The first measurement made of the device was the measurement of resistance versus device temperature. The resulting data are shown if Fig. 7.2. A small bias, V_{th}=20 nV, was applied. At this low bias, the device temperature was approximately equal to the temperature of the ADR stage. The resistance of the TES lies in series with resistance due parasitic resistances associated with wire bonds and soldier joints that connect the TES thermometer to the SQUID amplifier. These resistances total 14 mΩ. As shown in Fig. 7.2, the measured resistance increases from the 14 mΩ value due to parasitic resistance, when the TES is superconducting, to about 225 mΩ, when most of the TES in the normal metal state. The steep part of the phase transition was about 0.25 mK wide. During the resistance versus temperature measurement, the current through the device was 1.0 μA when the TES was superconducting. The current decreased with increasing resistance to 82 nA when the resistance was 225 mΩ. The parameter $\alpha = (T_0 / R_0)dR/dT$ is 540 when the resistance is 100 mΩ. The critical temperature of this TES is T_c=121 mK. In summary, the measurement of resistance versus temperature indicated that the TES had a phase transition at the intended temperature, and that the phase transition was narrow enough to allow the

TES to function as a sensitive thermometer. The measurement of resistance versus temperature is described in more detail in Appendix A.

7.2.3 Measurement of current versus bias voltage characteristics

Current through the TES is measured as a function of Thevenin equivalent bias voltage V_{th}. These current versus voltage characteristics of the microcalorimeter are each measured with the bath temperature (the temperature of the ADR stage) regulated to a constant

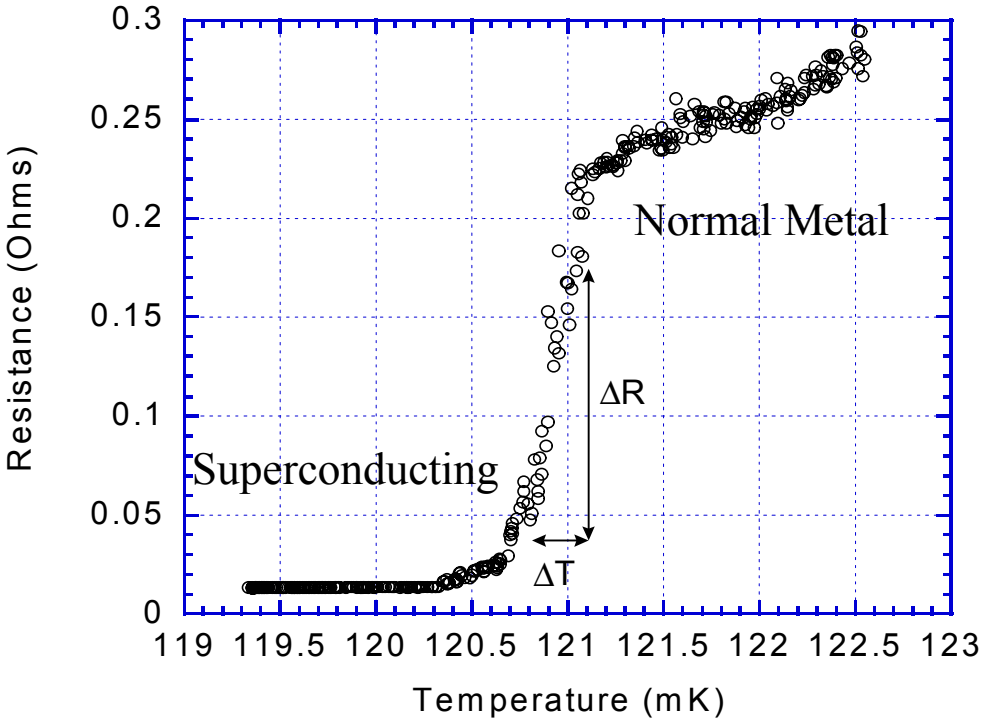

Figure 7.2. The measured resistance versus temperature of the TES thermometer of the microcalorimeter "Sunflower 12-1.2.3." The measurement was made using the bias circuit of Fig. 4.2. with V_{th}=20 nV and R_{th}=20 mΩ. The current through the TES was less than 1 μA when the TES was on the phase transition.

temperature. The characteristics were measured for a sequence of different bath temperatures. The measurement of such a sequence of characteristics provides information about resistance, gain, thermal coupling, power dissipated, and electrothermal feedback in TES thermometers for a range of bath temperatures and bias voltages. (The measurement of current versus temperature characteristics is described in greater detail in Appendix A.)

A plot of current versus voltage characteristics of Sunflower 12-1.2.3 is shown in Fig. 7.3. For the characteristics shown in Fig. 7.3, the ADR temperature is less than the critical temperature. In these measurements, the temperature of the microcalorimeter is sufficiently low to allow the TES to superconduct at low bias. Electrothermal feedback in the microcalorimeter causes the dynamic resistance of the TES to be negative in the transition.

We compute the equilibrium voltage V_0 across the TES from the measurements of the current I and the bias voltage V_{th}. In Fig. 7.4, we plot the current I conducted through the TES as a function voltage V_0 across it. Contours of power dissipated in the microcalorimeter and contours of resistance are also plotted in Fig. 7.4. In this plot, the superconducting branch is vertical. In the phase transition, electrothermal feedback causes the microcalorimeter to regulate its temperature T to approximately 120 mK (as will be explained below). In the 100 mK I-V characteristic, self regulation causes the power dissipated in the microcalorimeter to be nearly constant as a function of voltage. (The power changes a small amount because the finite width of the phase transition in temperature allows the power to vary.)

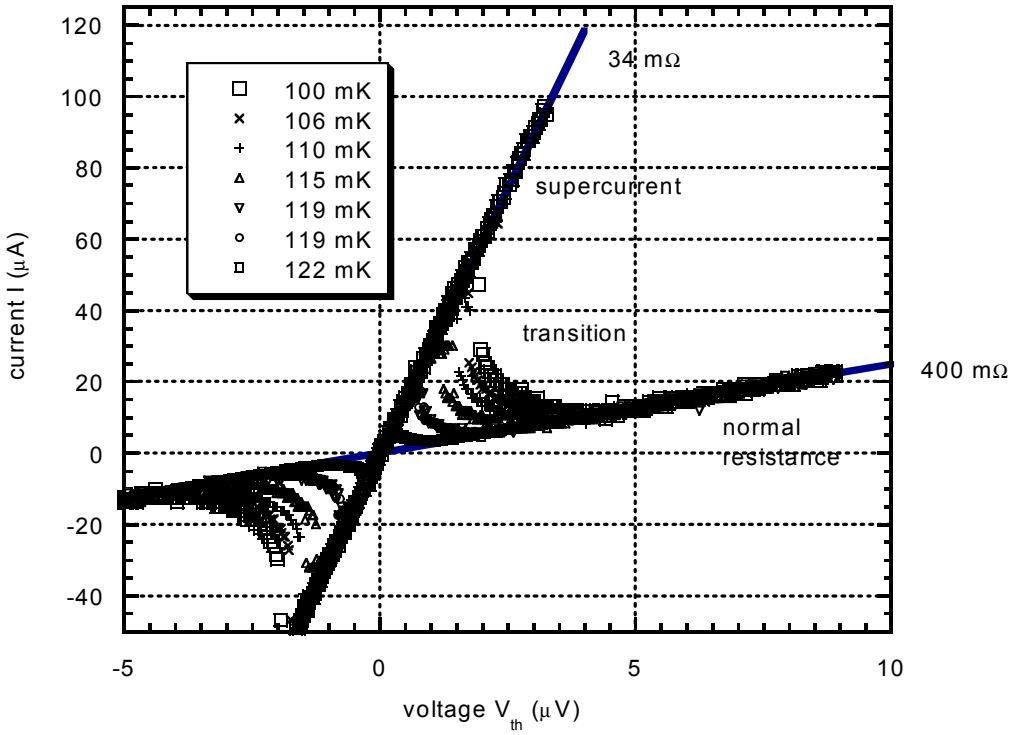

Figure 7.3 A family of I-V characteristics. Each I-V characteristic is a plot of the current I through the TES versus the Thevenin equivalent bias voltage V_{th}. Contours of resistance (including thermometer resistance $R(I,T)$ plus parasitic resistance) are also plotted. The data were measured with a bias circuit equivalent to the one of Fig. 4.2. The shunt resistance was R_s=20 mΩ. There was an additional 14 mΩ of parasitic resistance in series with the TES due to wire contacts. The total Thevenin equivalent resistance due to the shunt resistor and parasitic resistance was R_{th}=34 mΩ. The branches of the curves that are strait lines correspond to regions of constant TES resistance. The supercurrent branch has a resistance of 34 mΩ due to the Thevenin series resistance R_{th}. The normal resistance R_N is 400 mΩ. The I-V characteristics were measured at a series of bath temperatures, which are indicated in the figure.

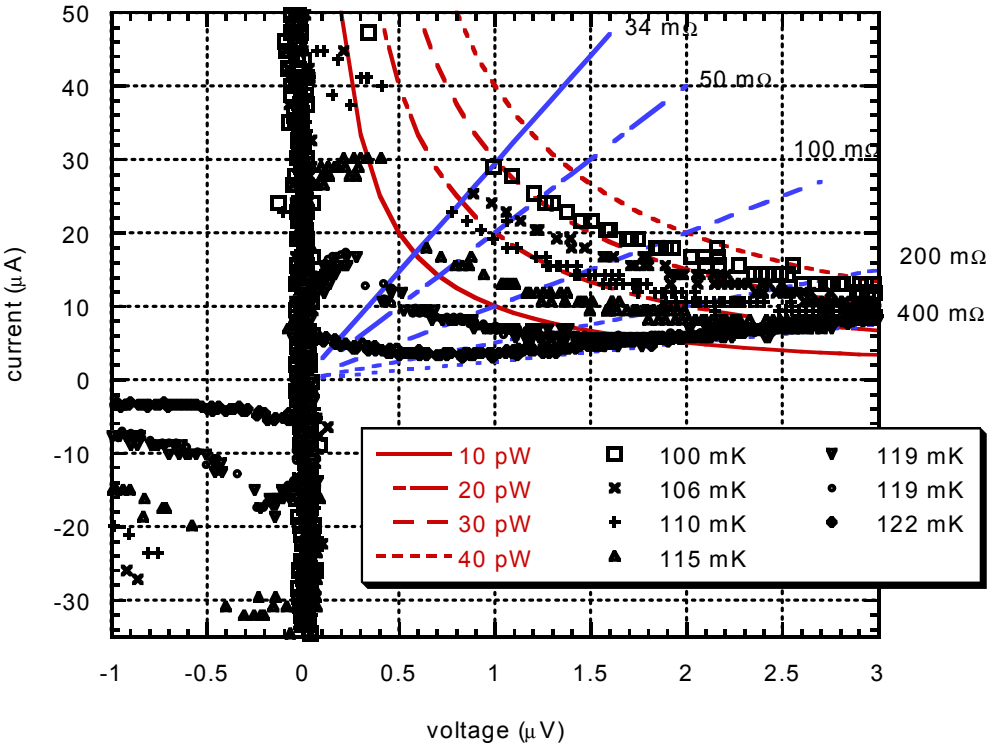

Figure 7.4. A family of I-V characteristics of the "Sunflower 12-1.2.3" microcalorimeter. In each characteristic, current I versus voltage V_0 across the TES is plotted. These characteristic curves are computed from the curves of Figure 7.3. Contours of constant resistance $R(I,T)$ of the TES and constant power are also plotted. The parasitic resistance has been subtracted from the data. The superconducting branch of each I-V curve lies on the vertical line of zero resistance. The normal branch is of 400 mΩ resistance. The curved parts correspond to the phase transition. Few data points are measured when the resistance is less than 34 mΩ, because the microcalorimeter in unstable when the TES resistance is less than R_{th}.

7.2.4 Measurement of thermal coupling

We estimate the strength of thermal coupling between the microcalorimeter and the cold bath from the data of Fig. 7.4. The cooling power is described by

$$P = K(T^N - T_{\text{bath}}{}^N). \tag{7.1}$$

When the microcalorimeter is at equilibrium, the cooling power equals the power dissipated in the microcalorimeter, $P=IV=I(V_{th}-IR_{th})$. We compute the power as a function of bath temperature T_{bath} from the data of Fig, 7.4. The resulting data is plotted in Fig. 7.5. Using the expression that $G = \partial P / \partial T \cong \partial P / \partial T_{bath}$ at $T = T_c$, we find that G=1.8 nW/K.

7.2.5 Measurement of critical current versus temperature and the phase transition

Even though the phase transition appears to occupy narrow range about 121 mK in Fig. 7.2, the TES can be in the phase transition and have a much lower temperature. This is possible because the width and temperature of the phase transition depends on the bias current.

The critical current $I_c(T)$ is the largest superconducting current sustainable by the TES at a given temperature T. When the TES is superconducting, there is no significant self heating in the microcalorimeter, therefore the microcalorimeter temperature T then equals the bath

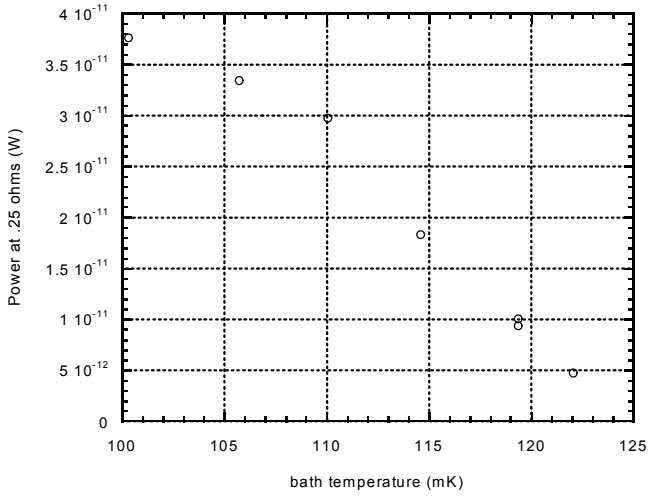

Figure 7.5 The equilibrium power of the TES versus bath temperature. The power is computed from the current-voltage characteristics of Fig. 7.4.

temperature T_{bath}. The critical current $I_c(T)$ of the TES is the largest supercurrent plotted in a current versus bias voltage curve measured at bath temperature T_{bath}. Hence, the value of the supercurrent can be obtained from data the I-V curves of Fig 7.3.

The plot of critical current versus temperature of the TES of the microcalorimeter is shown in Fig. 7.6. For each point on the I-V curves of Fig. 7.3 and Fig. 7.4, the temperature T of the microcalorimeter is calculated using the equation

$$T \cong T_{bath} + I_0 V_0 / G_0 . \tag{7.2}$$

Using the approximation (7.2), we can estimate the temperature T of the microcalorimeter for each of the data points in the I-V characteristics of Fig. 7.3. In Fig. 7.6, we plot the current I versus the temperature T of the microcalorimeter for each of the I-V characteristics of Fig. 7.3.

This plot can be used to estimate the temperature of the microcalorimeter. For example, this plot indicates that if the current I_0 through the TES is 100 μA and the TES is not superconducting, then the temperature of the TES must be least 100 mK. (If the temperature were lower, the TES would superconduct with 100 μA of current.) Based on Fig 7.6, we can also conclude that if the current through the device is less than 20 μA and the TES is not superconducting, then the temperature of the microcalorimeter must be within several millikelvin of the critical temperature T_c. From Fig. 7.2, we can conclude that the temperature of the TES can not be much larger than the critical temperature T_c and still lie in the phase transition. (Note that the critical temperature in Fig. 7.2 is several mK lower than the value $T_c \cong 125$ mK, which is inferred from the data of Fig. 7.6. This discrepancy is due to variations in thermal loading in the cryostat between the two measurements.) Based on these observations, we can conclude that if the TES is in the phase transition and the bias current is more than 1 μA and less than 20 μA then the

temperature of the microcalorimeter must be between 120 mK and 125 mK. We will use this observation to estimate the temperature of the microcalorimeter at our chosen operating point.

The boundary between the phase transition and the normal-metal state was not measured. However, a rough estimate of where this boundary lies is illustrated in Fig. 7.6. This boundary must lie to the right of points that lie in the phase transition. (These are points where $R(I,T)$ is less than 400 mΩ and greater than 0 mΩ.) The transition region in the plot includes these points. The boundary between the transition and the normal-metal state can not be at a temperature much higher than the critical temperature T_c because the transition is narrow at low current as shown in Fig. 7.2. The boundary line decreases in temperature with increasing current $|I|$ because the magnetic field associated with the current I lowers the temperature at which the transition occurs. Precise measurements of this boundary are not usually conducted by researchers because that measurement requires a second thermometer to be coupled to the microcalorimeter. (A second thermometer is useful because it directly measures temperature T but does not depend on current I.)

7.2.6 Choice of operating temperature and bias voltage

Based on the above measurements, a suitable bath temperature and bias voltage were chosen for the measurement of pulses from x-ray absorption events. The first consideration is that the microcalorimeter should be operated with the bath temperature regulated to a temperature significantly below the temperature of the TES. The bath temperature should be low so that small fluctuations in the bath temperature do not significantly affect the temperature and gain of the TES thermometer. (The effects of bath temperature fluctuations are greatly reduced when the difference between the cold bath temperature T_{bath} and the microcalorimeter equilibrium temperature T_0 is large compared to the fluctuations in the bath temperature.) Also, the calorimeter can be operated at high power when the bath

temperature is much less than the critical temperature. High power results in larger signals. Based on these considerations, the ADR temperature was regulated to a temperature of 100 mK and the TES was operated at a temperature of approximately 120 mK. The 100 mK bath temperature was also chosen because this temperature was sustainable by the ADR refrigerator for a long enough time to conduct experiments. Microkelvin fluctuations in the bath temperature associated with imperfect temperature regulation had negligible effect when the TES was operated at a temperature 20 mK above the bath temperature.

Higher energy resolution of a microcalorimeter is obtained for larger values of the parameter $\alpha' = (T_0 / R_0)\partial R / \partial T$, as described in Chapter 4. This formula indicates that the higher energy resolution is obtained at regions in the phase transition where the equilibrium resistance of the TES thermometer R_0 is small and $\partial R / \partial T$ is large. However, the TES resistance R_0 must be larger than the Thevenin resistance R_{th} to be approximately voltage biased. As stated in Section 4.6, the TES must be approximately voltage biased in order to avoid instability due to Joule heating. (In this microcalorimeter, strong Joule heating is required to elevate the temperature of the TES 20 mK above the bath temperature.)

The operating resistance R_0=100 mΩ was chosen as compromise between the demand for a large value of the parameter α', which is largest for small values of R_0, and the demand for approximate voltage bias, which occurs for values of R_0 that are significantly larger than R_{th}. With the bath temperature regulated to 100 mK, the Thevenin equivalent bias voltage was set to V_{th}=2.2 μV. This choice resulted in the desired resistance of the TES, R_0=100 mΩ. The equilibrium voltage across the thermometer was V_0=1.8 μV. This operating point lies in the negative dynamic resistance region of the current versus voltage characteristic shown in Fig 7.4. The operating point is at the intersection of the 100 mK I-V characteristic with the 100 mΩ resistance contour of Fig. 7.4. The equilibrium current through the TES was I_0=18 μA, which implies that the temperature T_0 of the microcalorimeter was roughly

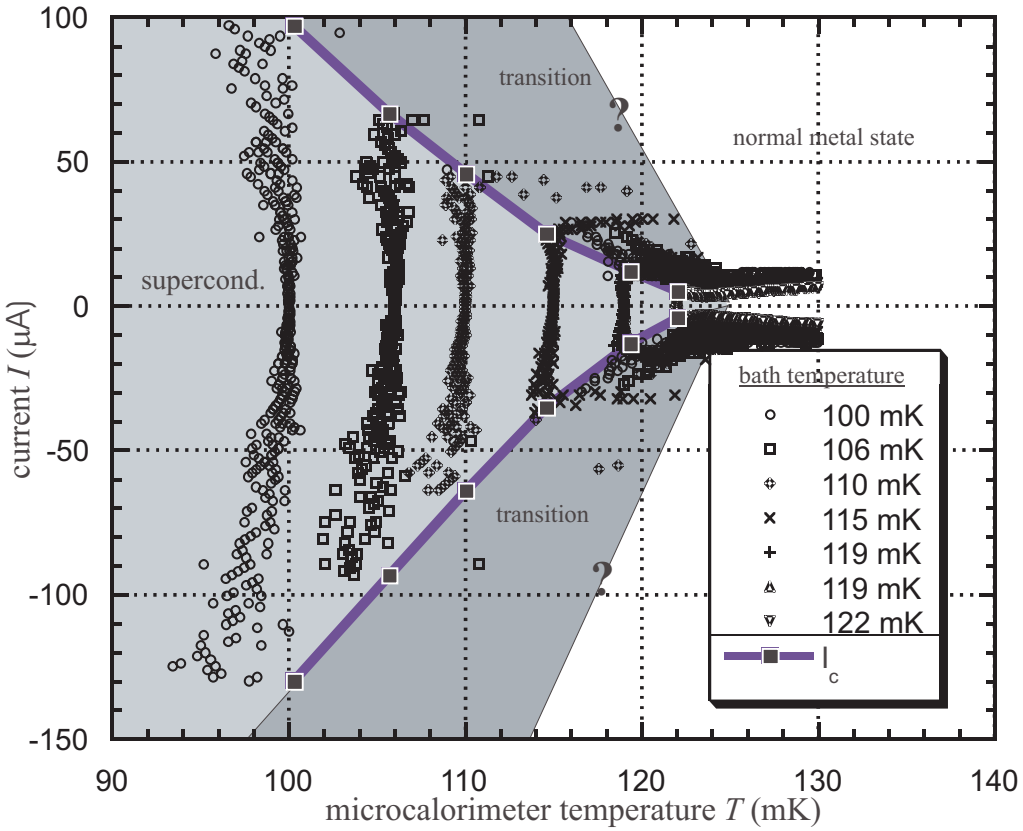

Figure 7.6. A plot of the phase transition of the "Sunflower" 12-1.2.3 microcalorimeter. The critical current versus temperature is plotted along with measurements from the I-V curves of Fig. 7.3. The microcalorimeter temperature is estimated using equation (7.2) for each of the data points of the I-V characteristics. Those points with near zero resistance lie in the superconducting region. The data points with a resistance of less than 400 mΩ but greater than 0 mW lie in the phase transition region of the plot. Data with resistance equal to 400 mΩ lie in the normal resistance region. The thermal coupling is not sufficiently determined to give the precise temperature of the microcalorimeter for data in which there is significant Joule heating. Because the temperatures of data points in the transition and in the normal stat are not precisely known, the boundary between the normal metal state and the phase transition is not precisely measured. The boundary between phase transition and the normal metal states is labeled with "?"symbols because it could not be precisely measured.

120 mK to 125 mK (based on the argument of Section 7.2.5). The temperature of the microcalorimeter was elevated 20 to 25 mK above the bath temperature by a Joule heating power of 33 pW.

An absorption event could cause the resistance of the TES to increase to as high as R=400 mΩ. This occurs when the energy of an absorption event is sufficiently large to warm the microcalorimeter to the point that the TES is completely in the normal metal phase. Such an event would reduce the current I to 5.0 μA, resulting in a current pulse with a 13 μA amplitude. This is the amplitude of the largest pulse that can be produced by the microcalorimeter at the chosen operating point. In practice, the we wish to measure x rays that produce smaller changes in temperature of the microcalorimeter because response of the microcalorimeter is only linear for small pulses.

The highest energy x ray that can be measured by the microcalorimeter is determined by heat capacity of the microcalorimeter and the width in temperature of the phase transition at the equilibrium current I_0=18 μA. As previously stated, a 6 keV energy x ray produces a temperature change of 0.44 mK in this microcalorimeter. Therefore, the phase transition has to be much wider than 0.44 mK wide for the microcalorimeter to respond linearly to the absorption of x rays of energies up to 6 keV. At low bias, the transition was only 0.25 mK wide, as shown in Fig. 7.2. At larger currents the transition is much broader in temperature, as illustrated in Fig. 7.6. At the larger operating current I_0=18 μA, the transition will be shown to be much wider.

7.2.7 Measurement of x rays

Electronic noise from pickup is reduced as much as possible before the measurement of x rays begins. All unnecessary equipment is disconnected from the cryostat, turned off, and unplugged from the power grid. The Faraday cage is often sealed shut to block radio frequency interference. The electronics are grounded as described in Section 6.7.2.

The detector is then regulated at the desired operating point: The bath temperature T_{bath} is regulated to 100 mk, and the bias voltage V_{th} is set to 2.2 μV. The microcalorimeter is exposed to the x rays from a Henke tube x-ray source as described in Section 6.6. X rays

from the x ray source then impinge on the microcalorimeter as illustrated in Fig. 7.7 The microcalorimeter responds to each x-ray absorption event by generating a pulse in the current *I*. The pulses are measured, filtered, and digitized as described in Section 6.8 and Section 6.9.

The measured pulses were filtered by the Ithaco amplifier. The box was set to low-pass filter at a frequency of 100 kHz. The low-pass filter is used to anti-alias the signal and to suppress noise at frequencies at which the signal-to-noise ratio is small.

A measured pulse from the microcalorimeter shown in Fig 7.8. The plotted pulse is the

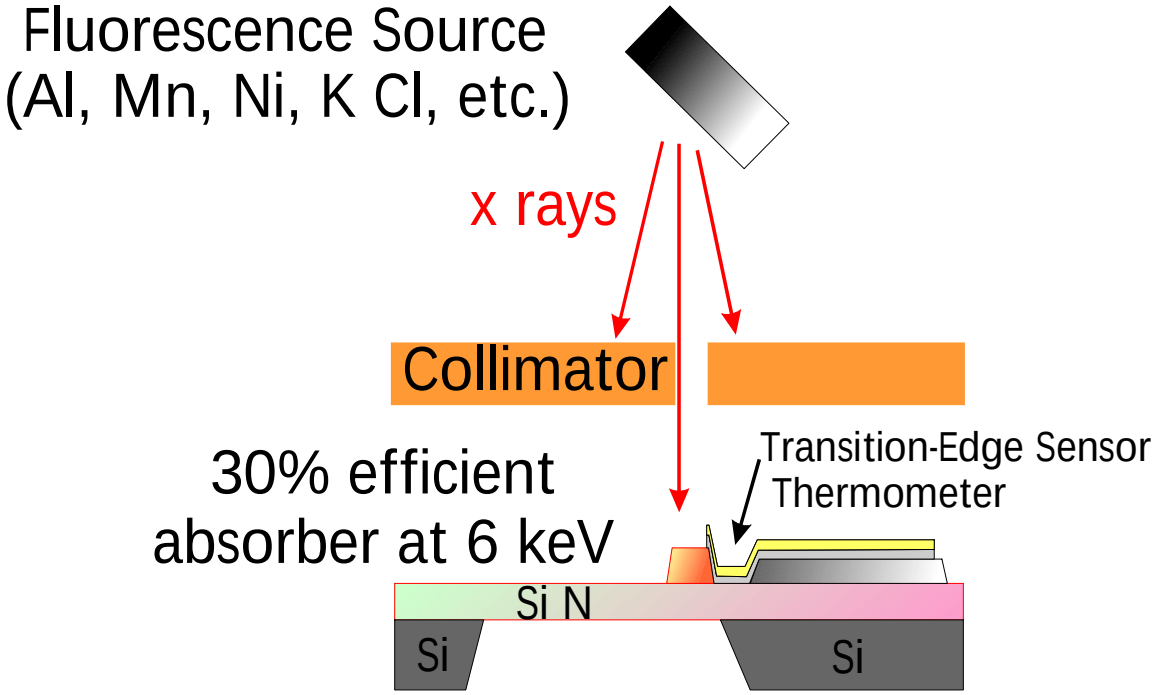

Figure 7.7. An illustration of the fluorescence measurement experiment using the Sunflower 12-1.2.3 microcalorimeter. The microcalorimeter lies under a collimator which blocks most of the x rays that would be absorbed by the substrate. The microcalorimeter is exposed to fluorescence from a number of targets located roughly a meter away. In the actual experiments, the collimator hole was not perfectly aligned and sized. This allowed some x-ray absorption events to occur in the silicon substrate.

measured response of the current I to the absorption of a 5895 eV x ray in the absorber. The pulse is exponential, with a sharp rise and a longer decay. The pulse has a decay time of 240 μs. The rise time of the pulse is 2 μs due the 100 kHz anti-alliasing filter. (The intrinsic rise time is approximately 1 μs as computed from equation (4.18)). In Fig 7.8, the noise is small compared to the signal. This noise is what limits the energy resolution of the microcalorimeter.

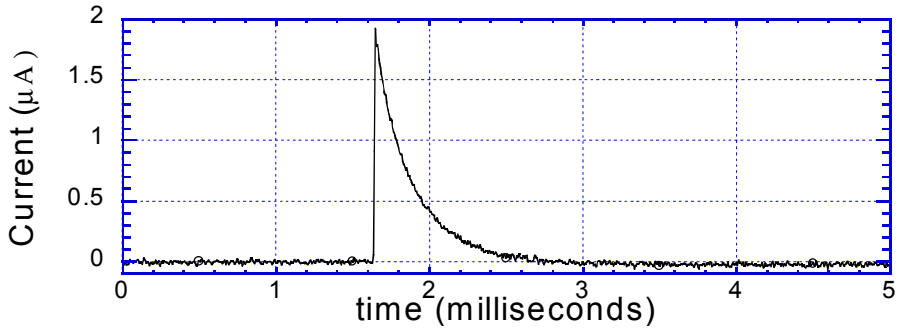

Figure 7.8. A pulse from the absorption of a 5895 eV pulse in the absorber of microcalorimeter Sunflower 12-1.2.3. The measurement contains 1024 samples of the output of the SQUID feed back voltage, V_{FB}. An anti-alias filter was used to filter out noise at frequencies greater than the sample rate so that high frequency noise would not be aliased to lower frequencies by the digital sampling. The feedback voltage is converted to units of current I conducted through the TES. The noise that appears on the exponential pulse limits the energy resolution of the microcalorimeter.

The heat capacity of the microcalorimeter is 2.2 pJ/K. This implies that the absorption of a 5895 eV x ray increases the temperature by ΔT=0.45 mK. The pulse of Fig. 7.8 corresponds to an increase TES resistance ΔR=34 mΩ. From this calculation, we can estimate α.

$$\alpha \cong \frac{T_0}{R_0}\frac{\Delta R}{\Delta T} = \frac{120\text{ mK}}{100\text{ m}\Omega}\frac{15\text{ m}\Omega}{0.45\text{ mK}} = 40 \tag{7.3}$$

The value of α' is estimated from the microcalorimeter model of Chapter 4. Based on the model, we estimate α' to be equal to 100. This value is obtained by using equation (4.17) with the values of Table 4.1 and Table 4.2. The model, with a value of α'=100 produces a pulse shown in Fig. 4.11 that approximates the measured pulse shown in Fig. 7.8. This estimate has an error which is approximately a factor of 2 due to uncertainties in various parameters in the model. The model microcalorimeter of Section 4.15 is based on the "Sunflower 12.1.2.3" microcalorimeter. (The only difference between the model and the actual calorimeter is that in the model, the inductance L is chosen to be 10 μH instead of the actual value which is 0.3 μH.)

Thousands of x rays are recorded. Each pulse is analyzed and filtered using the program "Filter Pulses" as described in Section 6.9. This program is used to generate a scatter plot of the measured pulse heights and decay times. Figure 7.9 shows a scatter plot of pulses resulting from fluorescence of Mn, Fe, Ni, K, Cl, Al and other sources. (The measured x-ray lines are labeled in Fig. 7.13.) Not all of the pulses correspond to absorption events in the absorber. Many of the pulses correspond to absorption events in the silicon substrate below or near to the TES. The substrate events have shorter decay times.

In a substrate absorption, only a fraction of the x-ray's energy reaches the microcalorimeter. Therefore, most of the pulses resulting from the substrate absorption events are only a fraction of the size of pulses from absorption events in the microcalorimeter. The fraction of the x-ray energy that is collected by the microcalorimeter depends on how close the absorption event in the substrate is to the microcalorimeter. Most of the energy is collected from nearby events. Much less is collected from events farther away.

For substrate events, much of the temperature change measured by the TES is caused by localized heating in the substrate below the TES. Heat below the TES quickly propagates away to the rest of the substrate. Consequently, the heated part of substrate cools much

quicker than the microcalorimeter does. Therefore, the pulses of substrate events have shorter decay times than the pulses of absorber events.

Events with pulses that have decay times longer than the absorber events were also observed. These events are attributed to absorption events in the aluminum wiring layer or the thermometer.

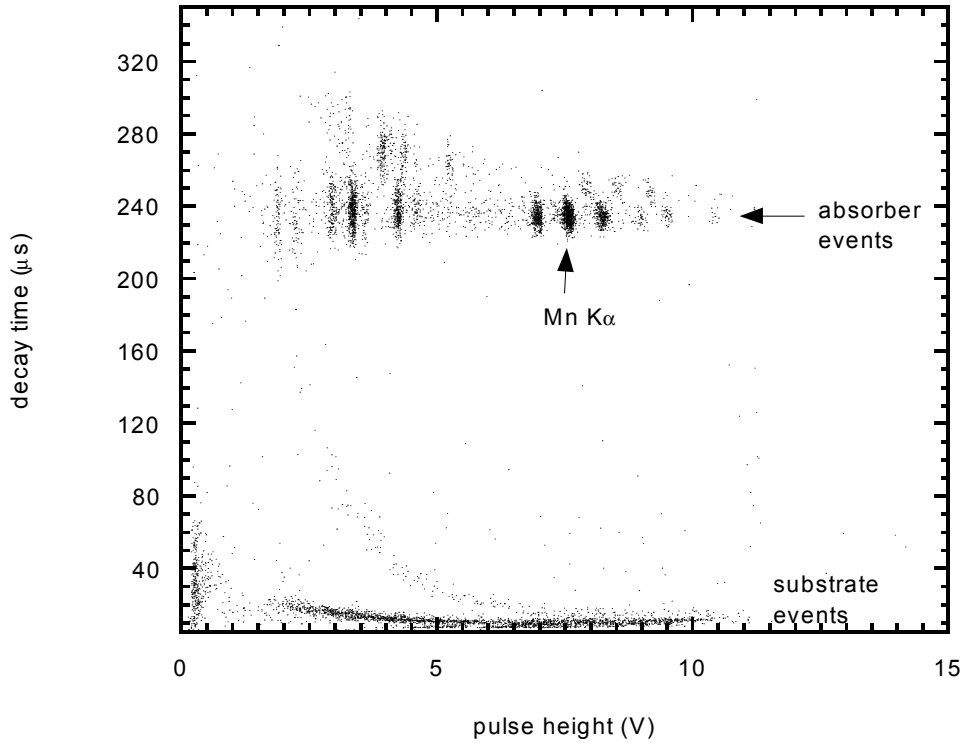

Figure 7.9 A scatter plot of pulse measurements obtained from the "Sunflower 12-1.2.3" microcalorimeter. The x rays were generated from a variety of x rays fluorescence sources including Mn, Fe, Ni, K, Cl, Al and other elements. The pulse height is the peak feedback voltage V_{FB} multiplied by a gain of 10 from the Ithaco amplifier box (as described in Chapter 6). The events with decay times of less than 80 μs correspond to x rays absorbed in the substrate. The events with 240 μs decay times are the absorber events. A correlation between the decay time and pulse height indicates position dependent response of the microcalorimeter. The substrate events show such a correlation, but the absorber events do not. There is group of events that appear to have larger amplitudes and longer decay times than the absorber events. Those events may correspond to x rays absorbed in the TES thermometer.

The highest energy resolution is obtained by using data from absorption events in the absorber only. The other events are discriminated from the absorber events by the difference in decay times and amplitudes. We use the program "filter pulses" to remove the all but the absorber events from the data.

Once the other events are removed, the absorber events are optimally filtered. (The optimal filter is described in Appendix B.) Noise samples, which are recorded immediately following the acquisition of pulse data, are used to generate the optimal filter. The optimal filter also requires a template of the typical pulse shape. Hundreds of 5895 eV pulses are averaged to form the template. After pules heights are measured using the optimal filter algorithm, a histogram of pulse heights is plotted as described in Section 1.2. The histogram plot shows the spectrum of x rays measured by the microcalorimeter.

A histogram of optimally filtered pulses of the "Sunflower 12-1.2.3" microcalorimeter is shown in Fig. 7.10. Peaks in the histogram correspond to x rays of various energies. The area under each peak is proportional to the number of x rays of the peak energy absorbed in the absorber. As indicated in the figure, the microcalorimeter demonstrated a full-width-half-maximum (FWHM) resolution of 42 eV at 6 keV.

The microcalorimeter also demonstrated excellent linearity. A plot of pulse height versus x-ray energy and the residuals are shown in Fig 7.11.

The energy resolution of the microcalorimeter is roughly constant as a function of energy. The energy resolution of various emission peaks in the spectrum is plotted in Fig. 7.12 The error bars in Fig. 7.12 represent one standard deviation errors in the measured FWHM of each of the peaks.

In calculating the errors, the peaks are modeled as Gaussian distributions with a FWHM of 42 eV. The standard deviation in the measurement of the FWHM depends on the number of x-ray measurements in the peak. The Si Kα peak of Fig. 7.12 corresponds to approximately 40 measurements. The standard deviation of the measurement of the FWHM of that peak is 4.7 eV. The Mn Kα peak corresponds to 810 measurements, with a standard deviation in the measurement of the FWHM of 1.0 eV. The standard deviations do not include other sources of error. Additional error occurs when peaks overlap, such as Fe Kα and Mn Kβ. The stray counts that form the baseline in the spectrum between the peaks also contribute some error.

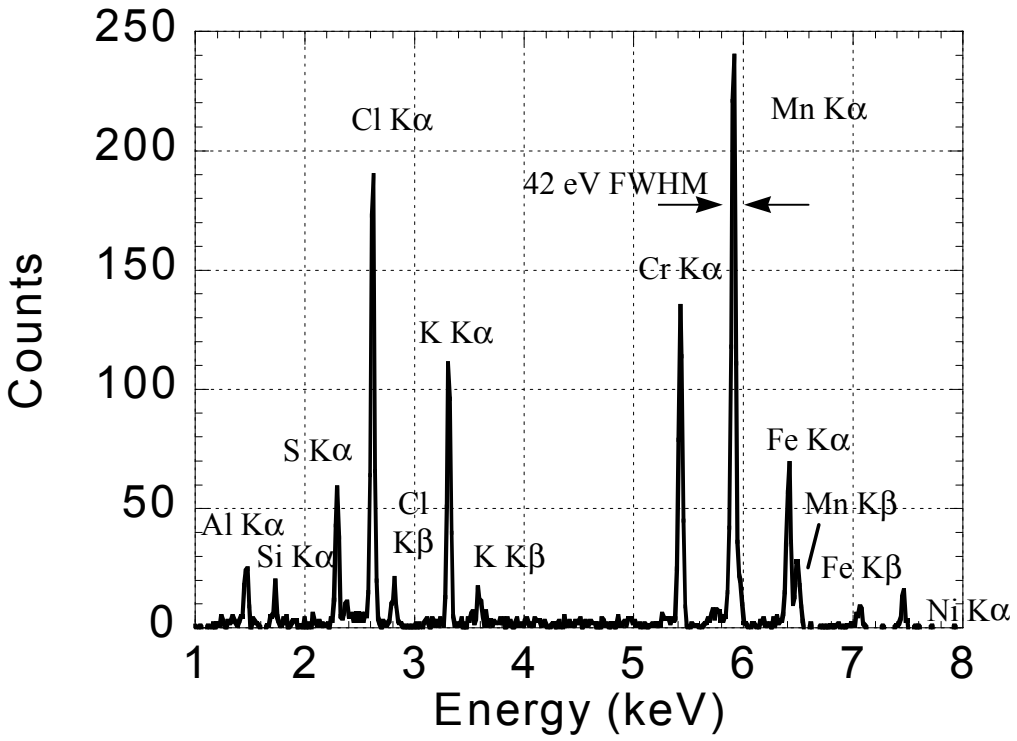

Figure 7.10 Energy spectrum obtained from the "Sunflower 12-1.2.3" microcalorimeter. The microcalorimeter measured x rays from a number of fluorescence sources, including Al, KCl, Mn, and Ni. The 5895 eV Kα emission line was measured with 42 FWHM energy resolution. This is a histogram of the absorber events of Fig. 7.9.

The spectrum in Fig. 7.10 was obtained by exposing the microcalorimeter to x-ray fluorescence from a number of different targets as described in Section 6.6. The microcalorimeter was exposed to fluorescence targets in the following order: nickel, manganese, potassium chloride on aluminum, and a target containing some sulfur as an impurity. Other x-ray lines were also observed throughout the measurement due to the fluorescence of the stainless steel vessel that housed the x-ray targets. Fluorescence from iron, chromium, and silicon in the stainless steel was observed. Fluorescence due to

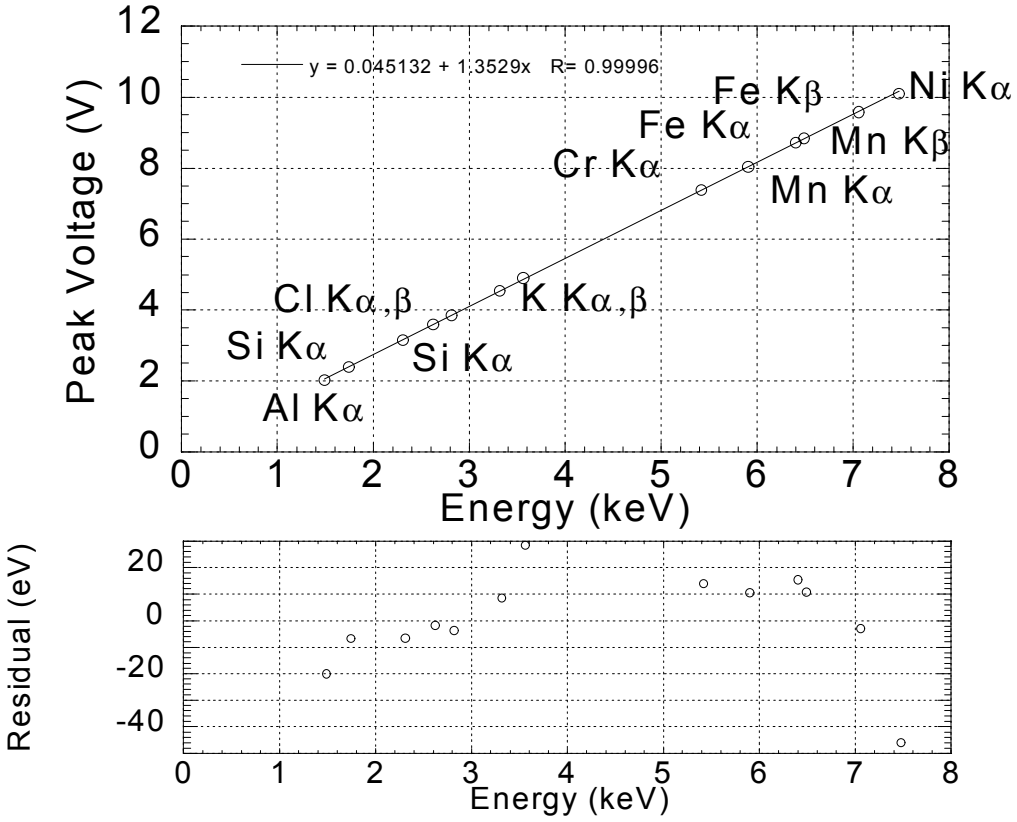

Figure 7.11 Pulse height versus x-ray energy and the residual to the linear fit. The "Sunflower 12-1.2.3" microcalorimeter demonstrated excellent linearity.

aluminum fixtures in the x-ray source was also observed.

Figure 7.13 shows a plot of pulse amplitudes (in Volts) versus pulse number. The first 400 pulses contain pulses due to the x-ray fluorescence are from the nickel target. Pulses corresponding to Ni Kα and Ni Kβ can are discernible in the plot. In pulses 400 to 1850, the Mn Kα and Mn Kβ fluorescence lines from the manganese target are discernible. In

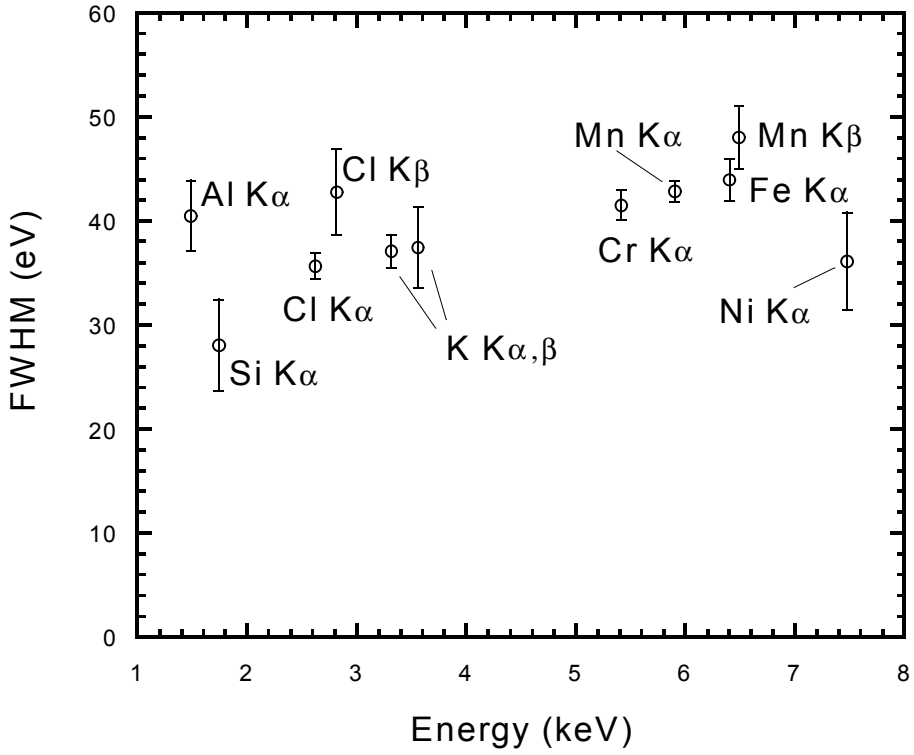

Figure 7.12 Energy resolution versus x energy of x-ray absorption events. The error bars represent one standard deviation error in the measured Full-Width-Half-Max of the peaks. The standard deviation is derived from the number of counts in the each peak. The peaks are assumed to be Gaussian distributed curves.

pulses 1850 to 3200, the K Kα, K Kβ, Cl Kα, and Cl Kβ fluorescence lines from the potassium chloride target were discernible. In pulses 3200 to 3600, the S Kα fluorescence line is discernible. The Fe Kα, Fe Kβ, Cr Kα, Cr Kβ, Si Kα, and Al Kα, fluorescence lines are discernible throughout the measurement. These lines are caused by fluorescence in the stainless steel walls of the x-ray source and in aluminum fixtures. The plot shown in Fig 7.13 is very useful because it allows the emissions of the various targets to be separated from each other. Using this plot, it is a simple matter to identify the fluorescence lines of Fig. 7.10. The energy calibration of Fig. 7.10 is obtained from the identification of these fluorescence lines. Another useful feature of the plot in Fig.7.13 is that it demonstrates that the gain of the microcalorimeter remains constant throughout the experiment. If the gain of the microcalorimeter were to change, the vertical bands in the figure would be distorted.

7.2.9 Signal and noise

After measuring the pulses, samples of the noise were recorded. A 100 kHz anti-alias filter was used to prevent noise from frequencies higher than the sample frequency affecting the measurement. Figure 7.14 contains a plot of the noise of the "Sunflower 12-1.2.3" microcalorimeter when biased on the phase transition at the chosen operating point. The figure also contains a plot of the signal due to a 5895 KeV x-ray for comparison. The calculated current noise due to Johnson noise in the TES, Johnson noise in the shunt resistor, and phonon noise is also plotted in Fig. 7.14. (The microcalorimeter model of Chapter 4 is used to compute the current noise due to these noise sources. The numerical values of the model parameters are listed in Section 4.15). The noise equivalent power (NEP) due to these noise sources is plotted in Fig. 7.15.

Figure 7.14 shows that the signal (and hence the gain) of the microcalorimeter rolls off at 660 Hz (which corresponds to the decay time of the microcalorimeter). The noise does not decrease at that frequency as would be expected if the dominate source of noise were

phonon noise. If the dominate source of noise were white voltage noise in the microcalorimeter, the noise would be reduced at low frequencies due to electrothermal feedback as described in Section 4.10 However, the noise is not decreased at low frequencies. Instead, the noise is fairly constant across the entire bandwidth of the measurement, but increases somewhat at low frequency.

The measured noise source is about 50 $pA/Hz^{1/2}$ at frequencies between 500 Hz and 20 kHz. The NEP of this noise increases with increasing frequency, as shown in Fig. 7.15. The noise cuts off at 100 kHz due to the low-pass filter. The measured noise is too large and has the wrong frequency dependence to be accounted for by phonon noise, Johnson noise, or 10 $pA/Hz^{1/2}$ amplifier noise. The dominate source of noise is probably due to voltage fluctuations in the TES thermometer because the excess noise only appears when the TES is in the phase transition and the current I through the TES is large. Because the measured noise is much larger than the theoretical noise, the microcalorimeter did not achieve the 5 eV energy resolution computed in Section 4.15.

7.2.10 Position dependence

In the x-ray fluorescence experiment, x rays were absorbed throughout the copper absorber of the Sunflower 12-1.2.3 microcalorimeter. Ideally, the response of the microcalorimeter to the absorption of an x ray of a particular energy should be the same regardless of where in the absorber the x-ray is absorbed. However, the response of some microcalorimeters does vary with position of the absorption event. This can be caused by position dependent energy losses from heat leaking out of the calorimeter. Position dependence can also be caused by time delays associated with the time its takes for the energy of the event to reach the thermometer. Position dependent response of a microcalorimeter has the effect of causing the FWHM energy resolution to be larger than would be predicted from the measured signal-to-noise ratio.

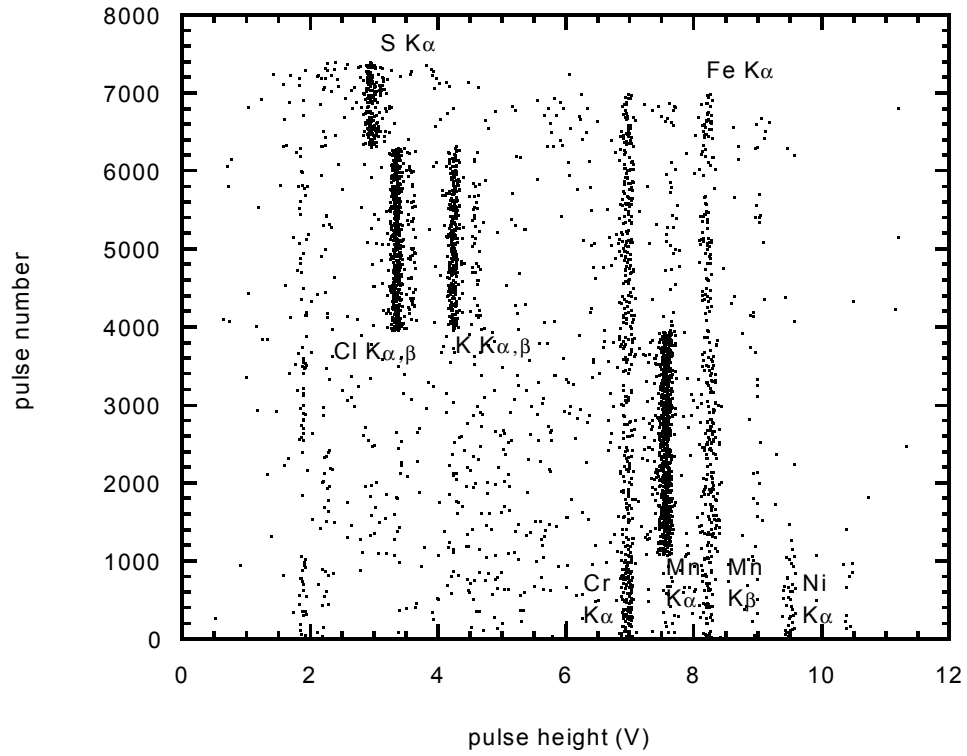

Figure 7.13. The measurement of fluorescence from nickel, manganese, potassium chloride, and sulfur targets by the Sunflower 12-1.2.3 microcalorimeter. The horizontal axis gives the heights of the measured pulses. The pulses are ordered sequentially on the vertical axis. The vertical bands correspond to measured due to fluorescence lines of various energies. Each of the target produces a unique set of bands corresponding to the target's fluorescence spectrum. A histogram all the measured pulses is shown in Fig. 7.11.

The Sunflower 12-1.2.3 microcalorimeter was designed to minimize position dependence. The compact design of the microcalorimeter allows heat in the device to diffuse through the device in about a microsecond. The heat in the microcalorimeter is evenly distributed much more quickly than it can leak out to the bath through the thermal coupling, On the time scale of the pulse measurements, heat is approximately evenly distributed in the calorimeter regardless of where the x ray is absorbed in the absorber. In addition, the majority of the keV x rays penetrate deep into the absorber before being absorbed. Hence, energy losses due to ejection of photoelectrons are rare. Therefore, the response of the microcalorimeter should be position independent.

The signal-to-noise ratio computed in Figure 7.14 corresponds to an energy resolution of 42 eV, which is the resolution that is measured. Therefore, the measurements indicate that the energy resolution is limited by the measured noise, not by position dependent effects in

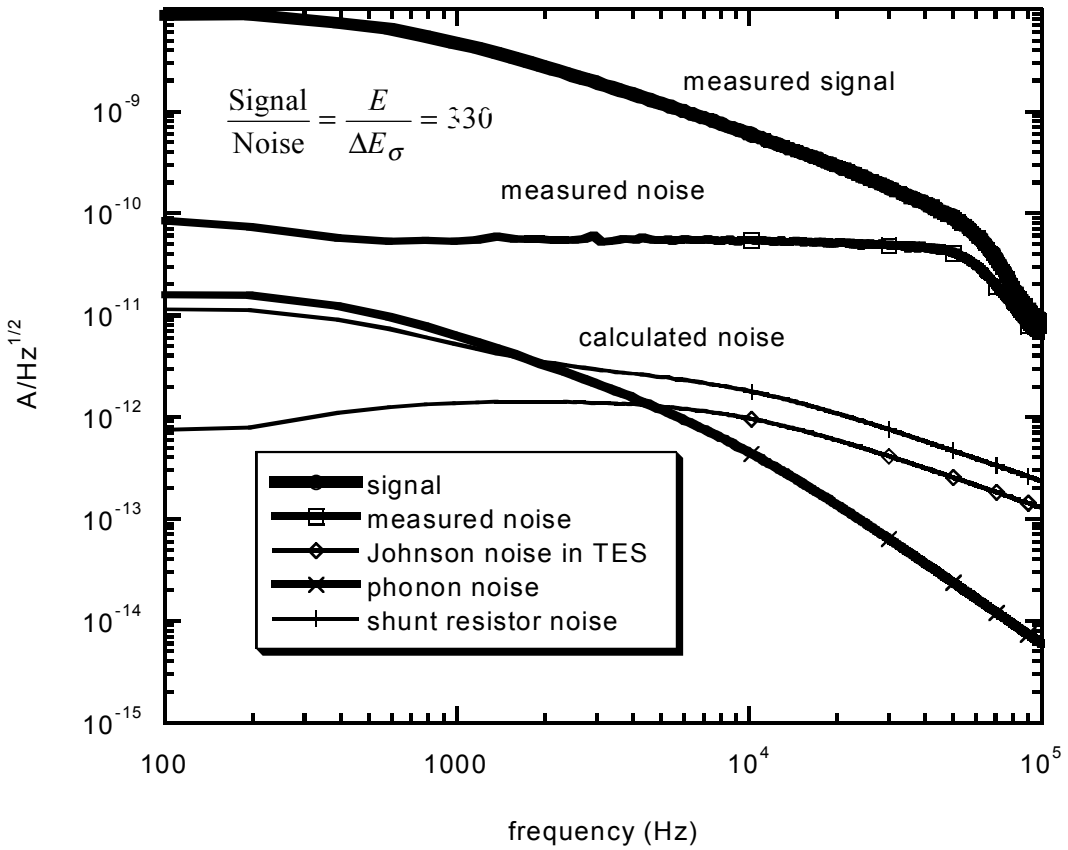

$$\Delta E_{\text{FWHM}} = 2.35\,\sigma = 2.35\,E_{\text{Mn K}\alpha}\,\frac{\text{Noise}}{\text{Signal}} = 2.35\,\frac{5895\text{ eV}}{330} = 42\text{ eV}$$

Figure 7.14 Signal and noise in the "Sunflower 12-1.2.3" microcalorimeter. The averaged signal of a 5895 eV pulses is plotted along with the measured noise. The calculated noise due to Johnson noise in the TES, phonon noise, and Johnson noise from the shunt resistor are also plotted. The measured noise is much larger than the calculated noise. The empirical data was obtained from samples of noise and pulses. In these measurements the voltage was recorded at 5 μs intervals. A 100 kHz low-pass filter was used. The total signal/noise is 330 which corresponds to the energy resolution of 42 eV. This is the actual energy resolution obtained in Fig. 7.10. Therefore, the energy resolution is not affected by position dependence in the microcalorimeter.

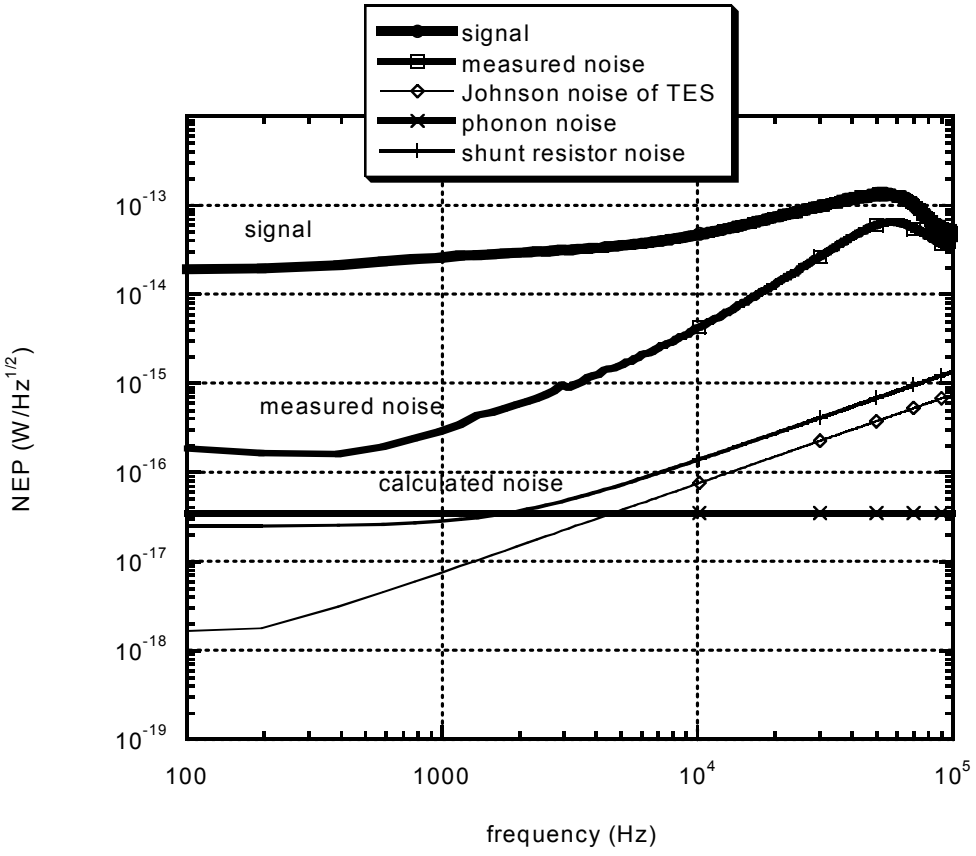

Figure 7.15. Noise equivalent power (NEP) of microcalorimeter "SF 12-1-2-3" is plotted along with the signal, and calculated NEP due to Johnson noise of the TES, Johnson noise of the shunt resistor, and phonon noise.

the microcalorimeter

Position dependence in the absorber usually affects both the pulse amplitude and the pulse decay time. The effect on the amplitude is typically correlated to the affect on the decay time. Such a correlation is apparent in the substrate events of Fig. 7.9. No such correlation is seen in the absorber events of Fig. 7.9. Therefore, the shapes of the absorber pulses do not appear to depend significantly on where in the absorber an x ray is absorbed.

7.3 Deviations from optimal behavior

Up to point, we have centered our discussion on the Sunflower 12-1.2.3 microcalorimeter. With the exception of the extra noise, that detector usually responded as would be expected by the small signal theory of Chapter 4. X-ray absorption events resulted in exponential current pulses, the amplitudes of the pulses were proportional to the energy of the measured x rays, and the energy resolution corresponds to the measured signal-to-noise ratio.

At this point, deviations from the simple behavior described above will be briefly discussed, as will lessons about how to correct such problems. One of the most common deviations from optimal behavior is an observed variation of the gain of the microcalorimeter with time. The gain in the microcalorimeter changes as the equilibrium temperature and current in the microcalorimeter varies with time. The change of equilibrium usually arises from a small drift in the temperature of the ADR stage of the cryostat. This problems is remedied by stabilization of the ADR stage of the cryostat to a temperature far below the equilibrium temperature of the microcalorimeter and by improving the temperature stability of the ADR stage, so that small variations in the temperature of the ADR stage are not significant.

Some microcalorimeters display peculiar responses to the absorption of x rays. For instance measurement of the Sunflower 6-1.2.2 microcalorimeter demonstrated two stable equilibria for a particular choice of bath temperature T_{bath} and bias voltage V_{th}. Figure 7.16 contains a plot of pulses measured by the device. In the plot, the pulses are plotted side by side in the order that they were measured. The plot shows that the microcalorimeter often switches between two stable equilibria as it responded to the absorption of an x ray. The two equilibrium have different levels of the baseline. The calorimeter switches between the two equilibria during some of the pulses.

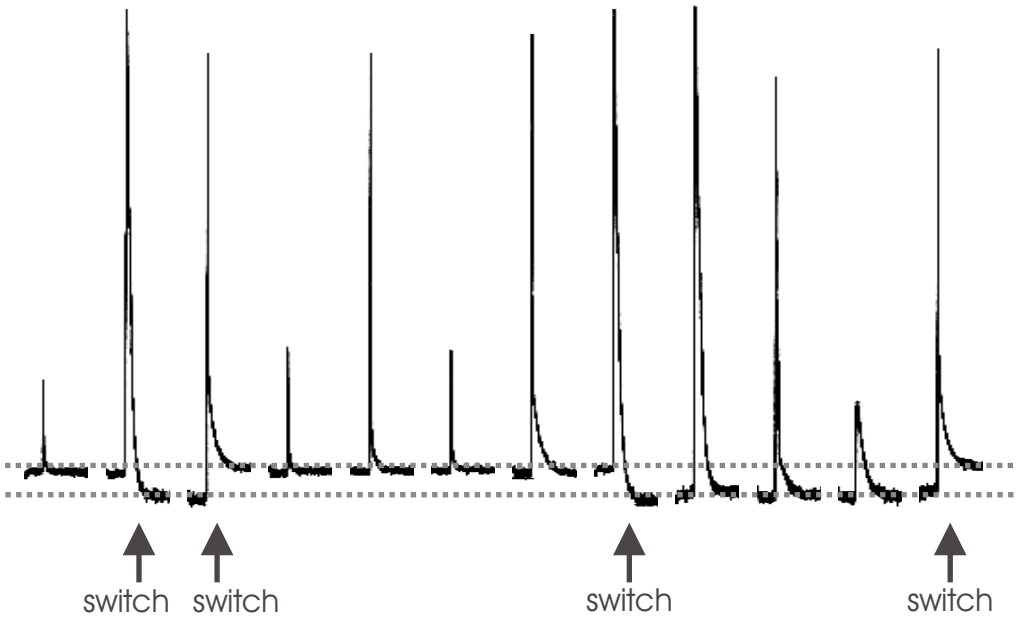

Figure 7.16. The device SF 6-1.2.2 switches between two stable equilibria during the measurement of 5895 KeV x rays.

A possible explanation for this behavior is that the thermal conductivity in the TES was too low. The normal state electrical resistance of this device is 1.7 Ω. The calculation of Section 3.3, suggests that a TES with a normal state resistance greater than 1 Ω may have poor thermal conductance. Low thermal conductance allows regions of different temperatures to form within the TES. Such independent regions could form numerous stable equilibria because they allow for many different stable configuration of temperature within the TES. If this hypothesis is correct, then such behavior can be eliminated by increasing the thermal conductance of the TES so that it remains at one temperature throughout as described in Section 3.3.

Another type of peculiar pulse was displayed by the "Sunflower" 12.1.2.3 microcalorimeter is shown in Fig. 7.17, which has a normal-state electrical resistance of 400 mΩ. One of the

plotted pulses appears to switch to a lower resistance on time scales much faster than the thermal time constant of the microcalorimeter. (In previous measurements of other TES microcalorimeters, I have often seen the current switch back and forth between two states a number of times during single pulses.) It appears that parts of the TES suddenly switch between the superconducting or normal-metal state during the pulse. This is possible if small regions of different temperatures form within the TES during the pulse. The thermal time (C/G) of these small regions can be much faster than the response of the microcalorimeter as a whole. This hypothesis predicts that such behavior should be eliminated in TES's with higher thermal conductance as described in Section 3.3.

These instabilities and the associated peculiar pulses appeared in early measurements of the Sunflower 12-1.2.3 microcalorimeter. However, reduction of pickup noise in the system through removal of ground loops appeared to eliminate the instabilities and peculiar shaped pulses. Also, the application of alternating (sinusoid) heater currents with frequencies greater than 1 kHz created instabilities and switching within the TES during heater measurements. The coupling between the heater circuit and the TES bias circuit can cause fluctuations in the bias voltage across the TES just as pickup does. Because problems with instabilities were greatest when there was large radio frequency pickup or high frequency heater currents, I suspect that high frequency noise in the TES bias voltage is a contributing factor to the observed instabilities and peculiar pulses.

7.4 Summary of results

The "Sunflower" 12.1.2.3 microcalorimeter demonstrated good energy resolution (42 eV FWHM at 6 keV) and excellent linear response to the absorption of x rays. The device also showed no evidence of position dependence, as expected. However, excess noise caused

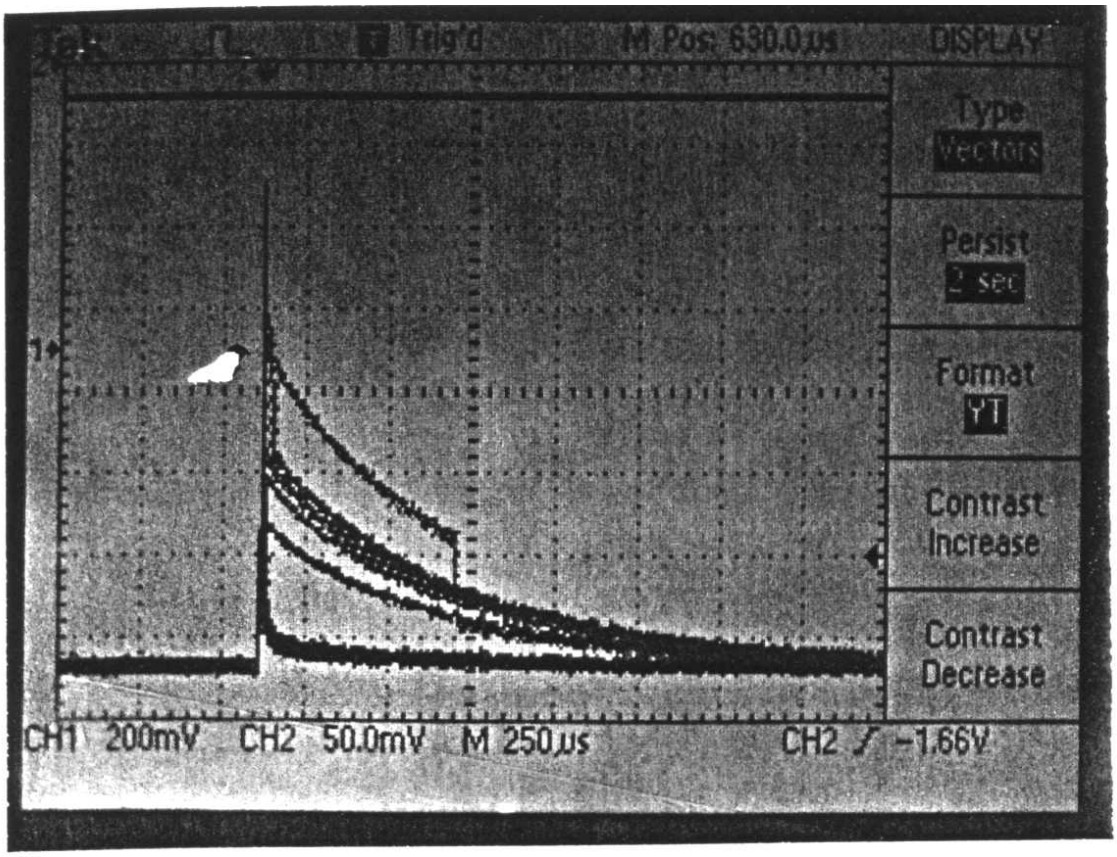

Figure 7.17 A picture of pulses taken from microcalorimeter Sunflower 12.1.2.3. At particular bias points our TES microcalorimeters have demonstrated switching during pulses. This picture shows several pulses recorded by the storage mode of our digital oscilloscope. In this picture, the horizontal direction is the time axis, with each square representing 250 μs. The decay time of these pulses is roughly 270 μs. The vertical axis is proportional to current I through the thermometer (with each square representing 0.6 μA). In the largest pulse shown, the current I exponentially decays from the maximum until about 580 μs after the trigger with a decay time of approximately 270 μs. Then, the current suddenly drops by 0.6 μA on a time scale less than 20 μs. Afterwards, the current resumes its exponential decay on a time scale of approximately 270 μs. The exponential decay time is the effective thermal time τ_{eff} of the microcalorimeter. The sudden drop occurs on a much faster time scale. This rapid change in current may be due to part of the TES suddenly switching from the resistive normal state to the superconducting state. It may be possible for parts of the TES to rapidly switch states if they are in poor thermal contact with the other parts of the microcalorimeter.

the resolution to be poorer than the optimal resolution (5 eV) of the calorimeter as computed in Section 4.15. The source of the excess noise is most likely fluctuations in the TES when it is the phase transition.

Several steps can be taken to improve the signal to noise in future TES based x-ray microcalorimeters. The signal and noise should be measured for a large number of operating points in the phase transition of a TES. Ideally, the measurements would be made for many points on the transition so that contours of signal, noise, R_0, and α', could be plotted versus current I and temperature T (in a plot resembling Fig. 7.6). From such a measurement, it could be determined where the signal-to-noise ratio highest. A better understanding of the signal and noise would enable us to design microcalorimeters in which the signal-to-noise ratio is optimized. For example, the excess noise, which dominates the noise of Fig. 7.14, only appears when the detector is biased with a large current. This noise appears to be caused by fluctuations in the TES as described in Section 7.2.9. These fluctuations are reduced to the Johnson noise limit as the electrical current density is reduced to zero. It may possible to improve the signal-to-noise ratio if the noise were reduced by redesigning the TES thermometers so that the current density in the TES is lower.

Chapter 8

SUMMARY

8.1 Summary of thesis

Many scientific and industrial applications call for quantum-efficient high-energy-resolution microcalorimeters for the measurement of x-rays. The applications driving the development of these detectors involve the measurement of faint sources of x rays in which few photons reach the detector. Microcalorimeters enable the determination of elemental composition of x-ray sources based on observed x-ray emission spectra in which only hundreds of photons are collected per emission line. These microcalorimeters must achieve very high energy resolution so that emission lines in the measured spectra are sufficiently separated from each other to make elemental identification possible. Obtaining energy resolution of several eV is a goal because many sources contain combinations of elements producing emission lines spaced only a few eV apart. Interesting astrophysical applications for these microcalorimeters include the measurement of composition and temperatures of stellar atmospheres and diffuse interstellar plasmas. Other applications of microcalorimeter technology include x-ray fluorescence (XRF) measurements of industrial or scientific samples.

We are developing microcalorimeters with transition-edge-sensor (TES) thermometers for such applications. A TES microcalorimeter consists of an absorber that is well coupled to a TES thermometer. The whole microcalorimeter is weakly coupled a to cold bath that keeps the microcalorimeter at its operating temperature. When an x-ray photon is absorbed in the

absorber, its energy is thermalized, which results in an increase in temperature of the microcalorimeter. The heat from the event then leaks out of the microcalorimeter to the cold bath, which returns the microcalorimeter to equilibrium. Thus, the response of a microcalorimeter to the absorption of a photon is a pulse in temperature. The amplitude of the temperature pulse is proportional to the energy of the absorbed photon.

A TES thermometer is used to measure the small changes in temperature caused by each absorption of an x-ray. A TES thermometer consists of a thin superconducting metal film, biased on the phase transition between the superconducting and normal-metal states. In the phase transition, the resistance increases rapidly with increasing temperature. Typically, the TES is voltage biased. The current conducted through the TES is read out by laboratory instrumentation.

The heat capacity of x-ray microcalorimeters is kept small so that the temperature of the microcalorimeter is significantly affected by the absorption of a single x-ray. Thermal noise must also be small so that the temperature pulse can be accurately measured. For these reasons, x-ray microcalorimeters are operated at low temperature (typically about 100 mK).

The microcalorimeter is fabricated on top of a silicon substrate that suspends a 0.5 μm thick membrane. The silicon substrate functions as the cold bath. Most of the microcalorimeter lies on the thin membrane, which decouples the microcalorimeter temperature from the bath temperature. The absorber of our microcalorimeter consists of 250 μm × 250μm × 3 μm of copper. The microcalorimeter obtained energy resolution of 42 eV at 6 keV. The microcalorimeter demonstrated excellent linearity, and showed no evidence that the response of the microcalorimeter varied with the location of x-ray absorption in the absorber.

The response of a TES thermometer depends both on temperature and on the electrical current conducted through it. We developed a microcalorimeter model that extends previous microcalorimeter theory to include additional current dependent effects. The model makes predictions about the effects of various forms of noise. In addition, the model helps us to understand what measurements are useful for characterizing TES microcalorimeters. Furthermore, the model can be used to aid in the design of new calorimeters. We used this model in the development and characterization of our microcalorimeters.

While the energy resolution we obtained was quite good (twice as good as conventional semiconductor-based x-ray detectors), the obtained resolution was not as good as expected, due to excess noise from fluctuations in the TES thermometer. The energy resolution of future TES microcalorimeters can be improved by redesigning the calorimeters to minimize the noise due to these fluctuations.

Appendix A

CHARACTERIZATION OF TRANSITION-EDGE SENSORS

A.1 Resistance versus temperature measurements

One of the most common measurements that is made of a TES is the measurement of its resistance R as a function of device temperature T. The resistance versus temperature curve is used as benchmark of the quality of a TES. Highly sensitive TES thermometers have transitions that are very narrow in temperature. The width of the phase transition in temperature and the parameter $\alpha = T / R(dR / dT)$ are calculated from the resistance versus temperature measurement.

The measurement of TES resistance $R(I,T)$ depends on the bias current I. Fig. A.1 illustrates the measurement of resistance versus temperature of a TES, as measured with a fixed current bias. Such measurement are made by thermally grounding a TES very well to the ADR stage of a cryostat, applying a constant current I through the TES, and measuring the voltage V across the TES. The temperature of the TES is varied by sweeping the temperature of the ADR stage of our cryostat. The temperature of the TES equals the temperature of ADR stage so long as the current is kept small to minimize Joule heating. In this measurement, the width of the transition (segment *bc* in the plot) in temperature depends on the current that is applied to the device. When the bias current is small, the width of the transition is relatively narrow. If the current nearly equals the critical current at zero temperature, $I_c(T = 0)$ of the TES, the measured transition width will be much larger.

If for the same device, the voltage is held constant and the current I is measured, a very different resistance versus temperature curve would result, as illustrated in Fig. A.2. It is different because the voltage bias traces a different trajectory in current-temperature space than the current bias does. In this measurement, the resistance is never zero because of the constant voltage. The shape of the resistance versus temperature curve depends on the voltage applied.

We often measure our transitions using the mixed bias circuit of Fig. 4.2. An illustration of a measurement of the same TES with the mixed bias circuit is illustrated in Fig A.3. This circuit applies a current bias when the resistance $R(I,T)$ of the TES is much less than the shunt resistance R_s, and it applies a voltage bias when the resistance of the TES is much larger than the resistance of the shunt R_s. The resulting case is a mixture of the two previous cases. If the superconducting segment (ab) is measured with the same current I in

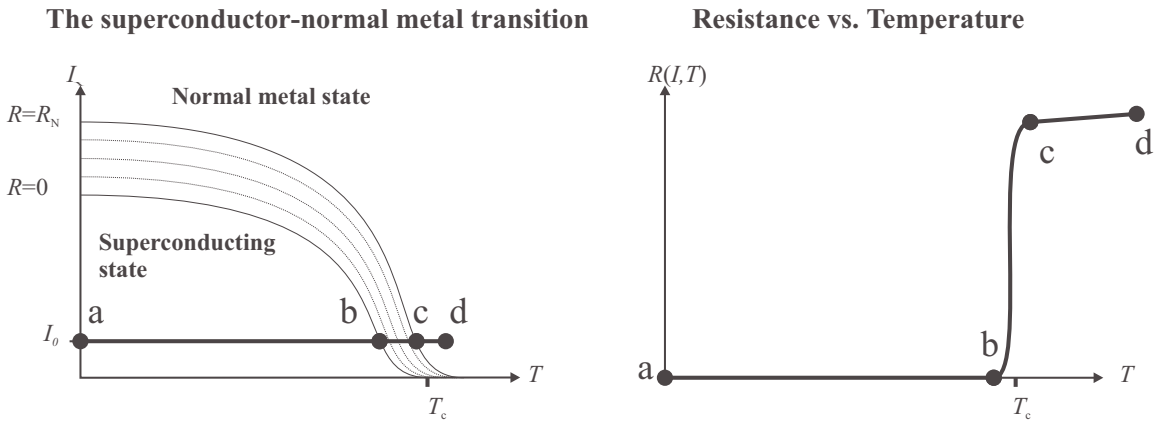

Figure A.1. An illustration of a measurement of resistance versus temperature with the constant bias current *I*. The superconductor to normal-state phase transition is shown in both plots. The left plot shows contours of resistance as a function of TES temperature *T* and electrical current *I* conducted through the TES. A constant current trajectory is also illustrated in the left plot. The right plot shows the plot of resistance *R* versus temperature *T* of the TES as would be measured along the trajectory in the left plot. On this trajectory, the current *I* is fixed, TES temperature *T* is varied, and resistance is measured. The TES superconducts in segment *ab*. The TES has the normal resistance R_N in segment *cd*. The TES is on the phase transition in segment *bc*.

the mixed bias case (Fig. A.3) as it is in the current bias case (Fig. A.1), then the measured width in temperature will be wider in the mixed bias case.

A.2 Current-voltage characteristics

Measurement of current through a TES versus voltage difference across the TES provides useful information about TES microcalorimeters. A current versus voltage characteristic (also called an I-V curve) can be measured by periodically sweeping the voltage across the TES, while measuring the current, and holding the bath temperature constant. (The bath temperature is the temperature of the ADR stage.).

An example of an I-V curve is shown in Fig A.4. Different branches of the I-V curve correspond to different phases of the TES. The superconducting branch is the vertical linear section in the center of the plot. The normal metal phase corresponds to the diagonal linear sections on the left and right sides. The curved section of the I-V curve, lies on the

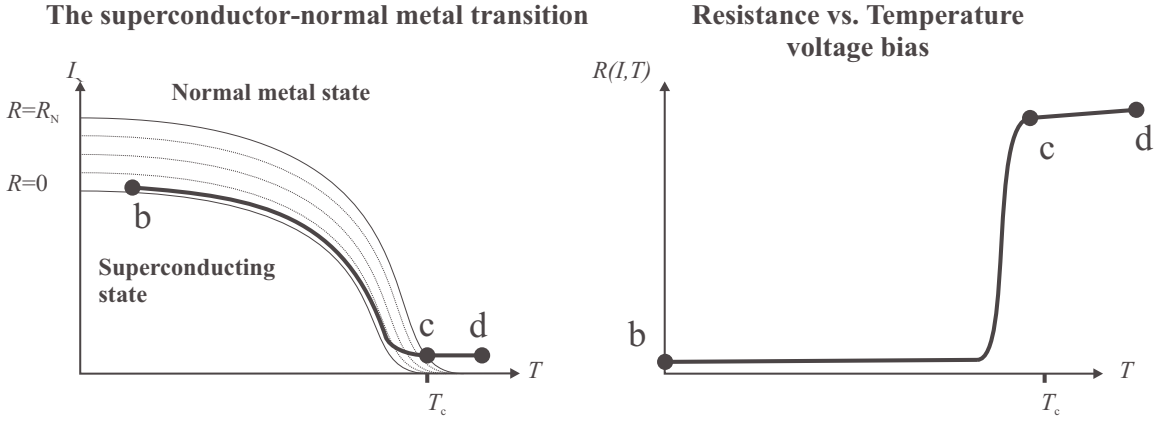

Figure A.2. An illustration of the measurement of resistance versus temperature with constant voltage bias. The right plot shows the plot of resistance R versus temperature T of the TES. The left plot shows the corresponding trajectory in current I versus temperature T. The curves on the I-T plot indicate the phase transition and represent contours of resistance R. In this measurement, the voltage across the TES is fixed, TES temperature T is varied, and resistance is measured. The TES has the normal resistance R_N in segment *cd*. The TES is on the phase transition in segment *bc*.

superconducting to normal metal phase transition. When a TES is operated at high power and a voltage bias is applied, the part of the I-V curve on the phase transition is hyperbolic in shape if the phase transition is sufficiently narrow in temperature. This occurs because electrothermal feedback keeps dissipated power IV approximately constant, so that the temperature of the TES remains in the phase transition near the critical temperature T_c.

We often use measured IV curves in order to pick bias voltages and bath temperatures at which to operate our TES microcalorimeters. If a TES x-ray microcalorimeter is exposed to x-rays during a measurement of an I-V curve, x-rays cause spikes to appear on the I-V curve where the detector gain is large. This method is often used to pick a bias voltage such that the gain is large.

Recording a series of I-V curves at different bath temperatures, provides even more information. Such a family of I-V curves can be used to map the phase transition and help

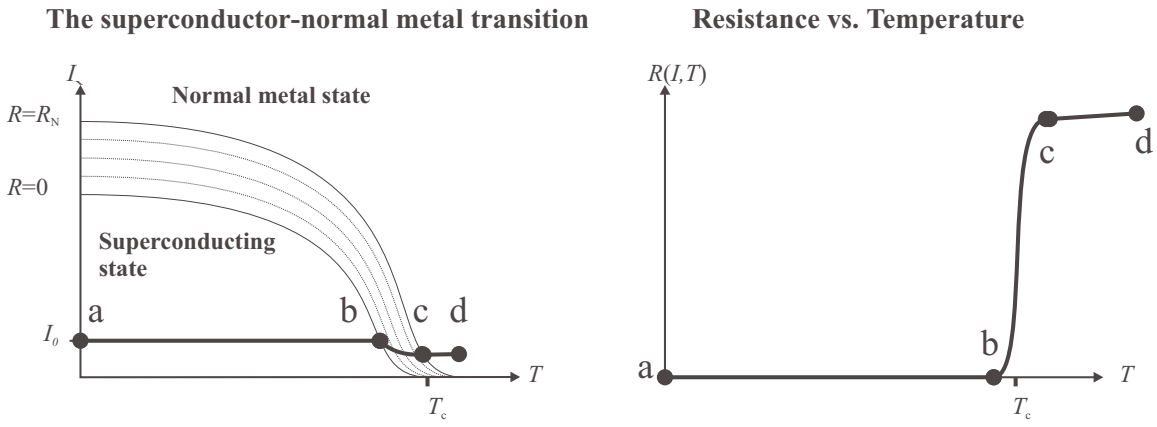

Figure A.3. An illustration of the measurement of the resistance versus temperature of a TES, using the bias circuit of Fig. 4.2. This is the kind of measurement of resistance versus temperature that is typically recorded by us. The right plot shows the plot of resistance R versus temperature T of the TES. The left plot shows the corresponding plot in current I versus temperature T. The curves on the I-T plot indicate the phase transition and represent contours of resistance R. In this measurement, the bias voltage V_b is constant, TES temperature T is varied, and resistance is measured. The TES superconducts in segment ab. The TES has the normal resistance R_N in segment cd. The TES is on the phase transition in segment bc

pick a voltage bias and bath temperature such that the detector gain is maximized and the noise is minimized.

The shape of a measured IV curve depends on the shape of the superconductor to normal metal phase transition, on the bath temperature of the device, on the amount of self heating in the microcalorimeter, and on whether the TES is current or voltage biased.

Fig. A.4 illustrates the I-V curve of a TES that is voltage biased with negligible self heating of the microcalorimeter. (Self-heating occurs when Joule heating in the thermometer raises the temperature of the calorimeter above the bath temperature T_{bath}). The bath temperature T_{bath} is regulated to a fixed temperature below the critical temperature T_c of the TES.

When the Joule heating power in a TES is large enough to elevate the temperature of the electrons above the bath temperature, the slope dI/dV of the I-V in the phase transition will be decreased due to electrothermal feedback. When the self heating is strong enough to raise the temperature of the electrons in the TES far above the bath temperature, the slope of the I-V in the phase transition is negative (as is the dynamic resistance dV/dI). An I-V characteristic with negative dynamic resistance is illustrated in Fig. A.5.

Electrothermal feedback in a TES microcalorimeter, which is responsible for the negative dynamic resistance, is negative when the TES is voltage biased. If the TES is current biased, there is positive electrothermal feedback that causes the microcalorimeter to be unstable, causing discontinuities in the part of the I-V curve as illustrated in Fig. A.6

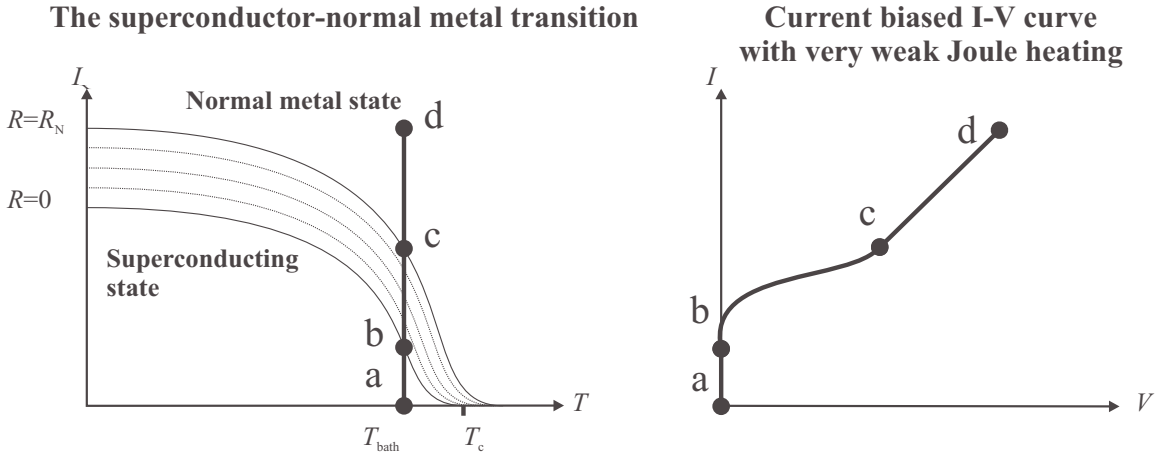

Figure A.4. An illustration of a I-V curve measured with a voltage bias on the TES and negligible self heating in the microcalorimeter. The right plot shows the plot of current I versus voltage V across the TES. The left plot shows the corresponding plot in current I versus temperature T. The curves on the I-T plot indicate the phase transition and represent contours of resistance R. In this measurement, the temperature T is constant, voltage V is varied, and resistance is measured. The TES superconducts in segment *ab*. The TES has the normal resistance R_N in segment *cd*. The TES is on the phase transition in segment *bc*.

In our measurements, we typically use the "mixed" bias circuit of Fig. 4.2. As previously stated, this circuit provides a current bias when the resistance $R(I,T)$ of the TES is small compared to the shunt resistance R_S. When the resistance of the TES is larger than the shunt resistance, the TES is voltage biased. In this case, the only unstable part of the I-V curve is the part where dynamic resistance is negative and the resistance of the TES $R(I,T)$ is leas than the Thevenin resistance R_{th}. This case is illustrated in Fig. A.7.

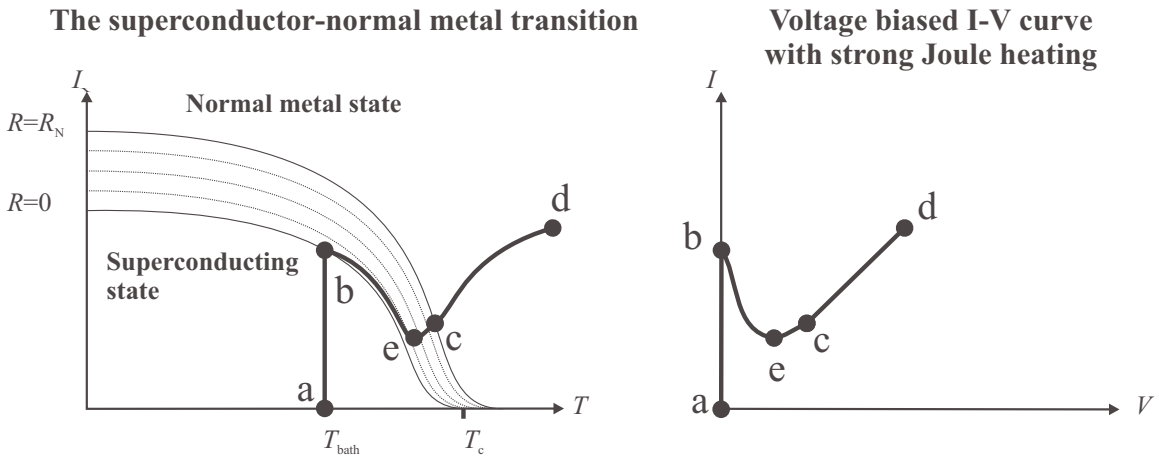

Figure A.5 An illustration of the measurement of an I-V curve. In this case, the TES is voltage biases and there strong self heating. This is the classic shape of an I-V curve of a TES operated at high power (compare to Fig 7.4). Electrothermal feedback in the phase transition causes part of the I-V curve to have negative dynamic resistance. The negative dynamic resistance region corresponds to biases where the calorimeter has the largest gain. When the thermometer is superconducting, the microcalorimeter temperature T equals the bath temperature T_{bath}. At biases where the TES is resistive, the self heating elevates the temperature of the microcalorimeter above the bath temperature. The right plot shows the plot of current I versus voltage V across the TES. The left plot shows the corresponding trajectory in current I versus temperature T. The curves on the I-T plot indicate the phase transition and represent contours of resistance R. In this measurement, the bath temperature T_{bath} is constant, voltage V is varied, and current I is measured. The TES superconducts in segment *ab*. The TES has the normal resistance R_N in segment *cd*. The TES is on the phase transition in segment *bc*.

A.3 The family of current-voltage characteristics

We often measure a sequence of I-V curves of a TES microcalorimeter using the mixed bias circuit of Fig. 4.2. Each IV curve in the sequence is measured with the bath temperature T_{bath} (which is the temperature of the ADR stage) set to a different value. Typically, the bath temperature is set to temperatures ranging from far below the critical temperature T_c of the TES to a temperature greater than T_c such that the TES is a normal metal.

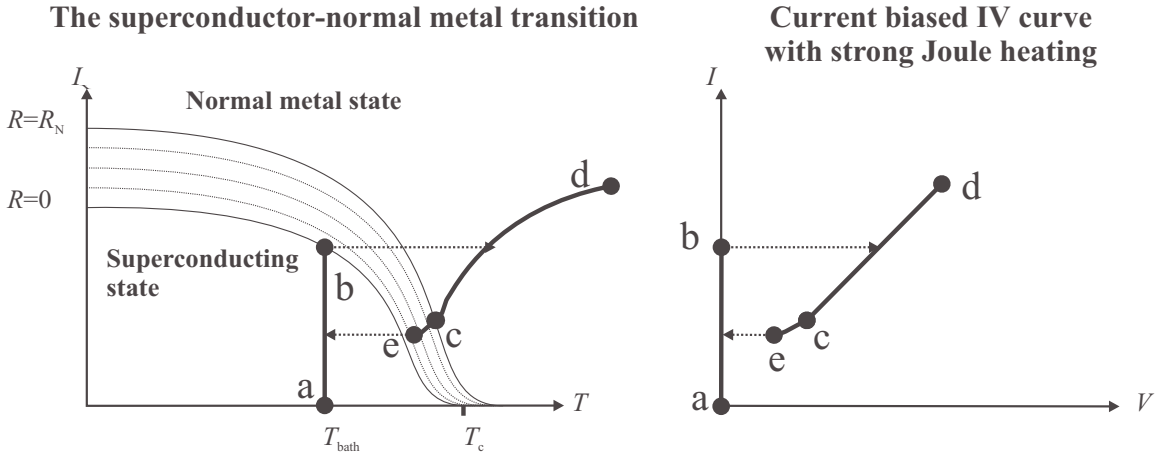

Figure A.6. The measurement of the same TES as in Fig A.6, but with a current bias instead of a voltage bias. With a current bias, there is a discontinuity in the I-V curve. Only regions with positive dynamic resistance can be measured. When the thermometer is superconducting, the microcalorimeter temperature T equals the bath temperature T_{bath}. At biases where the TES is resistive, the self heating elevates the temperature of the microcalorimeter above the bath temperature. The right plot shows the current I versus voltage V across the TES. The left plot shows the corresponding plot in current I versus temperature T. The curves on the I-T plot indicate the phase transition and represent contours of resistance R. In this measurement, the bath temperature T_{bath} is constant, current I is varied, and voltage V is measured. The TES superconducts in segment *ab*. The TES has the normal resistance R_N in segment *cd*. The segment *bc* is not measured because there is no stable equilibrium at bias voltages between point *b* and point *c*.

A sequence of several such I-V curves is illustrated in Fig. A.8. Typically, those IV curves in which the bath temperature T_{bath} is just below the critical temperature T_c have positive dynamic resistance; they have little self heating when the TES in the phase transition because the current I through the TES is quite small. When the bath temperature is set to be far below the critical temperature, the current in the TES can be large on the transition. Hence, those I-V curves correspond to low bath temperatures tend to have larger self heating, and negative dynamic resistance regions. IV curves measured with the bath temperature set above the critical temperature are strait lines corresponding the normal metal resistance of the TES.

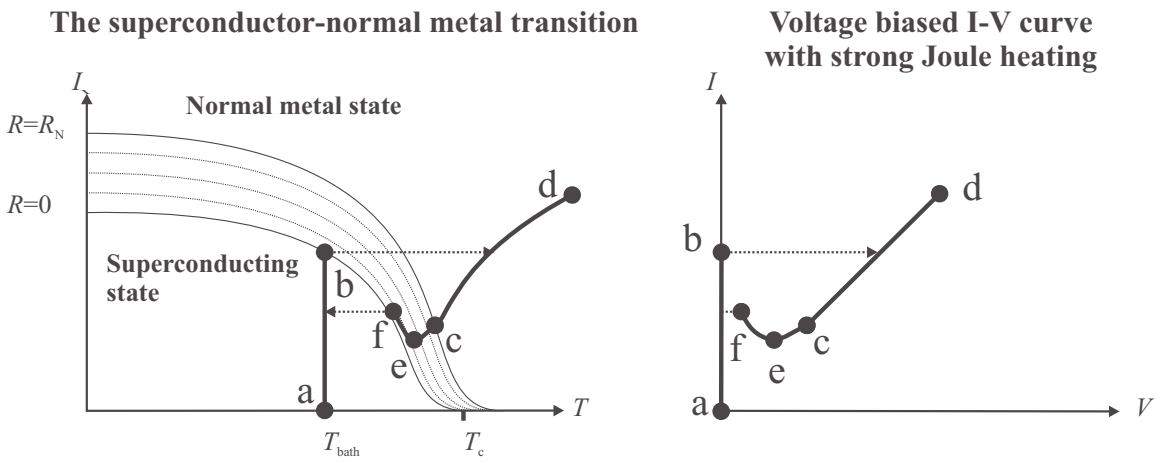

Figure A.7 An illustration of the measurement of an I-V curve with the bias circuit of Fig 4.2. The Thevenin resistance R_{th} is much less than the normal resistance $R_{N.}$ When the resistance R of the TES is less then the resistance R_{th}, the TES is approximately current biased. When the resistance R of the TES is more then the resistance R_{th}, the TES is approximately voltage biased. When the thermometer is superconducting, the microcalorimeter temperature T equals the bath temperature T_{bath}. At biases where the TES is resistive, the self heating elevates the temperature of the microcalorimeter above the bath temperature. The right plot shows the current I versus voltage V across the TES. The left plot shows the corresponding trajectory in current I versus temperature T. The curves on the I-T plot indicate the phase transition and represent contours of resistance R. In this measurement, the bath temperature T_{bath} is constant, bias voltage V_b is varied, and voltage I is measured. The TES superconducts in segment *ab*. The TES has the normal resistance R_N in segment *cd*. In segment *de*, the TES has negative dynamic resistance and is approximately voltage biased. The segment *be* is not measured because there is no stable equilibrium at bias voltages between point *b* and point *e* (where $R<R_{th}$).

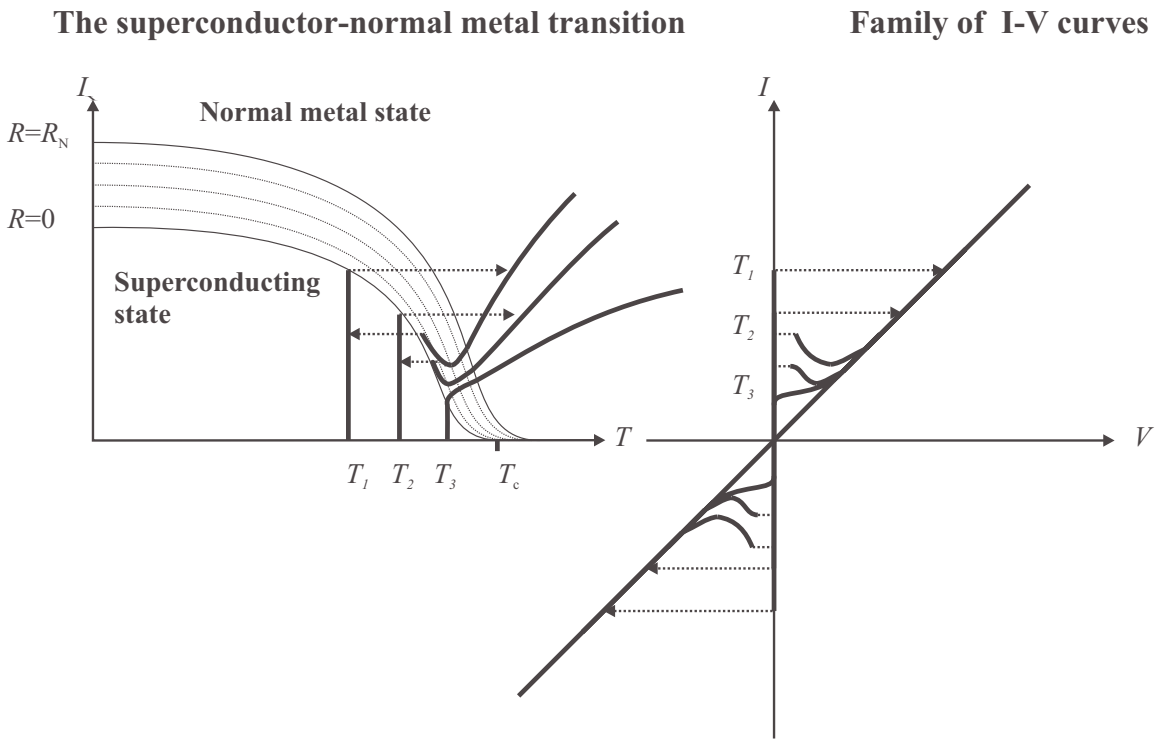

Figure A.8. An illustration of the measurement of a family of I-V characteristics. The I-V characteristics are illustrated in the plot on the right. The plot on the left shows the corresponding trajectories in current I and temperature T. Contours of resistance of the TES are also plotted in the left diagram. Each characteristic corresponds to a particular bath temperature.

Appendix B

THE OPTIMAL FILTER

B.1 The optimal filter algorithm

An absorption of an x-ray in a microcalorimeter produces a pulse in the temperature *T* of the microcalorimeter as described in Section 1.1. A resistive thermometer, such a TES, converts temperature variations in the TES to an electronic signal.

The measurements of pulses from a microcalorimeter contain both signal and noise. Ideally, the electronic signal is a pulse that whose amplitude is proportional to the energy of the absorbed x ray. The noise is caused by thermodynamic fluctuations in the microcalorimeter, fluctuations in laboratory electronics, and other sources such as radio frequency pickup. The noise limits the energy resolution obtainable from the measurements. The effects of noise on the measurements is minimized by filtering out frequencies from the measurements which have a poor signal-to-noise ratio.

The optimal filter [1] is designed to measure the amplitude of a signal in the presence of random noise. This filter is only truly optimal if the noise is only a function of frequency (and not time dependent), and the noise must be uncorrelated between frequencies.

The derivation of the optimal filter is as follows. The *j*th x ray is absorbed a microcalorimeter at time $t = t_j$. The energy of the absorbed x ray is E_j The absorption

event generates a signal $S_j(t)$. All of the signals are assumed to be pulses of the same shape. Therefore, signal $S_j(t)$ can be expressed as

$$S_j(t) = A_j s(t - t_j) \tag{B.1}$$

where $s(t)$ is a function that describes the shape of a typical pulse and A_j is the amplitude of the *j*th pulse. The amplitude A_j is proportional to the energy E_j.

The measurement of a single pulse consists of a sequence of *x* samples periodically recorded at time intervals Δt. A measurement $M_j(t)$ of the *j*th signal also contains noise $N_j(t)$.

$$M_j(t) = S_j(t) + N_j(t) \tag{B.2}$$

Note that the terms of equation (B.2) are defined at the discrete time intervals

$$t \in \{t_j, t_j + \Delta t, \ldots \ldots, t_j + (x\text{-}1)\,\Delta t\}\ . \tag{B.3}$$

We obtain an estimate of the energy E_j of an x ray absorption from the measurement $M_j(t)$. The discrete Fourier transform of the measurement is

$$M_j(f) = A_j s(f) e^{-i2\pi f t_j} + N_j(f)\,, \tag{B.4}$$

where $s(f)$ and $N_j(f)$ are Fourier transforms of the shape function $s(t)$ and the noise $N_j(t)$.

The measurement $M_j(f)$ is defined only for discrete frequencies $f = \{0, \Delta f, 2\Delta f, \ldots, f_{\max}\}$, where $\Delta f = 2 / x\Delta T$ and $f_{\max} = x\Delta f / 2$ is the Nyquist frequency.

The noise $N_j(\omega)$ is assumed to be Gaussian distributed and uncorrelated between frequencies. The magnitude of the of noise $N_j(\omega)$ depends on the bandwidth *b* over which the noise is measured, which is the bandwidth of the analog filters used in conjunction with the digitizer. The noise increases with the square root bandwidth because noise at differing frequencies is not correlated. The best signal to noise is obtained when a low-pass filter is used to filter noise at frequencies greater than the Nyquist frequency so that $b = f_{\max}$.

We fit the function $A_j s(f)$ to the Fourier transform of the *j*th measurement $M_j(f)$ using the linear least squares method. The likelihood *L* of an estimate of A_j and t_j being correct is given by the likelihood function:

$$L \propto \exp\left[-\sum_f \frac{\left| M_j(f) - A_j s(f) e^{-i2\pi f t_j} \right|^2}{2\left(\sigma(f)\right)^2} \right]. \tag{B.5}$$

In the equation (B.5), $\sigma(f)$ is the standard deviation of the noise at frequency *f*:

$$\sigma(f) = \sqrt{\left\langle \left| N_j(f) \right|^2 \right\rangle - \left| \left\langle N_j(f) \right\rangle \right|^2}. \tag{B.6}$$

The most likely value of A_j occurs when $\partial L / \partial A_j = 0$. The most likely value is

$$A_j = \frac{1}{n}\sum_f M(f)q^*(f)e^{i2\pi f t_j}\Delta f \,, \tag{B.7}$$

where the normalization function n is

$$n = \sum_f \left|\frac{s(f)}{\sigma(f)}\right|^2 \Delta f \,, \tag{B.8}$$

and the function $q(f)$ is

$$q(f) = \frac{s(f)}{\left(\sigma(f)\right)^2} \,. \tag{B.9}$$

Equation (B.7) is rewritten as a convolution in the time domain:

$$A_j(t_j) = \frac{\sum_t M(t)q(t-t_j)}{\sum_t s(t)q(t-t_j)} \,, \tag{B.10}$$

where $q(t)$ is inverse the Fourier transform of $q(f)$. The function $q(t)$ is known as the optimal filter. The most likely value of t_j occurs when $A_j(t_j)$ is maximized with respect to t_j.

The standard deviation of the likelihood function L is

$$\sigma_{\mathrm{A}} = \left[\sum_{f=0}^{f_{\max}} \left|\frac{s(f)}{\sigma(f)}\right|^2\right]^{-1/2} \tag{B.11}$$

The energy of an event E_j is proportional to the amplitude A_j, where the constant of proportionality is dE/dA. Therefore, the standard deviation in terms of the energy measurements E_j is

$$\sigma_E = \frac{dE}{dA}\left[\sum_{f=0}^{f_{\max}} \left|\frac{s(f)}{\sigma(f)}\right|^2\right]^{-1/2} = \left[\sum_{f=0}^{f_{\max}} \frac{4\Delta f}{\left|\mathrm{NEP}(f)\right|^2}\right]^{-1/2}, \tag{B.12}$$

where the noise equivalent power (NEP) is

$$\mathrm{NEP}(f) = 2\frac{dE}{dA}\frac{\sigma(f)}{|s(f)|}\sqrt{\Delta f}\,. \tag{B.13}$$

The interval Δf can not be made arbitrarily small because it is limited by the frequency resolution of laboratory equipment. Nevertheless, it is assumed that Δf is sufficiently small that equation (B.11) can be expressed as an integral.

$$\Delta E_{\mathrm{FWHM}} = 2.35\sigma_{\mathrm{E}} = 2.35\left(\int_0^{\infty} \frac{4\,df}{\left|\mathrm{NEP}(f)\right|^2}\right)^{-1/2}. \tag{B.14}$$

Equation (B.14) is used in calculating the energy resolution of a microcalorimeter given the NEP due to all the sources of noise. In Chapter 4, we use this equation to determine how various forms of noise affect the energy resolution of a microcalorimeter.

The optimal filer algorithm is incorporated into our data analysis software as described in Chapter 6. The software performs the optimal filtering by convolving each of the measurements $M_j(t)$ with a computed optimal filter $q(t)$. The maximum of the

convolution is the amplitude of the pulse A_j. The maximum occurs at the time t_j of the jth event. A histogram is computed from the values of A_j. When the histogram is calibrated into units of energy, the result is a spectrum similar to Fig. 1.4. The width ΔE_{FWHM} of the peaks in the spectrum is given by equation (B.14).

[1] A. E. Szymkowiak, R. L. Kelley, S. H. Moseley *et al*., "Signal processing for microcalorimeters," Journal of Low Temperature Physics **93** (3-4), 281-5 (1993).

University of California
Lawrence Livermore National Laboratory
Technical Information Department
Livermore, CA 94551